



CO₂ReMoVe - Progress Report



Facultad de Ciencias Astronómicas y Geofísicas
Universidad Nacional de La Plata (UNLP)
Argentina

WP 3.7 TTC research on passive and active seismic methods

Date: February 2010

Starting Date: September 2007

Participants:

Dr. Juan Enrique Santos, (Principal Investigator)

Dra. Claudia L. Ravazzoli

Dra. Patricia M. Gauzellino

Dr. Fabio Zyserman

Dr. J. Germán Rubino

Geof. Julián L. Gómez (Phd student)

Index

Summary	1
1. Physical properties of CO₂ and other reservoir fluids at in situ conditions.	
Equations of State (EOS) for CO₂	3
2. Modelling AVA coefficients at the top of CO₂ accumulations	7
2.1 Modelling procedure and main assumptions	8
2.2 Effective properties of pore fluids	9
2.3 Amplitude versus angle analysis	11
2.3.1 P-wave reflection curves	13
2.3.2. The influence of temperature and pressure	14
2.3.3 AVA coefficients versus partial CO ₂ saturation at different conditions	18
2.3.4 Effect of the EOS	18
2.3.5 Shear wave conversion	22
2.4 Conclusions	22
3. Modelling of velocity dispersion and attenuation in fractal patchy saturated media: mesoscopic effects, numerical upscaling.	26
3.1 Motivations	26
3.2 Review of Biot's theory	29
3.3 The equations of motion	30
3.4 Description of the numerical method to obtain the equivalent complex moduli ...	31
3.5 Validation of the procedure	35
3.6 A Monte Carlo approach to obtain the average equivalent complex moduli	38
3.7 Applications and Conclusions	39
4. Finite element numerical simulation of the propagation and attenuation of seismic wavefields in CO₂ bearing media	42
4.1 Methodology	43
4.2 Validation of the numerical procedure	44
4.3 Application to seismic modelling in a CO ₂ injection site	45
4.4 Conclusions	51
5. A finite element method to model attenuation and dispersion effects in highly heterogeneous fluid-saturated porous media	53
5.1 Proposed methodology	54
5.2 Memory variables and equation of motion	57
5.3 Application to seismic modelling in the Atzbach-Schwanenstadt injection site	59
5.4 Atzbach-Schwanenstadt geological model	59

5.5 Seismic properties of pore fluids and rocks	60
5.6 P-wave velocity and quality factor	62
5.7 Simulations	64
5.8 Conclusions	66
6. Seismic characterization of thin beds containing patchy carbon dioxide-brine distributions	68
6.1 Introduction	68
6.2 Viscoelastic behavior of rocks containing heterogeneous CO ₂ -brine distributions .	70
6.3 Equivalent viscoelastic solids for the Utsira Sand containing patchy CO ₂ -brine distributions	71
6.4 Seismic response of a CO ₂ -bearing thin bed	76
6.4.1 Methodology	76
6.4.2 Numerical experiments: Elastic versus viscoelastic models	78
6.5 Prestack spectral inversion of seismic data for the characterization of CO ₂ -bearing thin beds	80
6.6 Results and discussion	81
6.7 Conclusions	86
References	89

Summary

This progress report describes the main research activities carried out at Universidad Nacional de La Plata, Argentina, since September 2007 to present date (March 2010).

After an initial stage in which we investigated about the generalities of the seismic monitoring of underground carbon dioxide accumulations and the physical characterization of the gas and reservoir fluids using different models and equations of state, our work was directed to the development of different numerical applications related to the seismic monitoring of the CO₂ migration.

We developed a procedure for the evaluation of mesoscopic attenuation and velocity dispersion in heterogeneous formations. These effects are related to the dissipation of seismic energy due to wave-induced fluid flow. For this study, we considered the case of patchy CO₂ saturation in a brine saturated background. The problem involves the determination of effective complex plane wave and shear moduli in a highly heterogeneous fluid-saturated porous solid employing finite element based upscaling procedures. This method resembles laboratory compressional and shear tests on rock samples. The spatial heterogeneities in saturation are represented by means of stochastic fractals, which also encouraged us to implement this method in a Monte Carlo fashion. Our work also includes a parametric analysis as function of the spatial distribution and saturation levels of CO₂ in different geologic formations and the design of efficient iterative solvers to determine the complex effective moduli at each frequency. A closely related problem was the representation of the viscoelastic moduli previously obtained using linear viscoelastic models.

The effective moduli obtained in this way were next used to perform finite element numerical simulations of seismic wavefields (snapshots and traces) in CO₂ saturated geological formations using viscoelastic wave equations, to analyze the effect of this kind of accumulations on the amplitude and attenuation of seismic waves. This procedure is computationally more efficient than solving Biot's equations of motion due to the extremely fine meshes that would be necessary to represent properly the mesoscale heterogeneities and the large number of degrees of freedom involved.

Another subject investigated is related to the modelling of the P-wave reflection coefficient at the interface between a cap rock (such as a shale layer) and a layer saturated by a mixture of CO₂ and brine or oil at liquid, supercritical and gaseous conditions, using a Biot-Gassmann formulation. The variations in the reflection coefficients vs. angle of incidence (AVA) are commonly used in reservoir geophysics to obtain information about the rocks and pore fluids. For this analysis we assumed a long term injection so that it is reasonable to consider that the gas is uniformly distributed within the pore space of the rock forming a layer of thickness

large compared to the seismic wavelengths. We performed a sensitivity analysis of the standard AVA coefficients (the so called intercept, gradient and curvature) in the near offset range, to investigate whether they can be useful to study the properties of horizontal CO₂ accumulations such as saturation, pressure and temperature.

On the other hand, our group developed an efficient pre-stack spectral inversion procedure (based on the Simulated Annealing algorithm) for the characterization of thin layers and the determination of thickness, P and S wave velocities and bulk density. The feasibility and potential application of this technique to the problem of CO₂ monitoring was analyzed using synthetic gathers.

1 Physical properties of CO₂ and other reservoir fluids at in situ conditions. Equations of State (EOS) for CO₂

As is well known, for modelling purposes it is necessary to compute the physical properties of the different fluids involved in the CO₂ sequestration procedure at variable formation temperature (T) and pressure (P). With this idea one of the first steps in our work consisted in the implementation of empirical models and state equations to compute density, bulk modulus (or alternatively compressibility) and viscosity of hydrocarbon oil and gas, brine and CO₂.

Carbon dioxide and hydrocarbon gases behave as real gases, whose density and compressibility can be computed using EOS. The corresponding properties of CO₂ (density and bulk modulus) for variable temperature and pressure can be computed using some of the general equations of state (EOS) developed for real gases such as [72] or [52] [40], or some more specific such as [68] or [22]. To our knowledge, there is not a full agreement yet in geophysical literature about which EOS is the most appropriate to represent CO₂ properties at the temperatures and pressures found in geologic reservoirs. Among the different existing models we implemented and compared the following ones

- Van der Waals (1873), involving two-parameters,
- Duan et al. (1992), involving fifteen-parameters,
- Xu (2002) formulas, based on Batzle & Wang (1992) laws, and
- Peng-Robinson (1976, 1978), involving two parameters.

In many cases (except for Duan et al. EOS), the range of validity in the $T - P$ plane is uncertain. Comparing the results obtained with the different models with real data [73] as shown in Figures 1 and 2, we found that for pressures below the critical point for CO₂ (7.4 MPa) the different results are in good agreement, with higher discrepancies for supercritical pressures. In that range Duan et al. and Peng Robinson EOS give a more accurate density representation. However, important discrepancies are observed in the adiabatic bulk modulus computations K_A , which are mainly due to an improper calibration of the γ constant relating isothermal to adiabatic modulus K_I :

$$K_A = \gamma K_I$$

Velocity measurements in rock samples of Utsira sandstone saturated with CO₂ and other geologic formations involved in the project would be very useful to improve this calibration.

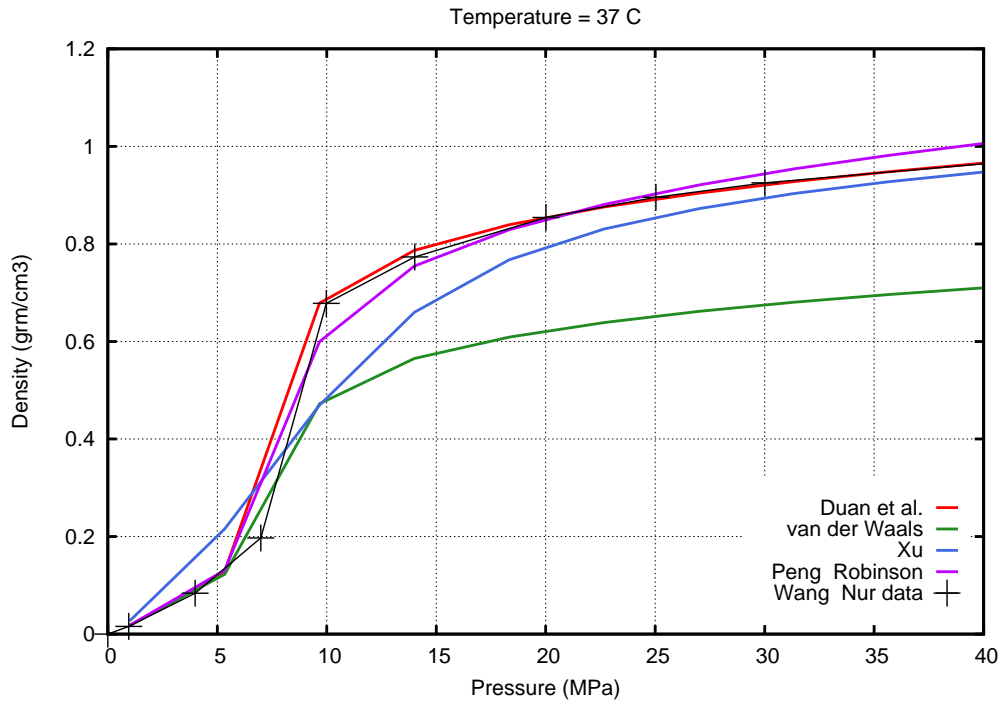


Figure 1: CO₂ density versus pressure for a fixed temperature according to the different models

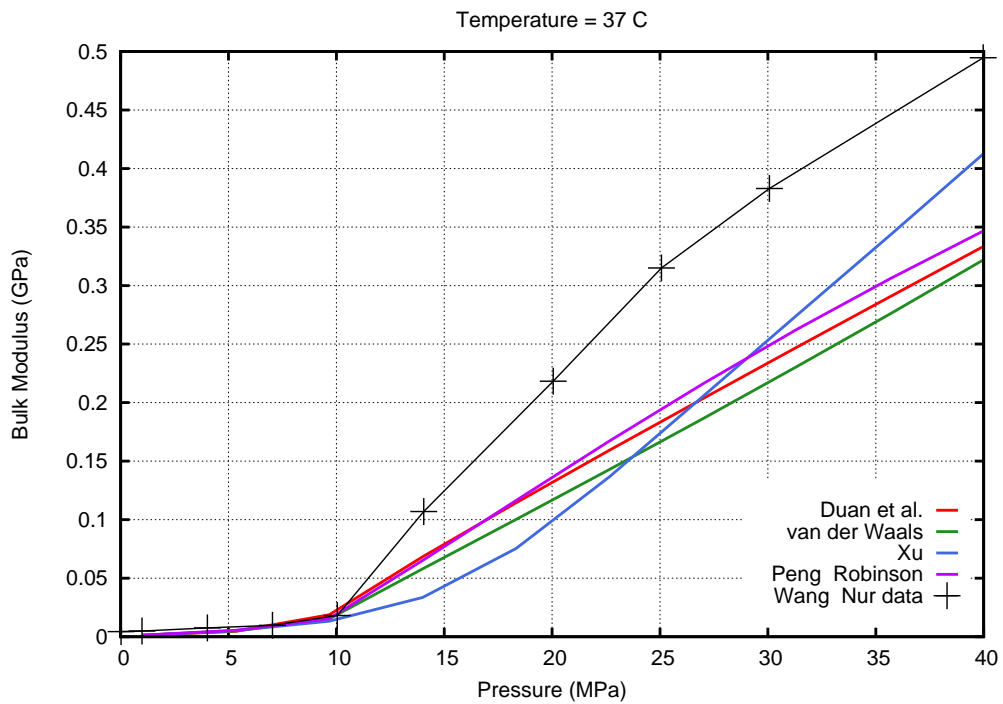


Figure 2: CO₂ bulk modulus versus pressure for a fixed temperature according to the different models

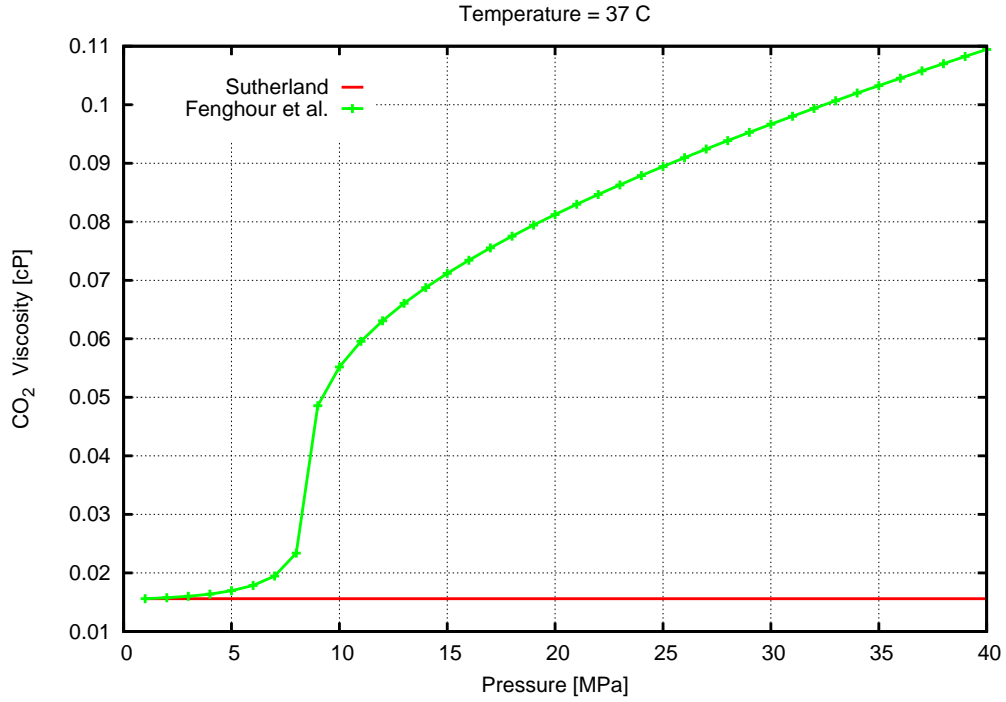


Figure 3: CO₂ viscosity versus pressure for a fixed temperature according to Sutherland formula and Fenghour et al. empirical models.

Other physical parameter of CO₂ is the viscosity, which can be computed using Sutherland temperature dependent formula. Alternatively, we used the formulas derived by [25] from laboratory experiments, who found that CO₂ viscosity depends not only on temperature but also on pressure. In Figure 3 we compare the behavior of both models, which are in good agreement only for low pressures. However it must be emphasized that for frequencies in the seismic range the influence of the effective viscosity in seismic velocities and reflection coefficients is minor.

Also, using Duan et al. (1992) equations we computed the solubility of CO₂ in brine under different physical conditions and brine salinity. Our aim is to analyze whether dissolution effects are important as trapping mechanism. In Figures 4 (a)-(b) we show some computations. These results allow us to conclude that the volume fraction of CO₂ dissolved in brine seems not to be significant at the supercritical temperature and pressure conditions usually present in CO₂ sequestration injection sites.

For simplicity, in the absence of measurements the density, bulk modulus and viscosity of brine for given in situ temperature and pressure conditions are computed using the classic [6] empirical relations.

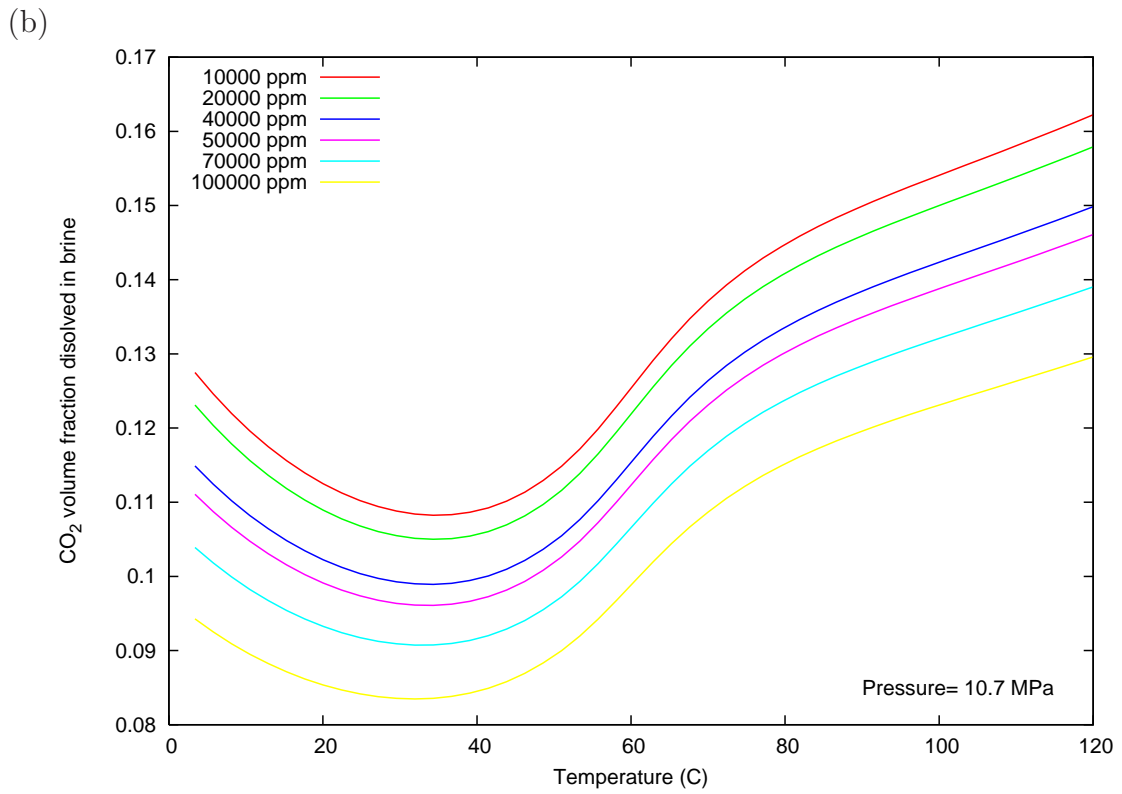
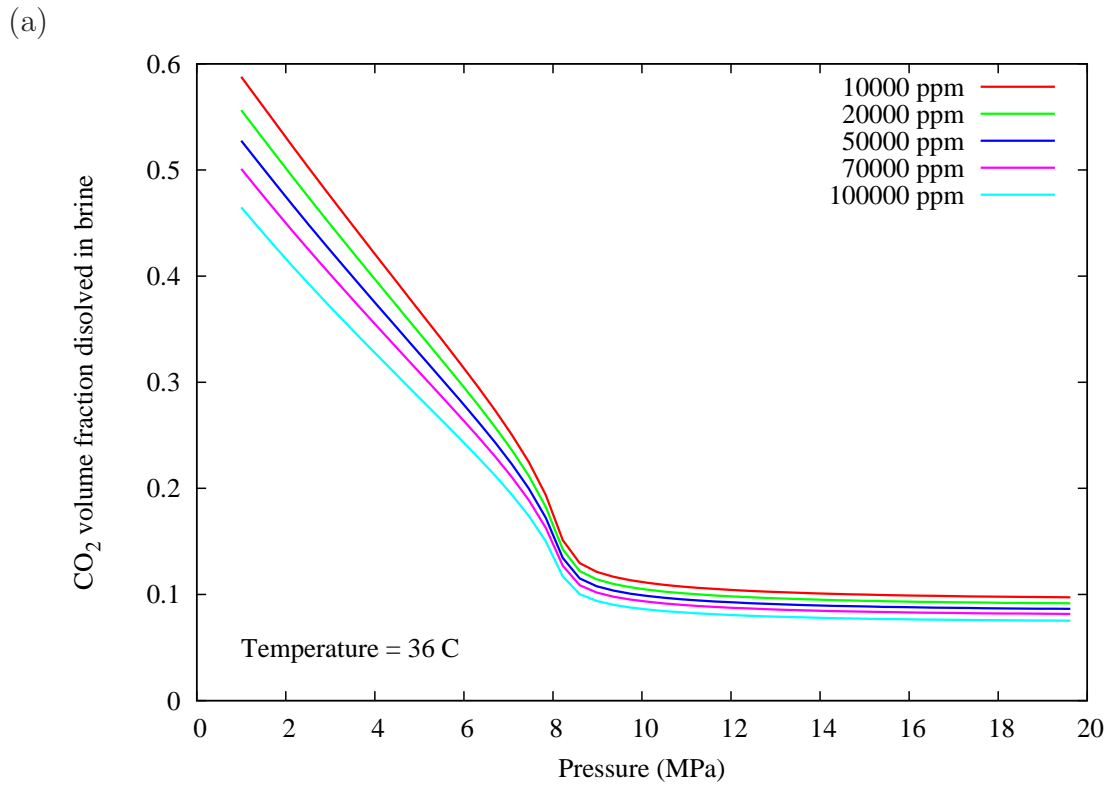


Figure 4: CO₂ solubility versus pressure and temperature according to Duan et al (1992) model.

2 Modelling AVA coefficients at the top of CO₂ accumulations

Carbon dioxide is released into our atmosphere during hydrocarbon production and mainly when carbon-containing fossil fuels such as oil, natural gas, and coal are burned during combustion. As a result of the world-wide consumption of such fossil fuels, the amount of CO₂ in the atmosphere has largely increased over the past century. It is now widely accepted that the continued increase in CO₂ concentration is a major agent in global climate change.

Many carbon dioxide capture and storage projects are being developed worldwide to reduce the emission of greenhouse gases in the atmosphere as a way to mitigate climate changes in a transition period towards the use of more sustainable energies, in accordance with the objectives of Kyoto agreement. The sequestration and geological storage of CO₂ in many cases is a feasible option to accomplish this goal, giving rise to the science of CO₂ *sequestration*, a new challenge for governments, scientists and engineers [58]. However this practice requires a careful surveillance to prevent this greenhouse gas from seeping back to the atmosphere.

In most cases, the appreciable contrast between the physical properties of natural reservoir fluids and those of carbon dioxide allows the utilization of 4D seismic methods as a monitoring tool of the spatio-temporal distribution of this substance after the injection. Very good illustrations of this technique are described by [1], [17] and [2] at Sleipner injection field (North Sea, Norway), among other works. While it is accepted that 4D seismic methods are able to monitor the presence or absence of CO₂, their ability to quantify the saturation and state of this fluid within the reservoir is still under discussion. This makes necessary to search for reliable seismic indicators for CO₂ saturated geological formations.

It is widely recognized that the dependence of seismic reflection amplitude versus offset from source to receiver (AVO) or equivalently, amplitude variations with ray angle (AVA) are important tools for reservoir lithology and fluid characterization. With this idea, [10] suggested an AVO based method to monitor both presence and degree of CO₂ saturation. They showed that variations in the best-fitting AVO parameters, A (intercept), B (gradient) and C (curvature) [43], before and after CO₂ injection may be seismically noticeable. More recently, [32] presented an AVO model in brine reservoirs oriented to the identification of CO₂ - brine interfaces. However, none of these works take into account the high variability of the many parameters and state variables involved in CO₂ sequestration problems. This led us to model the seismic P-wave reflection coefficient at the top of a layer containing mixtures of CO₂ and brine or oil, for variable saturations and different in situ pore pressure and temperature conditions (e.g. in cold and warm basins). These results then allowed us to perform a parametric analysis on the corresponding AVO parameters.

From these experiments we conclude that the intercept parameter shows a monotonic decreasing behavior, with very strong variations with respect to the pre-injection state and for low CO₂ saturations, showing slower changes at higher saturations. The gradient parameter also decays substantially for low CO₂ saturations, showing changes of trend for saturations in the intermediate range. The third AVO parameter (curvature term), related to the far offset information, is less sensitive to saturation, showing changes that in some cases may be well below the seismic resolution. We also found remarkable differences between the P-wave reflection coefficient curves for liquid CO₂ and those obtained for gaseous and supercritical states.

Our modeling results indicate that, under certain conditions, it would be possible to use seismic parameters not only to establish bounds on CO₂ saturation levels but also to characterize the physical state of this substance in subsurface accumulations and leakages at different depth levels.

2.1 Modelling procedure and main assumptions

The formulation and solution of the energy and amplitude splitting problem when a monochromatic plane compressional P-wave strikes obliquely at a plane interface between two isotropic porous saturated homogeneous halfspaces was treated by different authors, such as [20], [24], [64] and [59]. Following the ideas in those papers, in this work the mechanical behavior of the porous media is described in terms of the classic constitutive relations and equations of motion given by [8, 9]. At the interface, two reflected compressional waves (fast and slow) and a shear wave are generated, and the same holds for the transmitted waves. However, it must be remarked that when a low frequency seismic wave propagates through a porous saturated medium, due to fluid viscosity both constituents (solid and fluid) move in phase, and consequently the model response is equivalent to that resulting from the formulation given by [27]. In this connection, since in this work we are interested in frequencies within the seismic range, we can neglect slow wave conversion and focus in the fast P-wave reflection coefficient, hereafter denoted by R_{pp} . Nevertheless, and only for some particular situations, we also analyze the shear wave reflection coefficient denoted by R_{ps} .

It is assumed that the *mixture* of CO₂ and brine or CO₂ and reservoir oil can be treated as a viscous single phase fluid, as explained in the next section. We also consider that CO₂ is uniformly distributed within the pore space in one of the halfspaces, forming a layer of thickness larger than the wavelengths of the incident waves. The computation of seismic reflection coefficients for the case of thin layers or spatially variable CO₂ distribution (such as patchy saturation) would require a more complex treatment.

In general, the presence of intrinsic dissipation in this kind of media leads to a complex

frequency dependent reflection coefficient, which produces changes in amplitude and phase of the reflected waves [59]. Given that for the applications we are only considering viscous friction effects associated to Biot's global flow, which are negligible at low frequencies, the imaginary parts of the reflection coefficients result several orders of magnitude lower than the real parts. Consequently, for practical purposes they will be omitted.

To complete the model description, it is important to remark the assumption of no chemical interactions between the pore fluids and the frame, which allows us to employ the fluid substitution procedure to consider that the pore space is saturated by brine or oil and CO₂ in variable proportions. Variations of rock matrix elastic properties with effective pressure (related to the difference between confining and pore pressure), are not taken into account either. However, knowing the experimental effective pressure laws for the rocks under consideration would allow us to incorporate this effect in the computations [59].

2.2 Effective properties of pore fluids

We study the injection of a volume of carbon dioxide V_{CO_2} in a geologic reservoir in which the pore volume V_p at the pre-injection state is fully saturated by liquid reservoir fluids such as brine or oil. We assume that CO₂ displaces, without dissolution, part of such fluids giving rise to a two-phase fluid saturation. Then, if we denote the CO₂ saturation as

$$S_g = \frac{V_{CO_2}}{V_p}, \quad (1)$$

and if S_l denotes liquid saturation (corresponding to brine or oil), the following relationship holds:

$$S_l + S_g = 1. \quad (2)$$

We suppose that the fluid phase in the pore space can be described as a single-phase *mixture* of liquid and gas, whose effective physical properties can be obtained by means of the following rules:

$$\text{mass density } \rho_f^* = S_l \rho_l + S_g \rho_g \quad (\text{weighted average}), \quad (3)$$

$$\text{bulk modulus } \frac{1}{K_f^*} = \frac{S_l}{K_l} + \frac{S_g}{K_g} \quad (\text{isostress Reuss average}), \quad (4)$$

$$\text{viscosity } \eta^* \simeq \eta_g \left(\frac{\eta_l}{\eta_g} \right)^{S_l}, \text{ Teja and Rice (1981) [69]}, \quad (5)$$

where ρ_l, ρ_g are the individual liquid and gas densities, η_l, η_g their viscosities and K_l, K_g the corresponding bulk moduli. For the present analysis we leave out capillary pressure effects.

The density, bulk modulus and viscosity of brine and oil for given in situ temperature and pressure conditions are computed using [6] empirical relations. For the computations we consider a typical brine salinity of 50000 ppm. and a light oil with reference density $\rho_0 = 0.78$ gr/cm³, according to the notation used by [6], equivalent to an API gravity equal to 49.91.

The corresponding properties of CO₂ (density and bulk modulus) for variable temperature and pressure can be computed using some of the general equations of state (EOS) developed for real gases such as [72] or [52] [40], or some more specific such as [68] or [22]. To our knowledge, there is not a full agreement yet in geophysical literature about which EOS is the most appropriate to represent CO₂ properties at the temperatures and pressures found in geologic reservoirs. Then for our computations we employ the fifteen-parameter EOS given by [22], valid for pressures in the range 0-800 MPa and temperatures from 0 to 1000 °C, which guarantees a suitable representation of CO₂ properties at different states. In some cases, for comparison we also used the well known [72] cubic EOS.

To estimate CO₂ viscosity we used the formulas derived by [25] from laboratory experiments, who found that CO₂ viscosity depends not only on temperature but also on pressure. However it must be emphasized that for frequencies in the seismic range the influence of the effective viscosity in seismic velocities and reflection coefficients is minor.

Depending on the in situ pressure and temperature conditions CO₂ can exist at the underground in different physical states. We recall that its *critical point* occurs at a temperature $T_c = 31.1$ °C and a pressure $P_c = 7.39$ MPa. For pressures $P < P_c$ and $T < T_c$ CO₂ behaves as *vapour* and for $P < P_c$ and $T > T_c$ as a *gas*. For $T < T_c$ and $P > P_c$ CO₂ is a liquid. At temperatures higher than T_c and pressures higher than P_c CO₂ is said to be at *supercritical* state, where it is compressible like a gas but with the density of a liquid. This important characteristic of CO₂ behavior is particularly relevant for its underground storage since supercritical CO₂ is capable to fill the available volume with minimum buoyancy effects [5]. Temperatures and pressures near the critical point commonly occur in applications involving CO₂, such as enhanced oil recovery techniques and sequestration projects [44]. However, as pointed out by [5], the depth at which CO₂ supercritical conditions are met is highly variable and strongly dependent on surface temperature and geothermal gradients, even within a single basin. In addition, the pressure regime of the basin (normal or abnormal), is also very important and is related to its geologic history, existence of sealing faults, permeability barriers and the occurrence of overpressure generation mechanisms [51].

2.3 Amplitude versus angle analysis

Variations in the reflection coefficients with angle of incidence are commonly used in reservoir geophysics to infer properties about the lithology and fluid type of reservoir rocks [4, 43]. In this work, we investigate whether AVA coefficients can be usefully applied to the characterization of CO₂ accumulations, a problem of particular relevance for monitoring lateral migrations across permeable layers.

For the applications we consider a 50 Hz plane P-wave striking the horizontal interface between a porous poorly consolidated sandstone, with high porosity and permeability, i.e. with good storage capacity, overlain by a shale layer acting as sealing rock. For the sandstone we consider the following parameters, taken from [24]: porosity 30%, permeability 1 Darcy, solid grain bulk modulus 35 GPa, frame bulk and shear moduli 1.7 GPa and 1.855 GPa and grain density 2.65 gr/cm³. The corresponding properties of the upper shale layer are: porosity 25%, permeability 0.001 Darcy, solid grain bulk modulus 20 GPa, frame bulk and shear moduli 3.11 GPa and 1.528 GPa and grain density 2.45 gr/cm³. The shale rock is assumed to be fully saturated with brine and the sandstone is assumed to be saturated by mixtures of brine and CO₂, in one case, and mixtures of oil and CO₂ in another case, in variable volumetric proportions.

In the near offset domain or below the critical angle, we assumed that the R_{pp} reflection coefficient as a function of the incidence angle θ can be approximated in the usual form:

$$R_{pp}(\theta) \simeq A + B \sin^2\theta + C (\tan^2\theta - \sin^2\theta), \quad (6)$$

where the coefficient A is the so called *intercept*, B the *gradient* and C the *curvature*. The intercept is equal to the normal incidence reflection coefficient and is controlled by the contrast in acoustic impedance between both media. The gradient is more complex in terms of rock properties and is related to contrasts in density, in compressional and shear wave velocities [4]. The third parameter is important at far offsets and near the critical angle, in case it exists [43]. Equation (6) can be used to carry out a parametric analysis on the A , B and C coefficients to study their sensitivity at different saturation levels by implementing a standard fitting procedure on the results obtained for $R_{pp}(\theta)$.

With the aim of analyzing the behavior of the seismic reflectivity at different scenarios, in the following numerical experiments we consider variable CO₂ saturations, ranging from 0 to 100%, and different physical states (supercritical, gaseous and liquid), according to the location of the temperature and pressure pairs in the CO₂ phase diagram. A linear relationship between in situ temperature and pressure can be obtained by assuming that the pore pressure at any depth z is hydrostatic, i.e. $P = \rho_w g z$, where ρ_w is formation water density and g gravity.

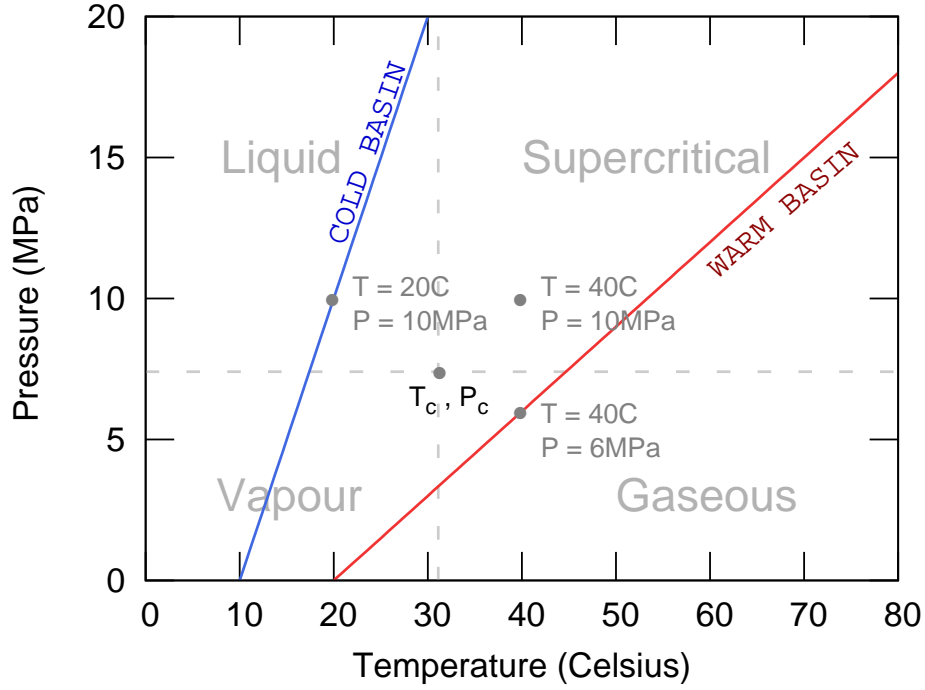


Figure 5: Schematic temperature vs. Pressure diagram and phase behavior of CO₂ .

Also, considering a surface temperature T_0 and a geothermal gradient G , so that $T = T_0 + G z$, it is straightforward that

$$P = \left(\frac{\rho_w g}{G} \right) (T - T_0). \quad (7)$$

According to [5], we can distinguish *warm* basin conditions, where the trajectory in the P vs. T diagram is to the right of the critical point and goes through the gas and supercritical regions. The opposite geothermal conditions, defined as *cold*, are those in which the line P vs. T is to the left of the critical point and passes through the vapor and liquid regions, as illustrated in Figure 5.

The values of the physical properties of CO₂ at the different states are given in Table 1.

	CO ₂	Brine	Oil
<i>Gaseous CO₂</i> $T = 40\text{ }^\circ\text{C}$ $P = 6\text{ MPa}$	$K = 0.0049\text{ GPa}$ $\rho = 0.1498\text{ gr/cm}^3$ $\eta = 0.1787\text{ }10^{-3}\text{ Poise}$	$K = 2.5986\text{ GPa}$ $\rho = 1.0287\text{ gr/cm}^3$ $\eta = 0.785\text{ }10^{-2}\text{ Poise}$	$K = 1.2175\text{ GPa}$ $\rho = 0.7714\text{ gr/cm}^3$ $\eta = 0.01985\text{ Poise}$
<i>Supercritical CO₂</i> $T = 40\text{ }^\circ\text{C}$ $P = 10\text{ MPa}$	$K = 0.01397\text{ GPa}$ $\rho = 0.6452\text{ gr/cm}^3$ $\eta = 0.4963\text{ }10^{-3}\text{ Poise}$	$K = 2.6234\text{ GPa}$ $\rho = 1.0304\text{ gr/cm}^3$ $\eta = 0.7849\text{ }10^{-2}\text{ Poise}$	$K = 1.2640\text{ GPa}$ $\rho = 0.7742\text{ gr/cm}^3$ $\eta = 0.01985\text{ Poise}$
<i>Liquid CO₂</i> $T = 20\text{ }^\circ\text{C}$ $P = 10\text{ MPa}$	$K = 0.0931\text{ GPa}$ $\rho = 0.8535\text{ gr/cm}^3$ $\eta = 0.8089\text{ }10^{-3}\text{ Poise}$	$K = 2.5009\text{ GPa}$ $\rho = 1.03607\text{ gr/cm}^3$ $\eta = 0.01101\text{ Poise}$	$K = 1.4319\text{ GPa}$ $\rho = 0.7879\text{ gr/cm}^3$ $\eta = 0.05002\text{ Poise}$

Table 1. Physical properties of brine, oil and CO₂ at different physical states, according to Batzle and Wang (1992), Duan et al (1992) and Fenghour et al.(1998).

2.3.1 P-wave reflection curves

The set of plots in Figure 6 (a)-(c), show the general behavior of R_{pp} as a function of incidence angle for fixed saturations and three CO₂ states, considering also the case of CO₂ injection in brine and oil. Hereafter, according to the scheme in Figure 1, for the gaseous state (see Figure 6(a)) we consider a pore pressure $P = 6\text{ MPa}$ and a temperature $T = 40^\circ\text{C}$, a condition that could be found within a warm basin at shallow depths (below 1 Km). We also analyze the seismic reflectivity in the liquid region (Figure 6(c)), by taking $P = 10\text{ MPa}$ and $T = 20^\circ\text{C}$, a possible case in a cold basin at about 1 Km depth. An intermediate situation, of great practical interest, is that of supercritical CO₂ (Figure 6(b)), which is analyzed by taking $P = 10\text{ MPa}$ and $T = 40^\circ\text{C}$. In the graphs we restricted the angles to the $0\text{-}30^\circ$ interval (near offset range). And, given the abrupt change observed in the reflection coefficients from pre-injection (i.e. for 0% CO₂ saturation) to post-injection states, we decided not to show in the figures the curves of 0% CO₂ saturation to obtain a scale more convenient to direct the attention on the changes of R_{pp} with CO₂ saturation, an effect that in general is not strong.

The set of curves shown for fixed saturations 10, 20, 60 and 100% show an AVA class III behavior, according to standard AVA classification [16]. In particular, the plots corresponding to brine at supercritical state are similar to those recently published by [28] for Utsira sandstone. As expected, due to the low impedance of the lower medium we obtain a negative reflection

coefficient for normal incidence becoming more negative for higher angles. However, as will be evident later, for saturations lower than 10% and for some physical states a different AVA class can be found.

For both types of reservoir fluids we observe that the minimum reflection coefficients (in absolute value) are obtained for liquid CO₂ due to its high density and bulk modulus in this state, having a lower contrast with respect to the physical properties of the reservoir fluids. However, the R_{pp} coefficient for liquid CO₂ allows a better discrimination of saturation degree than in the other physical states under consideration. Except for the gaseous state, for the same degree of saturation, R_{pp} is more negative for CO₂-oil mixtures than for CO₂-brine mixtures. In the supercritical and gaseous states variations with saturation are small and are associated with changes in the second decimal place.

2.3.2 The influence of temperature and pressure

Considering uncertainties in the in-situ formation temperature and pore pressure and to assess its influence on the seismic reflectivity, in Figures 7 and 8 we plot the variations of R_{pp} with those state variables, assuming that they vary independently. We restricted to $\theta = 30^\circ$ and a limited number of CO₂ saturations.

In Figure 7 we show the model computations for a fixed supercritical pressure $P = 10$ MPa, and temperatures ranging from 10 to 50°C, where we can see that for both reservoir fluids and for temperatures lower than 45°C the reflection coefficient becomes more negative with increasing temperature. The most pronounced changes are observed for the minimum saturations with an average change of 23% every 10 °C for 10% saturation in brine and about 18% every 10 °C for oil.

The curves of R_{pp} vs. pressure for a supercritical temperature $T = 40$ °C (Figure 8) show an almost constant behavior with pressure, with a noticeable change of trend at about 9 MPa, associated to the transition zone from gaseous to supercritical CO₂ (which was also corroborated using [72] EOS). For the case of 10% saturation we found a change of 18% from 9 to 12 MPa for brine and 16% for oil. Similar results were also found for normal incidence.

From both Figures 7 and 8 we observe that for higher CO₂ saturations smaller variations with pressure and temperature are observed. These results also prove the necessity of accurate estimations of pressure and temperature for a proper calibration of theoretical models and real time lapse seismic data, particularly at the early stages of injection, in which the errors could be significant.

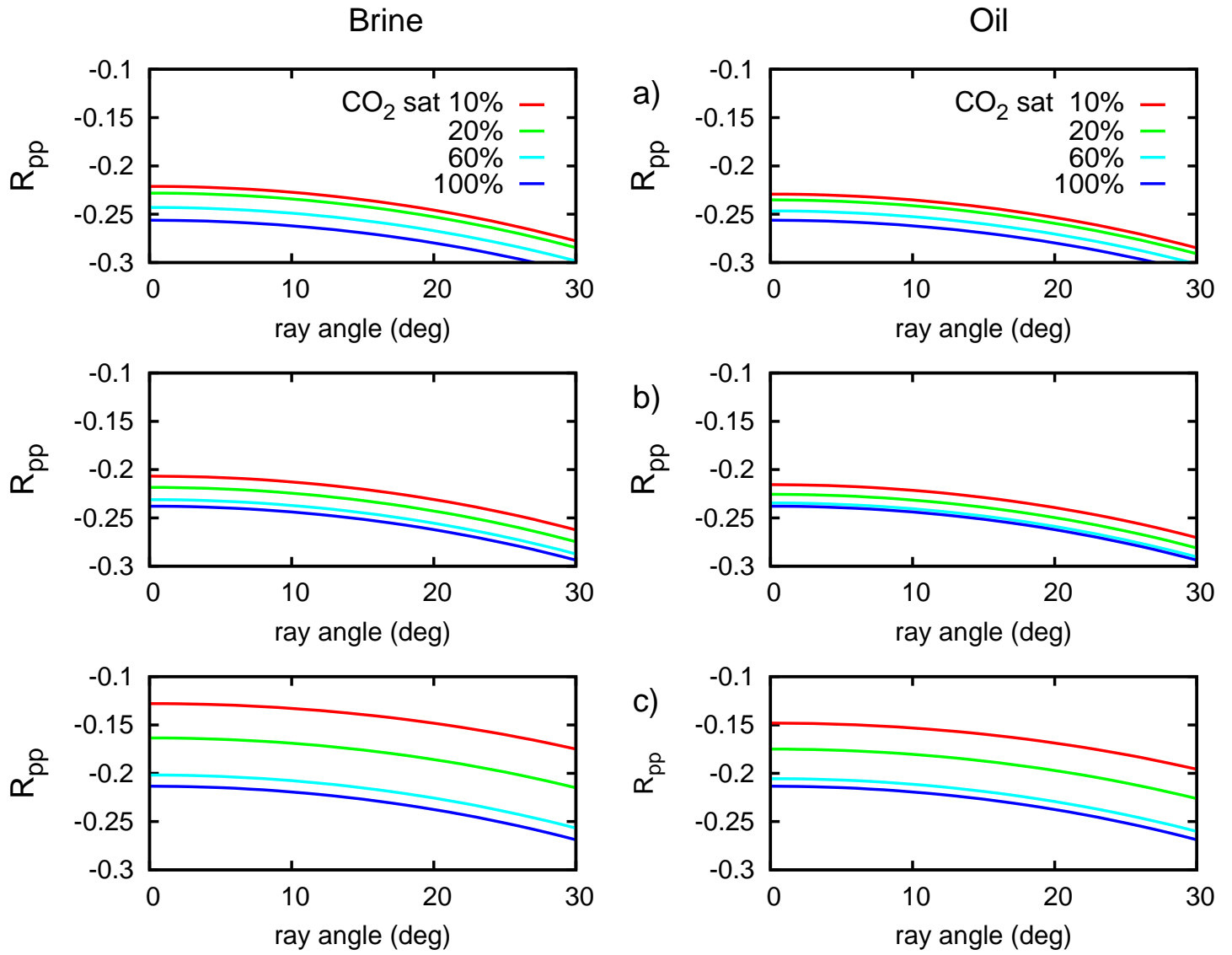


Figure 6: P-wave reflection coefficient vs. ray angle for brine-CO₂ mixtures (left) and oil-CO₂ mixtures (right) for: a) gaseous CO₂ , b) supercritical CO₂ and c) liquid CO₂ conditions.

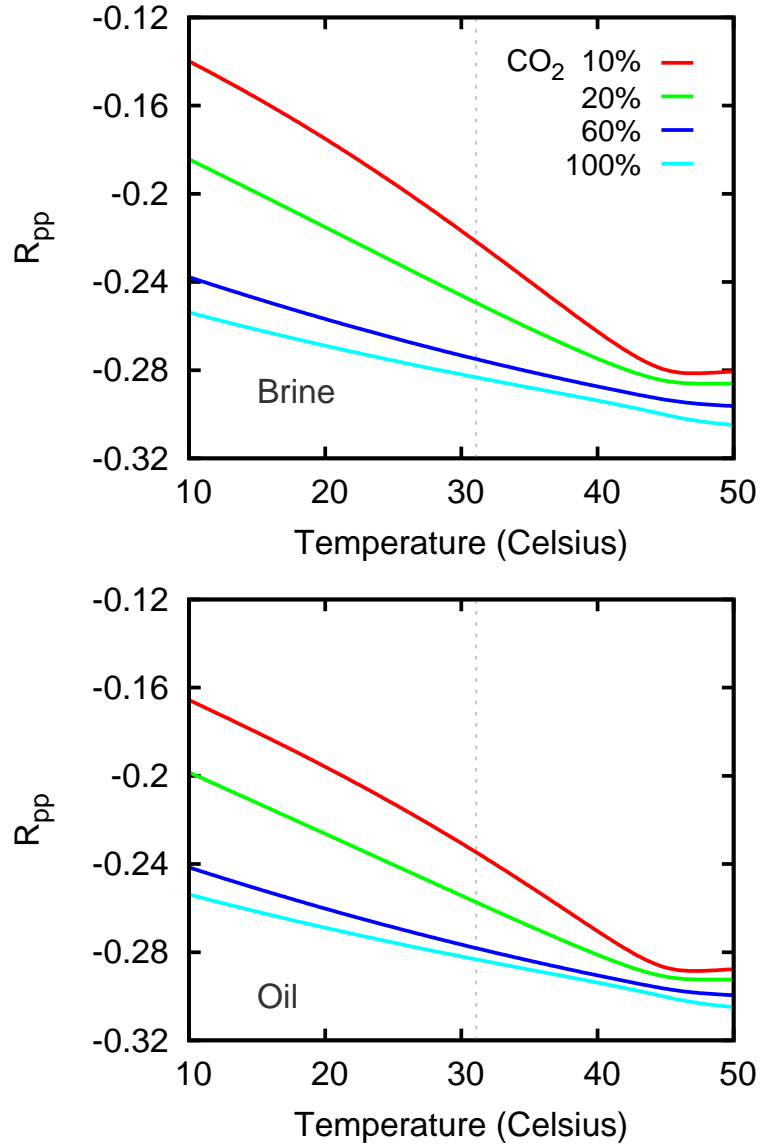


Figure 7: P-wave reflection coefficient versus formation temperature for fixed pressure $P = 10$ MPa. The dotted vertical line denotes the critical temperature at $T_c = 31.1^\circ\text{C}$.

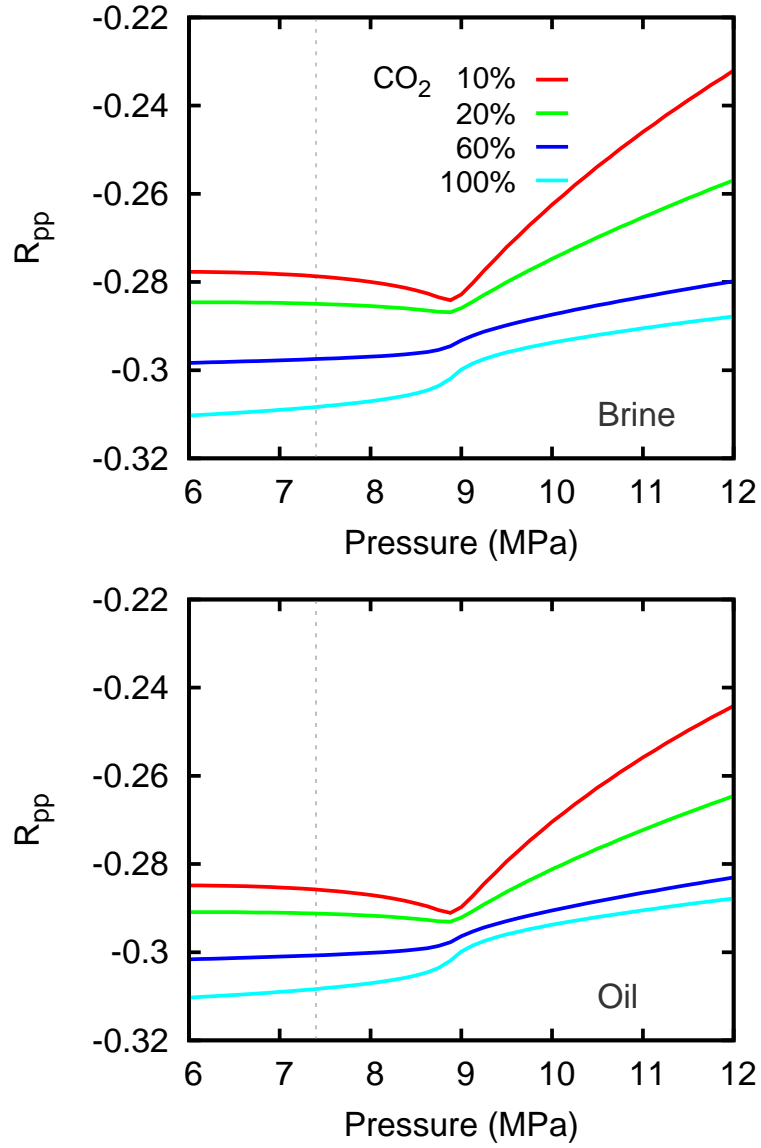


Figure 8: P-wave reflection coefficient versus pore pressure for fixed temperature $T = 40$ MPa. The dotted vertical line denotes the critical pressure at $P_c = 7.39$ MPa.

2.3.3 AVA coefficients versus partial CO₂ saturation at different conditions

In the next set of Figures (9, 10 and 11) we plot the coefficients A , B , C to study their sensitivity at different saturation levels, by fitting equation (6) to the numerical results obtained for $R_{pp}(\theta)$. As stated previously, due to the large variation of these parameters with respect to the pre and post-injection states, we excluded from the figure saturation levels lower than 5%, to accentuate the variations at higher saturations, which in general are small. From this analysis we found that the intercept parameter A , shows a monotonic decreasing behavior for the three states under consideration. These variations are more pronounced for CO₂ in liquid state, with significant percentage changes in the range from 5 to 40%, which for a better interpretation are indicated in the graph. It can be seen that they are greater than 100% for CO₂-brine and greater than 60% for CO₂-oil mixtures.

In the same saturation range the variation of A for supercritical and gaseous CO₂ is much lower but still noticeable for the reservoir fluids considered. This allows us to distinguish clearly the liquid state from the other two, in which the overall behavior is the same but with less significant changes. It is worthwhile to mention that for the particular case of liquid CO₂ and for saturations lower than 5%, the intercept takes slightly negative values, consistent with an AVA Class II case.

Regarding the gradient B , it can be seen that it is always negative showing a trend similar to that of the intercept, except for the gaseous CO₂ state, in which an opposite trend is observed. The most significant variations take place for CO₂ in liquid state (the percentage variations are indicated in the figure).

With regards to the curvature coefficient C , for both fluid types, we only found significant changes on the order of 10% for CO₂ at the liquid state and for saturations in the range 0-40%. For the other states the variations are much lower than 2%. The correct determination of such small changes may be strongly limited by the seismic resolution. In this sense, [10] point out that AVA variations on the order of 5% are seismically detectable. Using this numerical threshold we can state that variations in the parameter C do not bring much information and consequently an AVO analysis based solely on A and B may be sufficient.

2.3.4 Effect of the EOS

In Figure 12 we illustrate coefficients A , and B vs. CO₂ saturation, comparing the results obtained using [72] and [22] equations of state. For brevity, we only show the results corresponding to mixtures of CO₂ with brine at supercritical conditions. As stated previously, we excluded of the figure CO₂ saturations lower than 5% to enhance the small discrepancies between the curves. From the results we observe for CO₂ saturations under 20% an almost perfect

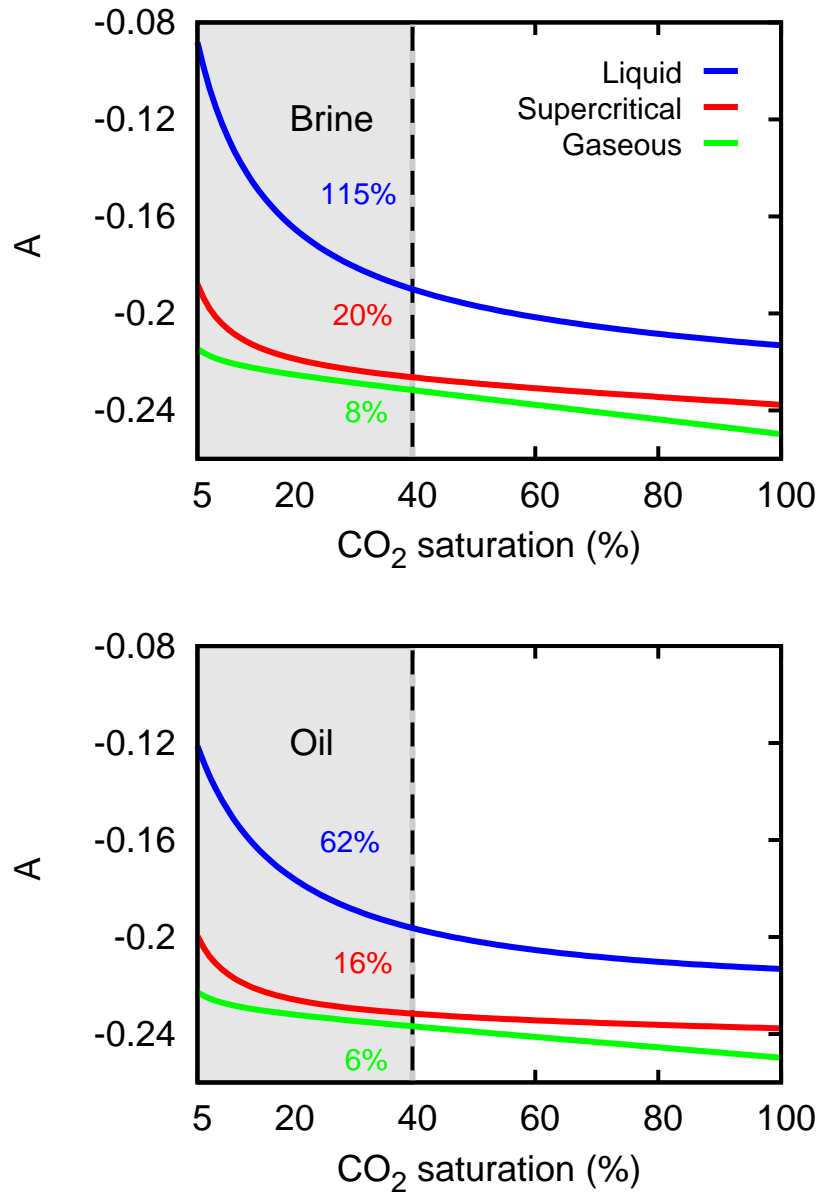


Figure 9: Behavior of intercept A versus CO_2 saturation for brine- CO_2 mixtures (top) and oil- CO_2 mixtures (bottom) at the different physical states. The percentage variations in the interval 5 to 40 % are indicated in the plot.

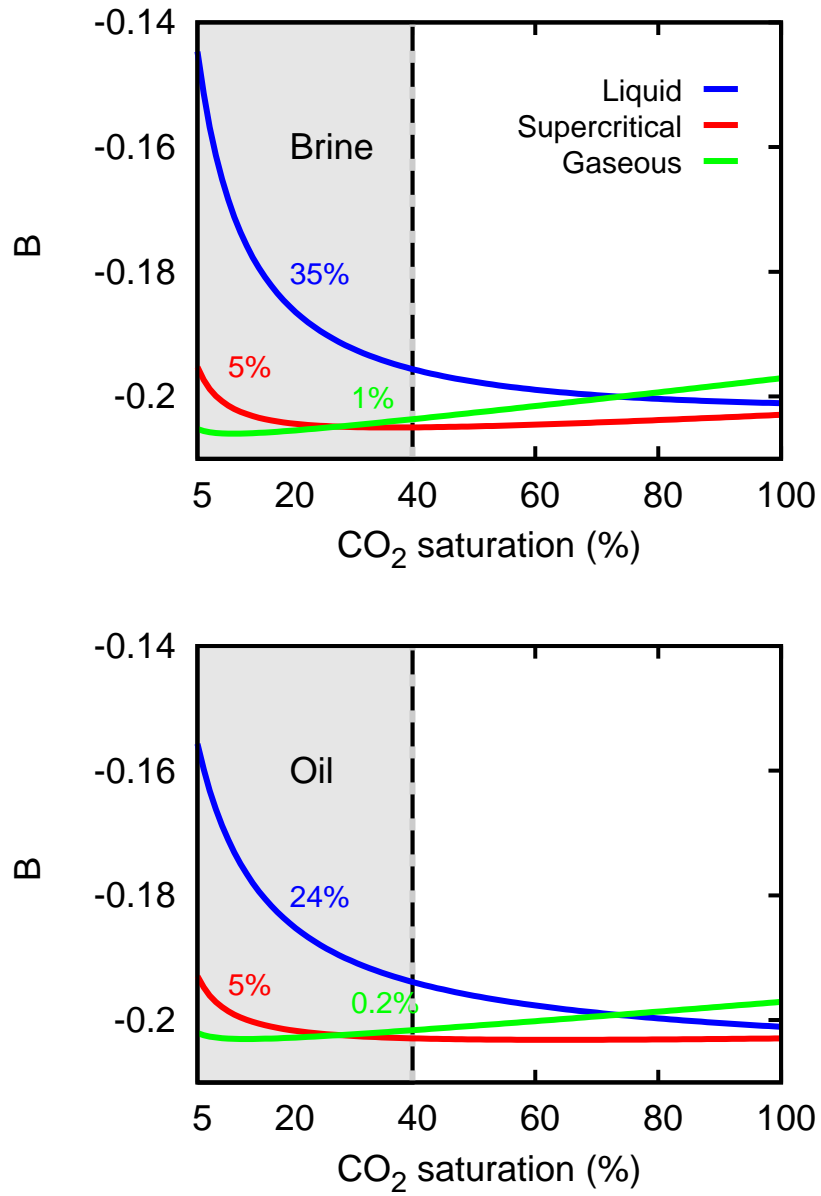


Figure 10: Behavior of gradient B versus CO_2 saturation for brine- CO_2 mixtures (top) and oil- CO_2 mixtures (bottom) at the different physical states. The percentage variations in the interval 5 to 40 % are indicated in the plot.

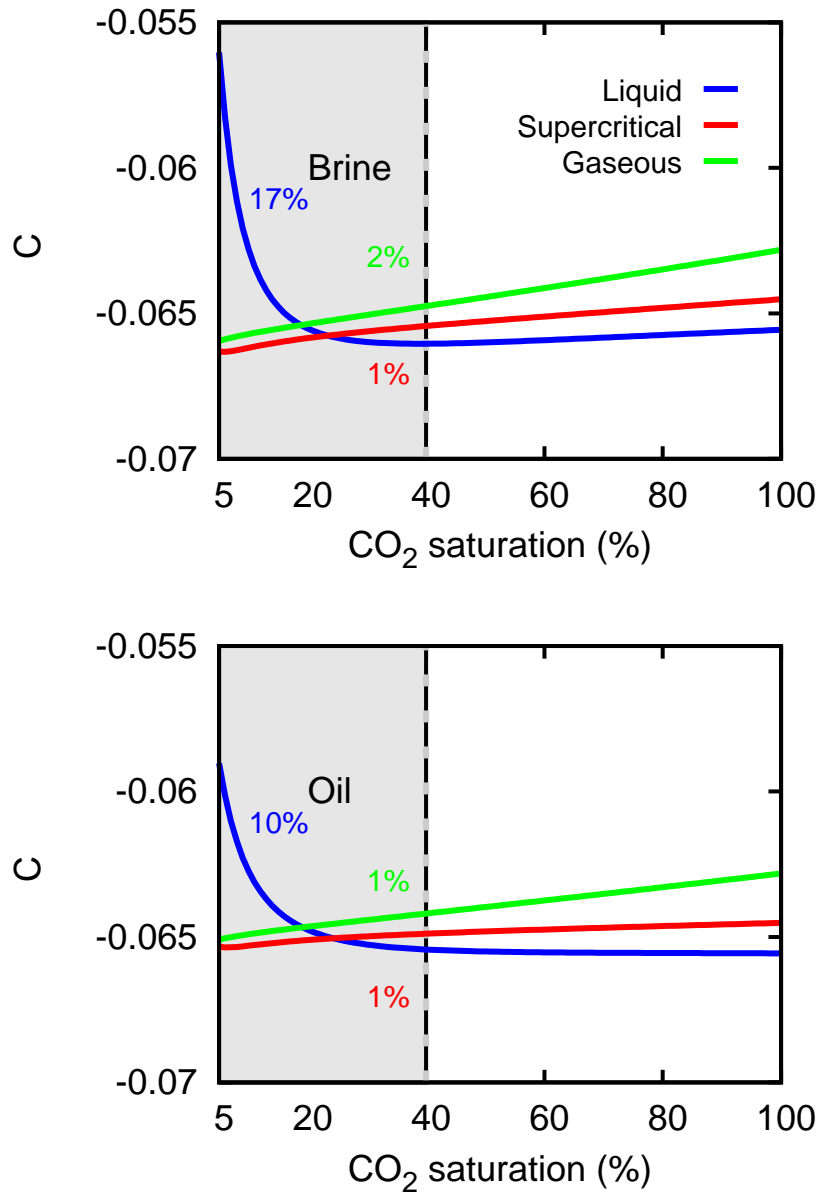


Figure 11: Behavior of coefficient C versus CO_2 saturation for brine- CO_2 mixtures (top) and oil- CO_2 mixtures (bottom) at the different physical states. The percentage variations in the interval 5 to 40 % are indicated in the plot.

agreement, while for higher saturations A is slightly underestimated when using [22] EOS and B results slightly overestimated. However, the discrepancies are lower than 3%. Equivalent conclusions are obtained for the other physical states. From these experiments we can conclude that for seismic modelling applications the choice of an EOS should not be a main concern since it does not change significantly the results.

2.3.5 Shear wave conversion

Here we investigate whether shear wave reflections at the top of the CO₂ accumulation could be used for monitoring purposes. With this motivation we modeled the shear wave reflection coefficient $R_{ps}(\theta)$ for mixtures of CO₂ with brine or oil at the different physical conditions under consideration. In Figure 13 we show R_{ps} for angles in the range 0-90° for the case of gaseous CO₂ injected in brine. Although the amount of energy conversion from compressional to shear wave mode is very low, we remark that for this particular case R_{ps} at far offsets is very sensitive to saturation degree, which is observed for brine and also for oil. For a saturation change from 10 to 100% this coefficient shows a decrease on the order of 60%. For supercritical CO₂ the curves show smaller differences while at the liquid state they are almost independent of saturation. The same behavior is obtained for R_{ps} in the case of CO₂-oil mixture, with values slightly lower than those in the previous case. They are not included for the sake of brevity.

2.4 Conclusions

We have analyzed the behavior of the compressional and shear wave reflection coefficients vs. angle of incidence at the top of a plane CO₂ accumulation within a poorly consolidated sandstone. Taking different temperatures and pore pressures corresponding to gaseous, supercritical and liquid states, we have also modelled the variations of the AVA parameters A, B, C with CO₂ saturation. Appreciable differences between the reflection coefficient in the different states were observed.

From this analysis we conclude that the intercept parameter A shows a monotonic decreasing behavior, with very strong and rapid variations with respect to the pre-injection state. This is also observed in the low saturation range, while much slower changes are found for higher saturations. The gradient parameter B also decays strongly for low CO₂ saturations even showing slight changes of trend for saturations in the intermediate range, particularly for gaseous CO₂. The most pronounced changes of these parameters with CO₂ saturation are observed for CO₂ at liquid state, a condition that can be met in cold basin scenarios. The curvature parameter C does not bring much more information about saturation, since in most cases its variations

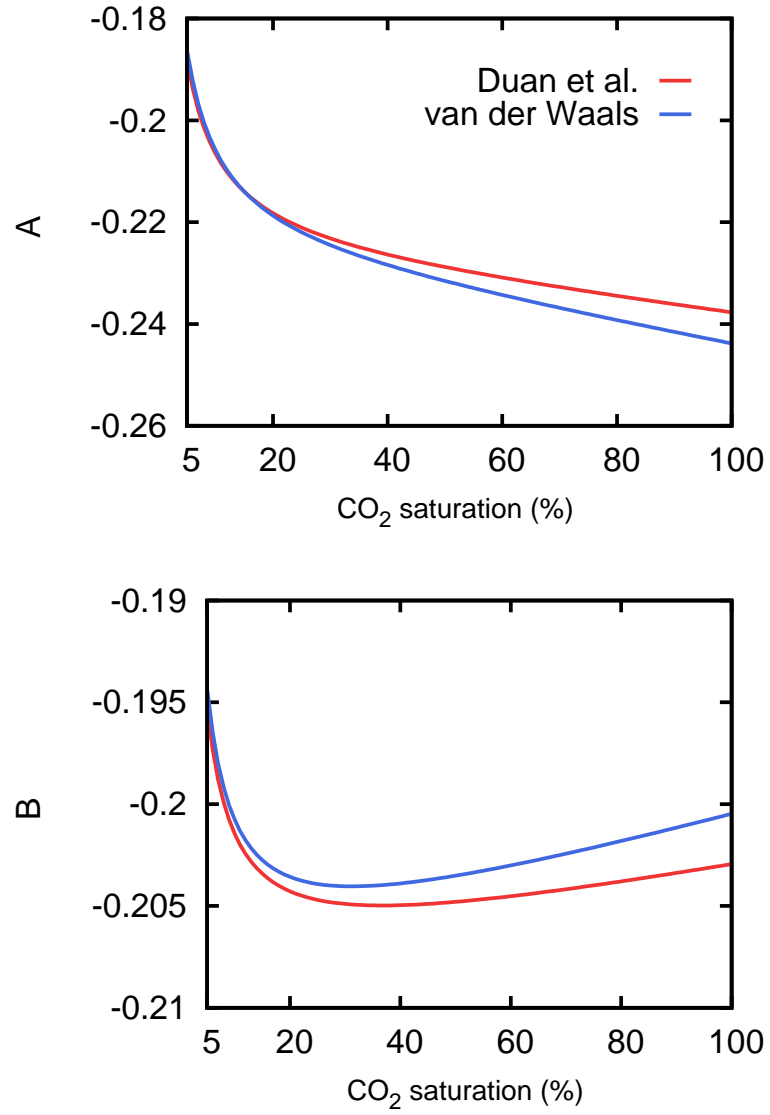


Figure 12: Comparison of A and B versus CO_2 saturation for brine- CO_2 mixtures using [72] and [22] EOS at CO_2 supercritical conditions.

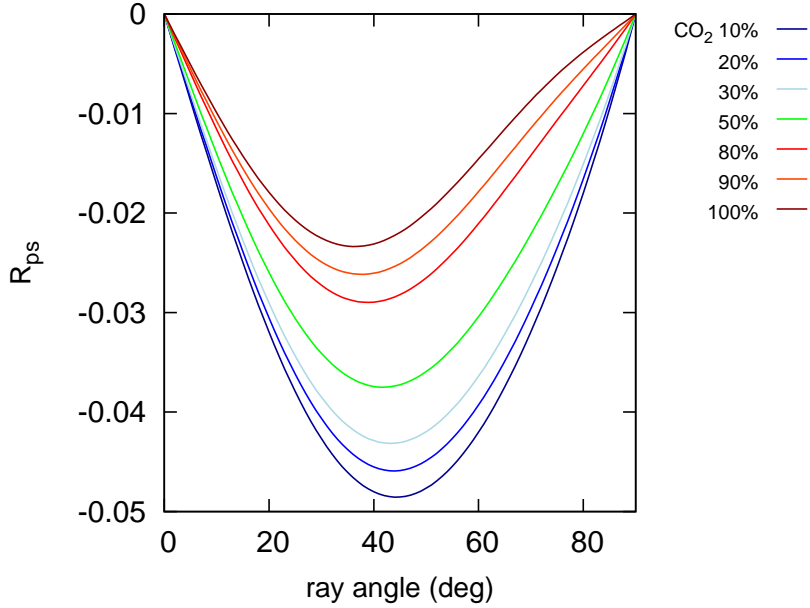


Figure 13: Shear-wave reflection coefficient vs. ray angle for brine-CO₂ mixtures at gaseous CO₂ conditions for different fixed saturations.

are smaller than those observed in *A* and *B*. In all cases analyzed the relative changes of *A*, *B* and *C* at saturations higher than about 40% are considered to be unimportant. The lack of sensitivity of AVA parameters in that saturation range imposes a serious limitation to any attempt to quantify CO₂ saturation degree using AVA information.

In some cases, reservoir temperature and pressure uncertainties can lead to significant errors in the modelled reflection coefficients, particularly at low CO₂ saturations. However, variations in AVA coefficients derived from implementing different equations of state for carbon dioxide are not significant.

With regards to the shear wave reflection coefficient at the top of the accumulation, we found that the amount of energy conversion from compressional to shear wave mode is low but particularly sensitive to saturation for gaseous CO₂ injected in brine or oil.

Our results suggest the possibility of using seismic reflection data to characterize the physical state of the CO₂ accumulated into brine or oil reservoirs, even with normal incidence data only. Moreover, the study of changes in AVA parameters over time may help to establish bounds on CO₂ saturation degree particularly at the early stages of accumulation below the cap-rock, assuming uniformly distributed CO₂. We remark the need of a careful analysis about the quality, resolution and processing of the seismic data. This is essential to obtain meaningful estimations of the AVA coefficients and to assess the significance of the relative changes observed in the parameters, which in some cases may be at the edge of conventional seismic resolution.

The results presented in this Section 2 were also included in the following paper:

Seismic reflectivity analysis in carbon dioxide accumulations, by Claudia L. Ravazzoli and Julián Gómez,
submitted to Journal of Applied Geophysics on 28/09/2009.

3 Modelling of velocity dispersion and attenuation in fractal patchy saturated media: mesoscopic effects, numerical upscaling

Different theoretical and laboratory studies on the propagation of elastic waves in real rocks have shown that the presence of heterogeneities larger than the pore size but smaller than the predominant wavelengths (mesoscopic-scale heterogeneities) may produce significant effects in the attenuation and velocity dispersion of seismic waves. Such phenomena are known as “mesoscopic effects” and are due to equilibration of wave-induced fluid pressure gradients. In this work we present a numerical upscaling procedure to obtain equivalent viscoelastic solids for heterogeneous fluid-saturated rocks. It consists in simulating oscillatory compressibility and shear tests in the space-frequency domain, which enable us to obtain the equivalent complex undrained plane-wave and shear moduli of the rock sample. The behavior of the porous media is assumed to obey Biot’s equations, and a finite-element procedure is used to approximate the solutions of the associated boundary value problems. Also, since at mesoscopic scales rock parameter distributions are generally uncertain and of stochastic nature, we propose to apply the compressibility and shear tests in a Monte Carlo fashion. This facilitates the definition of average equivalent viscoelastic media by computing the moments of the equivalent phase velocities and inverse quality factors over a set of realizations of stochastic rock parameters described by a given spectral density distribution. We present numerical examples in which we first analyze the sensitivity of the mesoscopic effects to different kinds of heterogeneities in the rock and fluid properties. Next, we illustrate the application of the Monte Carlo procedure for the particular case of quasi-fractal heterogeneities.

3.1 Motivations

Seismic velocities and absorption properties of rocks are key-parameters in the characterization of their properties, and permit to obtain valuable information such as lithology, types of saturating fluids, physical state and degree of saturation. Consequently, the understanding of the physics controlling these parameters is of great interest for theoretical and exploration geophysics and other branches of science.

One major cause of attenuation in porous media is wave-induced fluid flow, which can take place at microscopic, macroscopic and mesoscopic spatial scales. The attenuation mechanism associated with wave-induced fluid flow at microscopic scales is also known as *local fluid flow* or *squirt flow*, and is due to fluid-filled microcracks which respond with greater fluid pressure

changes than the main pore fluid producing fluid flow and, consequently, energy loss. This loss mechanism is able to explain ultrasonic attenuation data but is incapable of explaining the measured attenuation levels at seismic frequencies [55].

The loss mechanism predicted by the theory of Biot [8, 9], the classical Biot's *global fluid flow* in homogeneous media, has a macroscopic nature and is due to wavelength-scale fluid pressure equilibration between the peaks and troughs of the fast propagating wave. This induces a relative displacement between the solid frame and the fluid, causing energy dissipation due to viscous friction. Although the attenuation due to global flow is generally important in the range of ultrasonic frequencies, it is not significant at the seismic frequency band.

The wave-induced fluid flow at *mesoscopic* scales takes place when a fast wave travels across an heterogeneous porous medium having inhomogeneities larger than the pore size but smaller than the predominant wavelengths. Basically, when a compressional wave squeezes an heterogeneous fluid-saturated porous material, the different regions of the medium, due to their distinct elastic properties, may undergo different strains and fluid pressures. This in turn produces fluid flow and Biot slow waves generating energy loss and velocity dispersion. These effects can also be produced by shear stresses applied to the medium, particularly when the mesoscopic heterogeneities have some local anisotropy associated with its shape [42]. Recent results have demonstrated the importance of the mesoscopic effects in the context of exploration geophysics, being the dominant P-wave attenuation mechanism in reservoir rocks at seismic frequencies ([55]).

White and coauthors [74, 75] were the first to model the wave-induced fluid flow produced by mesoscopic-scale heterogeneities, showing that this mechanism can produce important attenuation and velocity dispersion effects at seismic frequencies in partially saturated rocks. They obtained approximated solutions of the response of plane porous layers alternately saturated with gas and water [74] and of spherical gas pockets in a water-saturated porous rock [75]. These works established the physical equivalence between the behavior of the low-frequency fast Biot's waves in the presence of meso-scale heterogeneities and that of a viscoelastic solid at a larger scale. Since then, many authors have made very important contributions to a better understanding of this subject using a great variety of methods.

In this sense, we can mention the work of [54] who obtained an analytical model for the seismic response of a mixture of two different porous phases having a single dominant length scale, while [49] and [29] focused on the case of layered porous media. The case of irregular patchy saturation received great interest during the last decade with important works such as that published by [34], who developed a general analytical solution for arbitrary geometries. Some years later, [46] analyzed the asymptotic behavior of attenuation and dispersion versus frequency in different random porous media. On the other hand, [70] presented a comparative

review of different models and analyzed the effect of random discrete and continuous fluid distributions. More recently, these authors ([71]) assessed the mesoscopic effects in the case of continuous random fluid distributions and [47] focused on fractal fluid distributions.

Mesososcopic effects have also been studied by performing numerical simulation of wave propagation, such as in [30] and [61], among others. However, this methodology is computationally expensive or even not feasible due to different reasons. First, very fine meshes are needed to represent the inhomogeneities. In addition, in the low frequency range the resolution of the diffusion process associated with the fluid pressure equilibration is a critical issue, since the diffusion length is very small as compared with the seismic wavelengths.

To overcome these limitations, a different and very interesting approach was recently presented by [42]. In their work, a time-varying stress is applied to the boundaries of an heterogeneous sample and by numerically computing the average stress and strain fields its effective complex moduli are determined.

First, we present an alternative methodology to obtain the *equivalent* compressibility and shear complex moduli of heterogeneous rock samples. Such moduli are obtained by defining an equivalent viscoelastic solid with the same attenuation and velocity dispersion as that of the fast compressional (or shear) wave in the original fluid-saturated porous rock. We emphasize that, since a viscoelastic solid is neither able to represent the propagation of both fast and slow waves nor support fluid flow through it, this equivalence is not complete and must be understood in the previously mentioned sense. The properties of the viscoelastic model are obtained by applying time-harmonic compressibility and shear stresses to a representative sample of bulk material, which are mathematically represented as local boundary value problems stated in the space-frequency domain. Biot's theory is used to model the response of the heterogeneous material to the applied stresses, and the approximate solution is obtained using a finite-element procedure. We validate the methodology by comparison with previously published theoretical results.

Since at mesoscopic scales rock parameter distributions are generally uncertain due to their high degree of spatial variability and the fact that direct observations are not possible, a second goal arises. It consists in representing the heterogeneities as stochastic functions and applying the before-mentioned numerical experiments in a Monte Carlo fashion. Such approach enables us to obtain the *average equivalent* complex plane-wave and shear moduli of highly-heterogeneous fluid-saturated porous media, as well as their corresponding variances. These moduli and variances represent the statistical properties of the response of a set of rock samples containing stochastic multi-scale heterogeneities described by a given spectral density distribution and facilitate the analysis of the effects of the spatial variability on the seismic response of these kind of media.

We present numerical examples in which we first perform a parametric study to analyze the sensitivity of the mesoscopic effects to different types of heterogeneities in the fluid and rock properties. Next, we illustrate the application of the Monte Carlo approach to obtain the *average equivalent* moduli and variances in the case that the poroelastic medium contains quasi-fractal stochastic multi-scale heterogeneities.

3.2 Review of Biot's theory

The propagation of waves in a porous elastic solid saturated by a single-phase compressible viscous fluid was first analyzed by Biot in two important classical papers [8, 9,]. He considered a porous isotropic medium saturated by a single-phase, compressible viscous fluid, and assumed that due to deformation the fluid may flow relative to the solid frame causing viscous friction. Let $u^s = (u_i^s)$ and $\tilde{u}^f = (\tilde{u}_i^f)$, $i = 1, \dots, E$ denote the average displacement vectors of the solid and fluid phases, respectively, where E denotes the Euclidean dimension. Also let

$$u^f = \phi(\tilde{u}^f - u^s), \quad (8)$$

be the average relative fluid displacement per unit volume of bulk material, where ϕ denotes the effective porosity. Set $u = (u^s, u^f)$ and note that

$$\xi = -\nabla \cdot u^f, \quad (9)$$

represents the change in fluid content.

Let $\varepsilon_{ij}(u^s)$ be the strain tensor of the solid phase. Also, let σ_{ij} , $i, j = 1, \dots, E$, and p_f denote the stress tensor of the bulk material and the fluid pressure, respectively. Following [9], the elastic stress-strain relations can be written in the form:

$$\sigma_{ij}(u) = 2\mu \varepsilon_{ij}(u^s) + \delta_{ij}(\lambda_c \nabla \cdot u^s - \alpha K_{av} \xi), \quad (10)$$

$$p_f(u) = -\alpha K_{av} \nabla \cdot u^s + K_{av} \xi. \quad (11)$$

The coefficient μ is the shear modulus of the bulk material, considered to be equal to the shear modulus of the dry matrix. We also introduce

$$\lambda_c = K_c - \frac{2}{E}\mu, \quad (12)$$

where K_c is the undrained bulk modulus of the saturated (closed) material. Following [27], the coefficients in expressions 10 and 11 can be obtained from the relations

$$\alpha = 1 - \frac{K_m}{K_s}, \quad (13)$$

$$K_{av} = \left(\frac{\alpha - \phi}{K_s} + \frac{\phi}{K_f} \right)^{-1}, \quad (14)$$

$$K_c = K_m + \alpha^2 K_{av}, \quad (15)$$

where K_s, K_m and K_f denote the bulk moduli of the solid grains, the dry matrix and the saturant fluid, respectively. The coefficient α is known as the effective stress coefficient of the bulk material. It is also convenient to introduce the undrained *plane-wave modulus* M_c , given by

$$M_c = \lambda_c + 2\mu. \quad (16)$$

For the present analysis, we consider that the moduli in the previous expressions are real and frequency independent.

3.3 The equations of motion

Let ρ_s and ρ_f denote the mass densities of the solid grains and the fluid and let

$$\rho_b = (1 - \phi)\rho_s + \phi\rho_f \quad (17)$$

denote the mass density of the bulk material. Let the positive definite matrix \mathcal{P} and the nonnegative matrix \mathcal{B} be defined by

$$\mathcal{P} = \begin{pmatrix} \rho_b I & \rho_f I \\ \rho_f I & g I \end{pmatrix}, \quad (18)$$

$$\mathcal{B} = \begin{pmatrix} 0I & 0I \\ 0I & bI \end{pmatrix}, \quad (19)$$

where I denotes the identity matrix in $\mathbb{R}^{E \times E}$. The mass coupling coefficient g represents the inertial effects associated with dynamic interactions between the solid and fluid phases, while the coefficient b includes the viscous coupling effects between such phases. They are given by the relations

$$b = \frac{\eta}{k}, \quad g = \frac{S\rho_f}{\phi}, \quad S = \frac{1}{2} \left(1 + \frac{1}{\phi} \right), \quad (20)$$

where η is the fluid viscosity and k the absolute permeability. The coefficient S is known as the structure or tortuosity factor, computed according to [7]. Next, let $\mathcal{L}(u)$ be the second-order differential operator defined by

$$\mathcal{L}(u) = (\nabla \cdot \sigma(u), -\nabla p_f(u))^t. \quad (21)$$

Then, if $\omega = 2\pi f$ is the angular frequency, in the absence of body forces, the Biot's equations of motion stated in the space-frequency domain can be written in the form [8, 9,]

$$-\omega^2 \mathcal{P}u(\mathbf{x}, \omega) + i\omega \mathcal{B}u(\mathbf{x}, \omega) - \mathcal{L}(u(\mathbf{x}, \omega)) = 0, \quad (22)$$

where \mathbf{x} denotes the position of an infinitesimal bulk volume in the Cartesian coordinate system. Considering the homogeneous case, it was shown by [8] that in these type of media two compressional waves, denoted here as P1 and P2, and one shear or S wave can propagate. The P1 and S waves correspond to the classical compressional and shear waves propagating in elastic or viscoelastic isotropic solids. The additional P2 slow mode is a wave strongly attenuated in the low frequency range, and it is associated with the motion out of phase of the solid and fluid. In terms of this theory, the physics of the mesoscopic attenuation and dispersion effects in heterogeneous porous media is basically the conversion from fast-wave energy into slow-wave energy at the discontinuities within the rock.

3.4 Description of the numerical method to obtain the equivalent complex moduli

As we mentioned in the introduction, using numerical simulation of wave propagation to study mesoscopic effects is computationally expensive or even not feasible.

A different and very convenient approach to achieve this goal is to apply time-harmonic compressional and shear stresses to a representative sample of a fluid-saturated porous rock, which enables us to obtain its *equivalent* complex plane-wave and shear moduli. This is performed by defining an equivalent viscoelastic medium with the same attenuation and velocity dispersion as the original porous rock. The theoretical basis for this procedure were given in the works of [74, 23] and [34].

This idea is implemented computationally in the 2D case, with the obvious extension to the 3D case. Figure 14 shows a schematic representation of an undrained oscillatory compressibility test, where ν is the unit outer normal on the boundaries of the sample and σ is the stress tensor. In this experiment, the sample is subjected to a time-harmonic compression of the form $\Delta P e^{i\omega t}$ on its top boundary, and no tangential forces are applied on the boundaries of the sample. Also, the solid is neither allowed to move on the bottom boundary nor have horizontal displacements on the lateral boundaries, and the fluid is not allowed to flow into or out of the sample.

Denoting by V the original volume of the sample, its (complex) oscillatory volume change, $\Delta V(\omega)$, enables us to define the *equivalent* undrained complex plane-wave modulus $\overline{M}_c(\omega)$, by using the relation

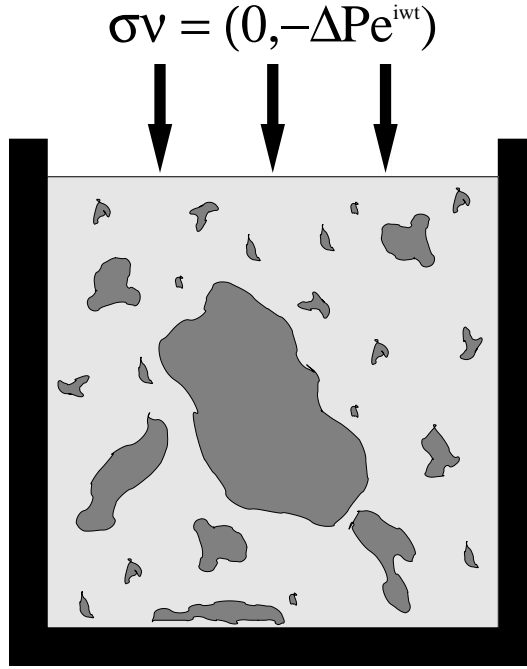


Figure 14: Schematic representation of an oscillatory compressibility test to estimate the equivalent complex plane-wave modulus of a sample.

$$\frac{\Delta V(\omega)}{V} = -\frac{\Delta P}{\overline{M_c(\omega)}}, \quad (23)$$

valid for a viscoelastic homogeneous solid in the quasistatic case.

To estimate the volume change $\Delta V(\omega)$, we consider the solution of equation 22 under the following boundary conditions

$$\begin{aligned} \sigma(u)\nu &= (0, -\Delta P), & (x, y) \in \Gamma^T, \\ \sigma(u)\nu \cdot \chi &= 0, & (x, y) \in \Gamma^L \cup \Gamma^R, \\ u^s \cdot \nu &= 0, & (x, y) \in \Gamma^L \cup \Gamma^R, \\ u^s &= 0, & (x, y) \in \Gamma^B, \\ u^f \cdot \nu &= 0, & (x, y) \in \Gamma^L \cup \Gamma^R \cup \Gamma^B \cup \Gamma^T, \end{aligned} \quad (24)$$

where Γ^L , Γ^R , Γ^B and Γ^T are the left, right, bottom and top boundaries of the domain, respectively. In the expressions 24, χ is a unit tangent on the boundaries of the sample and the factor $e^{i\omega t}$ is omitted, since the problem is formulated in the space-frequency domain.

Assuming that the fluid-saturated porous sample is a square of side length L , the vertical displacements $u_2^s(x, L, \omega)$ on the top boundary Γ^T allow us to obtain its average vertical

displacement $u_2^{s,T}(\omega)$. Then, for each frequency ω , the volume change produced by the compressibility test can be approximated by $\Delta V(\omega) \approx Lu_2^{s,T}(\omega)$. This in turn enables us to compute the equivalent complex plane-wave modulus $\overline{M}_c(\omega)$ by using the relation 23. The corresponding complex compressional velocity is given by ([11])

$$V_{pc}(\omega) = \sqrt{\frac{\overline{M}_c(\omega)}{\overline{\rho}_b}}, \quad (25)$$

where $\overline{\rho}_b$ is the average bulk density of the rock sample. The following relations allow us to estimate the equivalent compressional phase velocity $V_p(\omega)$ and (inverse) quality factor $Q_p(\omega)$ in the form ([11]):

$$V_p(\omega) = \left[\text{Re} \left(\frac{1}{V_{pc}(\omega)} \right) \right]^{-1}, \quad (26)$$

$$\frac{1}{Q_p(\omega)} = \frac{\text{Im}(V_{pc}(\omega)^2)}{\text{Re}(V_{pc}(\omega)^2)}. \quad (27)$$

Following the same methodology, in order to obtain the *equivalent* complex shear modulus of the fluid-saturated porous medium, we apply the numerical shear experiment shown in Figure 15. In this case, the solid is not allowed to move on the bottom boundary of the sample, the fluid is not allowed to flow into or out of the rock and shear stresses are applied on the left, right and top boundaries.

The change in shape of the rock sample permits to recover its *equivalent* complex shear modulus $\overline{\mu}_c(\omega)$ by using the relation

$$\tan(\theta(\omega)) = \frac{\Delta T}{\overline{\mu}_c(\omega)}, \quad (28)$$

where $\theta(\omega)$ is the departure angle between the original positions of the lateral boundaries and those after applying the shear stresses (see, for example, [36]). Equation 28 is valid for a viscoelastic homogeneous solid in the quasistatic approximation.

To estimate the shape change of the rock sample, let us consider the solution of equation 22 under the following boundary conditions

$$\begin{aligned} \sigma(u)\nu &= g(x, y), & (x, y) \in \Gamma^T \cup \Gamma^L \cup \Gamma^R, \\ u^s &= 0, & (x, y) \in \Gamma^B, \\ u^f \cdot \nu &= 0, & (x, y) \in \Gamma, \end{aligned} \quad (29)$$

where

$$g(x, y) = \begin{cases} (0, -\Delta T), & (x, y) \in \Gamma^L, \\ (0, \Delta T), & (x, y) \in \Gamma^R, \\ (\Delta T, 0), & (x, y) \in \Gamma^T, \end{cases} \quad (30)$$

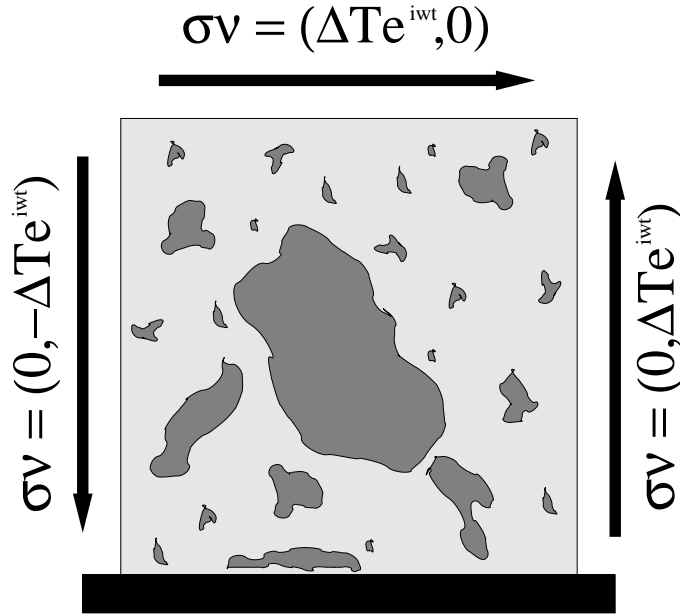


Figure 15: Schematic representation of an oscillatory shear test to estimate the equivalent complex shear modulus of a sample.

and ΔT denotes the constant amplitude of the external oscillatory stress.

The horizontal displacements $u_1^s(x, L, \omega)$ on the top boundary allow us to obtain, for each frequency, its average horizontal displacement $u_1^{s,T}(\omega)$. Then, the shape change of the sample can be approximated by $\tan(\theta(\omega)) \approx u_1^{s,T}(\omega)/L$, which from equation 28 let us estimate $\bar{\mu}_c(\omega)$. The complex shear velocity is given by

$$V_{sc}(\omega) = \sqrt{\frac{\bar{\mu}_c(\omega)}{\rho_b}}, \quad (31)$$

and the equivalent shear phase velocity $V_s(\omega)$ and (inverse) quality factor $Q_s(\omega)$ are estimated using the relations

$$V_s(\omega) = \left[\text{Re} \left(\frac{1}{V_{sc}(\omega)} \right) \right]^{-1}, \quad (32)$$

$$\frac{1}{Q_s(\omega)} = \frac{\text{Im}(V_{sc}(\omega)^2)}{\text{Re}(V_{sc}(\omega)^2)}. \quad (33)$$

In order to estimate these equivalent complex moduli, we use a finite-element procedure to approximate the solution of the equations of motion 22 under the boundary conditions 24 or 29. We use bilinear functions to approximate the solid displacement vector, while a closed subspace of the vector part of the Raviart-Thomas-Nedelec space of zero order ([60, 48]) for the

fluid displacement is employed. Santos et al. [67] show that uniqueness holds for the associated weak forms for $\omega > 0$ and sufficiently small. Also, these authors demonstrate that the error associated with these finite-element problems, measured in the energy norm, is of order of the size h of the computational mesh. The reader is referred to that work for the details of the finite-element procedure.

Concerning the mesh size h , in the low frequency range it has to be small enough so that the diffusion process associated with the fluid pressure equilibration is accurately resolved. For practical purposes, in this work we take h so that the minimum diffusion length is discretized with at least 3 mesh points at the highest frequency, which is sufficient to represent a (smooth) diffusion-type process. In the case that the frequency is above the critical value at which the slow wave becomes a truly propagating wave ([34]), the mesh size should be chosen as usual to avoid improper wavelength sampling.

We wish to emphasize that the size of the rock sample is not arbitrary: it has to be big enough to constitute a representative volume of the medium but, at the same time, it has to be much smaller than the wavelengths associated with each excitation frequency. To find an upper bound for the side length L , we check that the compressibility and shear tests applied to homogeneous samples of side length L , composed of any of the different materials forming the heterogeneous medium, give negligible attenuation and velocity dispersion at the highest frequency under consideration.

3.5 Validation of the procedure

To validate the procedure to estimate the equivalent plane-wave modulus, we assume that the rock sample is composed of two poroelastic layers of equal thickness 0.2 m, one fully saturated with water and the other fully saturated with gas. The physical properties of the solid matrix are taken constant in all the domain, and correspond to the sandstone 1 in Table 2, while the physical properties of the fluids (water and gas) are given in Table 3. The physical properties of the solid grains and those of the fluids were taken from [13]; in addition, following their work, the bulk and shear moduli of the dry matrices were computed using the model of [37], while the Kozeny-Carman relation was employed to relate porosity and permeability. We consider a partition of 75×75 equal square elements to approximate the solutions of the boundary value problems.

Next, we compare the phase velocities and inverse quality factors obtained using our numerical approach for frequencies lying between 0.1 and 100 Hz with the corresponding values obtained using the analytical theory of [75] but, in the last case, considering a periodic medium composed of alternating layers of equal thickness 0.4 m saturated with either gas or water.

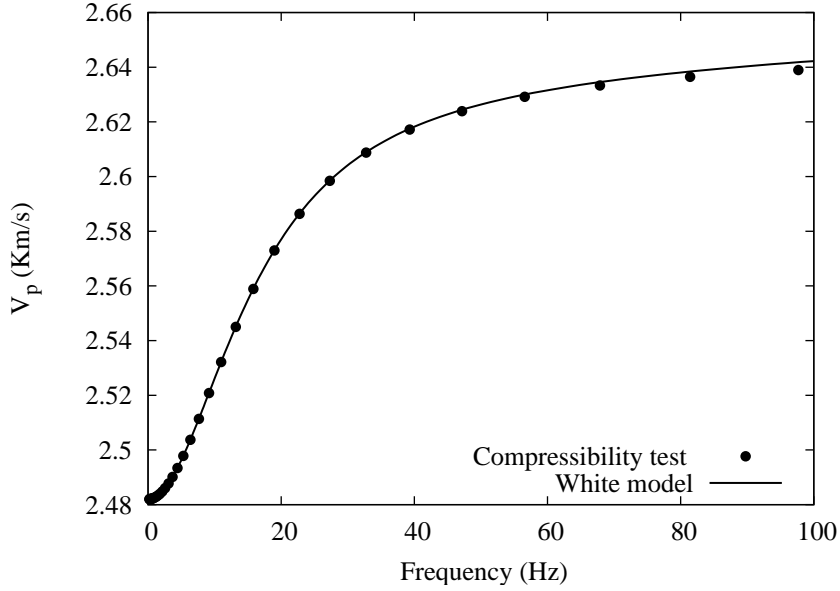


Figure 16: Compressional phase velocity obtained from the compressibility test (dots) and using White’s theory (line) for frequencies lying between 0.1 and 100 Hz.

This comparison is valid because the boundary conditions for the compressibility test can be associated with a compression similar to that proposed by [75], but applied to a periodic sample obtained by a mirror reflection of the rock sample with respect to the x-axis.

Figures 16 and 17 display the compressional phase velocity and inverse quality factor as functions of frequency, respectively, obtained with the compressibility test (dots) and with the White’s theory (line). In both cases an excellent matching between the two approaches can be observed, and the position of the peak in the curve of $\frac{1}{Q_p}$ is in good agreement with the theoretical predictions obtained using concepts from standard diffusion and wave propagation theories [43, 23].

To validate the procedure for the estimation of the equivalent shear modulus, we suppose that the rock sample is composed of two horizontal layers L_1 and L_2 , of thicknesses T_1 and T_2 respectively, such that $T_1 + T_2 = 1$ m. We assume that both layers are saturated with water but their solid matrices are different: the solid matrix of the layer L_1 is the sandstone 1 while the solid matrix of the layer L_2 is shale, with the physical parameters given in Table 2. Then, we verify that the equivalent shear modulus obtained with the shear test for different values of the shale content $T_2/(T_1 + T_2)$ and in the zero-limit frequency is in excellent agreement with that obtained using the Reuss average for an effective mixture of sand and shale [43]. Also, as expected, the imaginary part of the modulus is negligible due to the low frequency used in this experiment. These curves are not shown here for brevity.

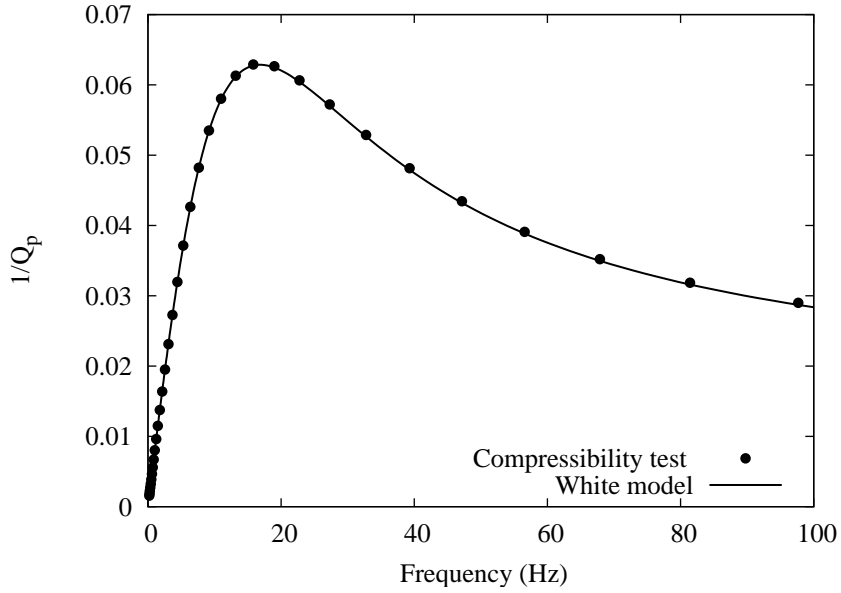


Figure 17: Compressional inverse quality factor obtained from the compressibility test (dots) and using White’s theory (line) for frequencies lying between 0.1 and 100 Hz.

	Sandstone 1	Sandstone 2	Shale
K_s	37 GPa	37 GPa	25 GPa
ρ_s	2650 Kg/m ³	2650 Kg/m ³	2550 Kg/m ³
ϕ	0.3	0.2	0.3
K_m	4.8 GPa	12.1 GPa	3.3 GPa
μ	5.7 GPa	14.4 GPa	1.2 GPa
κ	1 Darcy	0.23 Darcy	1.5×10^{-5} Darcy

Table 2. Physical properties of the solid materials used in the numerical examples.

	Water	Gas	Oil
K_f	2.25 GPa	0.012 GPa	0.7 GPa
ρ_f	1040 Kg/m ³	78 Kg/m ³	700 Kg/m ³
η	0.003 Pa·s	0.00015 Pa·s	0.01 Pa·s

Table 3. Physical properties of the fluids used in the numerical examples.

3.6 A Monte Carlo approach to obtain the average equivalent complex moduli

The compressibility and shear tests defined in the previous section enable us to estimate the equivalent complex moduli of rock samples when the spatial distribution of their properties is known in detail. However, as we mentioned before, a precise knowledge of the spatial distribution of the rock heterogeneities at mesoscopic scales may not be feasible. Instead, they can be represented as stochastic functions (parameters) with given spectral density distributions. For instance, [30] used the von Karman self-similar correlation function to model patchy fluid distributions, while [42] analyzed the behavior of materials having local properties randomly sampled from certain probability distribution functions. This fact suggests the possibility of applying the compressibility and shear tests in a Monte Carlo fashion, i.e., they can be applied to representative samples of bulk material containing stochastic heterogeneities characterized by certain spectral density distribution and the boundary value problems are solved for each realization. This allows us to obtain the *average equivalent* complex moduli for such media, and they represent the statistical behavior of the responses of the rock samples under consideration.

Following this stochastic approach, any given spatial property in the solid or fluid $p(x, y)$ is considered as a sample (or realization) taken at random from an ensemble of a physically meaningful random function $P(x, y, \gamma)$, where γ is the random variable. Using this concept of ensemble allows us to define the statistical properties of the stochastic process $P(x, y, \gamma)$ and of any computed (random) quantity obtained as output of our model. For example, the ensemble mean of $P(x, y, \gamma)$ could be interpreted as the average of repeated measurements of the property.

In our case, a finite set of realizations $P(x, y, \gamma_n)$, $n = 1, \dots, N_R$, is generated using a given spectral density distribution. Next, for each temporal frequency ω and realization γ_n , the phase velocities and inverse quality factors $\beta^n(\omega)$, $\beta = V_p, 1/Q_p, V_s, 1/Q_s$, are random functions and they are determined by taking spatial averages of the computed displacements at certain locations of the domain, as explained in the derivation of formulas 26, 27, 32 and 33. In this procedure we exchange ensemble averages of the computed displacements by their spatial averages and consequently the ergodic hypothesis must be used. This hypothesis ([39]) states that the statistical structure of $P(x, y, \gamma)$ can be obtained by substitution of ensemble averages by spatial averages, and is of common use in geophysical applications. Finally, the means and variances of the random functions $\beta^n(\omega)$, $n = 1, \dots, N_R$ represent the statistical behavior of the response of the fluid-saturated porous rocks under consideration.

To analyze the convergence of the Monte Carlo approach in terms of the number of realiza-

tions N_R , the frequency average of the variances are computed by

$$\| \sigma_{\beta}^2(N_R) \| = \frac{1}{N_F} \sum_{m=1}^{N_F} \sigma_{\beta}^2(\omega_m, N_R), \quad (34)$$

where

$$\langle \beta(\omega_m, N_R) \rangle = \frac{1}{N_R} \sum_{n=1}^{N_R} \beta^n(\omega_m), \quad (35)$$

$$\sigma_{\beta}^2(\omega_m, N_R) = \frac{1}{(N_R - 1)} \sum_{n=1}^{N_R} [\beta^n(\omega_m) - \langle \beta(\omega_m, N_R) \rangle]^2. \quad (36)$$

Following a standard criterion the Monte Carlo simulations are stopped after N_R^* realizations, such that the variances given by the expression 34 of the computed quantities stabilize at constant values. Then, the averages $\langle \beta(\omega_m, N_R^*) \rangle$ define our *average equivalent* phase velocities and inverse quality factors for the heterogeneous fluid-saturated poroelastic material.

The presented methodology was implemented in a serial computer, employing a global solver to find the solutions of the local boundary value problems associated with each realization. Alternatively, each local boundary value problem could be submitted to a different processor in a parallel cluster, in which case a linear speed up behavior would be obtained. An additional reduction in CPU time for the Monte Carlo runs may be achieved by employing for each local boundary value problem a suitable iterative procedure instead of a global solver.

3.7 Applications and Conclusions

In order to analyze the amount of attenuation and velocity dispersion caused by different types of inhomogeneities in the rock frame and fluid properties, we consider some heterogeneous rock samples and obtain their equivalent phase velocities and quality factors. We performed the following experiments:

- A. Sensitivity of the mesoscopic effects to the geometry of the fluid distribution
- B. Sensitivity of the mesoscopic effects to rock permeability
- C. Sensitivity of the mesoscopic effects to fluid viscosity
- D. Sensitivity of the mesoscopic effects to heterogeneities in the fluid and frame properties
- E. Sensitivity of the mesoscopic effects to lithological variations.

We do not include all the results in the report for brevity. The numerical experiments enabled us to obtain the equivalent complex undrained plane-wave and shear moduli of rock samples, as well as the corresponding phase velocities and quality factors. We applied our methodology to diverse 2D rock models to analyze the sensitivity of the mesoscopic effects to

different kinds of heterogeneities in the rock and fluid properties. Although we focused our attention in the seismic range of frequencies, these experiments can also be performed at higher frequencies, as long as the domain size and heterogeneity scales are properly chosen.

Since at mesoscopic scales rock parameter distributions are generally uncertain and of stochastic nature, we proposed to apply the oscillatory tests in a Monte Carlo fashion. This allowed us to define the average equivalent viscoelastic media by computing the moments of the equivalent phase velocities and inverse quality factors over a set of realizations of stochastic rock parameters characterized by a given spectral density distribution. In order to illustrate this procedure, numerical experiments were performed to obtain the average equivalent complex moduli of gas-water patchy-saturated sandstones.

The proposed numerical upscaling procedure can be used to replace a Biot medium containing mesoscopic-scale heterogeneities by an equivalent (or average equivalent) viscoelastic solid, where the mesoscopic effects are included by solving a set of local boundary value problems. This methodology is particularly important in the context of exploration geophysics, since performing numerical simulation of wave propagation employing the viscoelastic equation is computationally much less expensive than any numerical procedure based on the discretization of the full Biot's equations for the same order of accuracy.

The results of this work were published in the following papers:

J. Germán Rubino, Claudia L. Ravazzoli and Juan E. Santos, Equivalent viscoelastic solids for heterogeneous fluid-saturated porous rocks. *Geophysics*, 74(1), N1-N13, (2009). ISSN 0016-8033.

Juan E. Santos, J. Germán Rubino and Claudia L. Ravazzoli, A Numerical Upscaling Procedure to Estimate Effective Plane Wave and Shear Moduli in Heterogeneous Fluid-saturated Poroelastic Media. Publicado en *Computer Methods in Applied Mechanics and Engineering (CMAME)*, 198, 2067-2077, (2009) ISSN: 0045-7825.

J. E. Santos, C. L. Ravazzoli and J. G. Rubino, Statistical analysis of the effective velocity and mesoscopic attenuation in patchy saturated porous media. Society of Exploration Geophysicists, International Exposition and 77th. Annual Meeting, San Antonio, Texas, September 23-28 2007. Expanded Abstracts 26, 2708-2712. ISSN 1052-3812.

J. Germán Rubino, Claudia Ravazzoli, Juan Santos, A numerical procedure to estimate the effective moduli in highly heterogeneous fluid-saturated porous media.

The ideas presented in this Section are applied in next sections to model the seismic response of rocks containing patchy CO₂ distributions.

4 Finite element numerical simulation of the propagation and attenuation of seismic wavefields in CO₂ bearing media

The analysis of attenuation at seismic frequencies due to wave-induced fluid flow caused by mesoscopic-scale heterogeneities has been the object of many studies, such as [74, 56, 46, 41, 13, 61], among others. These heterogeneities in the solid frame and fluid properties, typically on the order of centimeters, are much smaller than the wavelengths of the fast P and S waves travelling in Biot's media. Consequently, the huge number of degrees of freedom (DOF) needed to represent these heterogeneities and their attenuation effects at the macroscale in any finite element or finite difference based numerical procedure employing Biot's equations renders such approach not feasible. In [66] the authors presented a novel numerical upscaling approach to tackle this problem. The idea is as follows: take a representative sample Ω_R of bulk material and perform (local) numerical oscillatory compressibility and shear tests to determine the *equivalent* undrained complex frequency dependent plane wave $M_c(\omega)$ and shear modulus $N(\omega)$ associated with Ω_R in the range of frequencies at which the material is going to be tested by acoustic methods.

These local compressibility and shear oscillatory tests are defined as boundary value problems formulated in the space-frequency domain assuming that the sample obeys Biot's equations of motion. The numerical solution of these boundary value problems employing a finite element method allows to determine the *equivalent* moduli $M_c(\omega)$ and $N(\omega)$. These moduli are then employed at the macroscale in a numerical simulator based on a finite element discretization of the viscoelastic wave equation formulated in the space-frequency domain. Using this numerical upscaling procedure the number of DOF is reduced in several orders of magnitude as compared with the DOF that would be needed if Biot's equation of motion was employed at the macroscale, while still representing the acoustic behavior of the highly heterogeneous fluid-saturated porous media. The proposed methodology is first validated by comparison with previous numerical simulations performed using a finite element procedure for the approximate solution of Biot's equations of motion for the case of alternating layers of gas and water, as presented in [61]. Then, it is applied to simulate the seismic response of an heterogeneous CO₂ accumulation within the Utsira formation, at the Sleipner field, using the data in [14]. The simulation results allow to explain the high levels of attenuation observed in the seismic data surveyed in this injection field ([1, 2]), as a result of the lateral and vertical migration of the CO₂ and its distribution in the form of patches of gas within an otherwise brine saturated formation.

4.1 Methodology

Let us consider a 2D isotropic fluid-saturated porous material Ω with boundary $\partial\Omega$ containing multiscale mesoscopic heterogeneities in the fluid and/or the solid matrix properties. Let us take a part of bulk fluid-saturated material containing a representative number of such heterogeneities. This will be our representative element, denoted Ω_R , and for simplicity let us assume that Ω_R is a square of side length L_R , *i.e.* $\Omega_R = (0, L_R)^2$. In the absence of external body sources, the oscillatory motion of Ω_R at the angular frequency ω will be assumed to obey Biot's equations of motion, stated in the form

$$-\omega^2 \rho u^s(x, \omega) - \omega^2 \rho_f u^f(x, \omega) - \nabla \cdot \tau(u^s, u^f) = 0, \quad \Omega_R, \quad (37)$$

$$\begin{aligned} -\omega^2 \rho_f u^s(x, \omega) - \omega^2 \frac{S \rho_f}{\phi} u^f(x, \omega) + i\omega \frac{\eta}{\kappa} u^f(x, \omega) + \\ \nabla p_f(u^s, u^f) = 0, \quad \Omega_R, \end{aligned} \quad (38)$$

where u^s and u^f are the Fourier transforms of the displacement vectors associated with the solid and the fluid phases, respectively, x denotes the particle position and ω the angular frequency. In (37)-(38) $\tau(u^s, u^f)$ is the total stress tensor and $p_f(u^s, u^f)$ is the fluid pressure, that are defined by stress-strain relations with coefficients that can be determined in terms of the bulk moduli K_s , K_f and K_m of the solid grains, the fluid and the dry matrix, the shear modulus μ of the dry matrix and the porosity (see [61]). In (37)-(38) ρ_s and ρ_f are the mass densities of the solid grains and the saturating fluid and $\rho = (1 - \phi)\rho_s + \phi\rho_f$ is the bulk density of the material, with ϕ being the effective porosity. Also, η is the fluid viscosity, κ the absolute permeability and S the structure or tortuosity factor.

To determine the *equivalent* complex frequency dependent plane wave modulus $M_c(\omega) = \lambda_c(\omega) + 2N(\omega)$ and the complex shear modulus $N(\omega)$ associated with our domain Ω we proceed as explained in [66], using a finite element procedure to solve Biot's equations (37)-(38) in Ω_R with boundary conditions chosen to represent compressibility and shear oscillatory tests at a finite number of angular frequencies ω . The computed displacements allow to measure the volume and shape changes of the sample, from where $M_c(\omega)$ and $N(\omega)$ are obtained.

At this stage, for a finite number of frequencies we solve the following boundary value problem at the macroscale (in Ω):

$$-\omega^2 \rho_b u - \nabla \cdot \sigma(u) = 0, \quad \Omega \quad (39)$$

$$-\sigma(u)\nu = i\omega \mathcal{D}u, \quad \partial\Omega, \quad (40)$$

where $u = (u_x, u_y)$ is the displacement vector in our *equivalent* viscoelastic material, ρ_b is the average bulk density and (40) is a first-order absorbing boundary condition using the positive

definite matrix \mathcal{D} , which definition is given in [31]. The stress tensor $\sigma(u)$ is defined in the space-frequency domain by

$$\sigma_{jk}(u) = \lambda_c(\omega)\nabla \cdot u\delta_{jk} + 2N(\omega)\varepsilon_{jk}(u), \quad \Omega, \quad (41)$$

where $\varepsilon_{jk}(u)$ denotes the strain tensor and δ_{jk} is the Kronecker delta.

The approximate solution of (39) with the boundary conditions (40) was obtained using a finite element procedure employing a uniform partition \mathcal{T}^h of the computational domain Ω into square subdomains $\Omega_m, m = 1, \dots, M$ of side length h . To approximate each component of the solid displacement vector we employed the nonconforming finite element space defined in [21], since it generates less numerical dispersion than the standard bilinear elements ([76]). It can be demonstrated that the error associated with this numerical procedure measured in the energy norm is of order h ([31]).

4.2 Validation of the numerical procedure

To validate the procedure we compared the time histories of the solid particle velocities obtained using the equivalent viscoelastic model and those resulting from Biot's equations of motion. The domain Ω is a square domain of side length 800 m consisting in alternating layers of equal thickness 40 cm fully saturated with either gas or water. The solid matrix and fluids properties are ([13]): $\phi = 0.3$, $\kappa = 10^{-12} \text{ m}^2$, $S = 1$, $K_s = 37 \text{ GPa}$, $K_m = 4.8 \text{ GPa}$ and $\mu = 5.7 \text{ GPa}$, $K_w = 2.25 \text{ GPa}$, $\eta_w = 0.03 \text{ Poise}$, $K_g = 0.012 \text{ GPa}$ and $\eta_g = 0.0015 \text{ Poise}$. The medium is excited with a compressional point source with dominant frequency 20 Hz. The mesh sizes are 2000×2000 for the Biot model ([61]) and 200×200 for the viscoelastic model.

Figure 1 shows time histories of the vertical component of the velocity $v_y = i\omega u_y$ in our viscoelastic model as function of time at three receivers r_j with receiver locations $(x_{rj}, y_{rj}), j = 1, 2, 3$, where $x_{rj} = 400 \text{ m}, j = 1, 2, 3$ and $y_{r1} = 230 \text{ m}, y_{r2} = 456 \text{ m}, y_{r3} = 682 \text{ m}$. The corresponding time histories for the Biot model are almost identical and are not shown for brevity. The amplitude decay due to the mesoscopic loss mechanism can be clearly observed. To fully verify the agreement with White's theory, the quality factor $Q(\omega)$ associated with this decay rate was evaluated using the frequency-shift and spectral-ratio methods. Both methods yield Q -estimates that are in very good agreement with the theoretical value ($Q = 28$ at the dominant frequency 20 Hz) predicted by [74], [61]. Notice that using our upscaling procedure the number of DOF has decreased in two orders of magnitude to obtain almost the same response of the system, with the consequent drastic reduction in computing time.

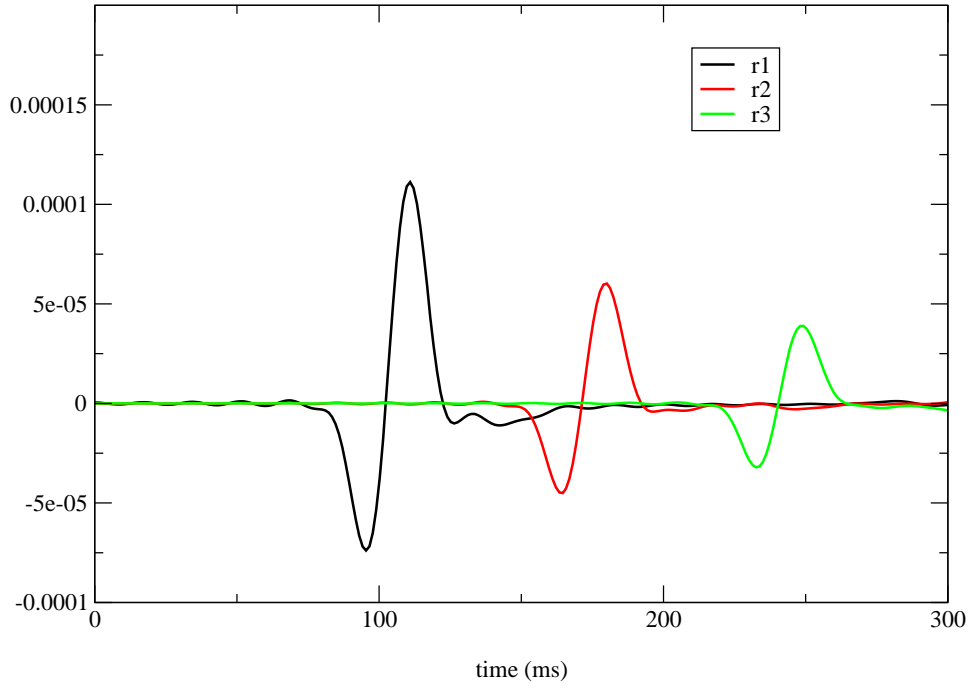


Figure 18: Time histories of the vertical component of particle the velocity at the receivers r_1, r_2 and r_3 obtained with a viscoelastic model for a periodic gas-water saturated porous medium.

4.3 Application to seismic modelling in a CO₂ injection site

As is well known, geological sequestration of carbon dioxide must be carefully monitored to ensure that this greenhouse gas is not returned to the Earth’s atmosphere. Since October 1996, million of tonnes of CO₂ are separated from natural gas and re-injected into a shallow saline aquifer, the Utsira formation at Sleipner field. This formation consists of a high porosity unconsolidated sandstone with several thin intra-reservoir shale layers, which structural geometry is not completely known. These shale intervals act as temporary seals causing accumulations of high CO₂ saturations beneath them ([1, 2]). However, as deduced from seismic interpretations and reservoir flow simulations ([1]), these shales allow for the vertical migration of CO₂, giving rise to the formation of *chimneys* at depth levels above the injection point. The marked contrast between the physical and acoustical properties of natural reservoir fluids and those of carbon dioxide allows for the utilization of seismic methods as a tool for monitoring the spatio-temporal distribution of CO₂ near the injection point. In particular, seismic data recorded in this injection site show a strong amplitude decay and delay of the seismic signals through the chimneys ([1]).

With these motivations, we employ our equivalent viscoelastic model to simulate the seismic response of wave propagation using the parameters of the Utsira formation. Thus we design an

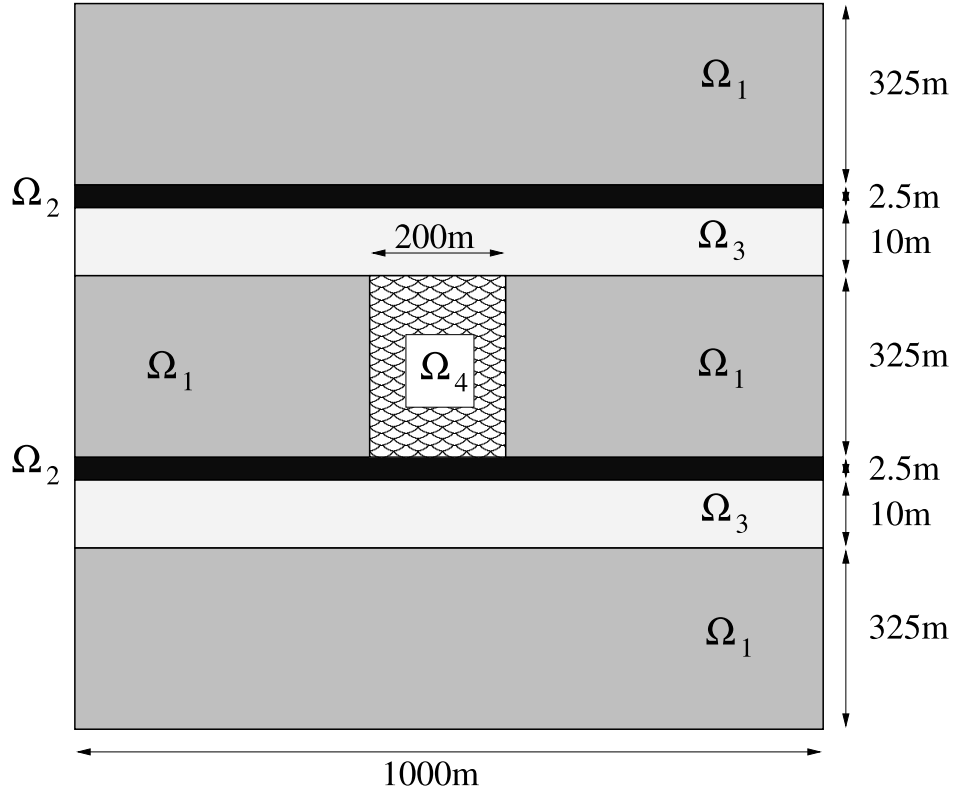


Figure 19: The idealized subsurface model of CO₂ accumulation.

idealized domain $\Omega = (0, L)^2$ with $L = 1$ Km consisting of different regions $\Omega_i, i = 1, 2, 3, 4$ as shown in Figure 2.

The material properties of the regions Ω_i are given in Table 4, taken from [14]. The thin layers of shale, referred to as Ω_2 , are used to model the CO₂ accumulations at different depths. We assume that the major cause of the observed attenuation in the seismic sections is associated to the accumulation of the CO₂ in the region Ω_4 of our idealized model. According to the previous description, we assume that the pore space in region Ω_4 contains a 90% of brine and a 10 % of CO₂ in the form of patches with a fractal-type spatial distribution, a novel saturation model, not considered previously by the authors in this field. Region Ω_3 is also assumed to contain patches of CO₂, but with 60% CO₂ saturation and 40% brine saturation. The regions Ω_1 and Ω_2 are considered to be brine-filled and are modeled defining a viscoelastic material having the same phase velocities and quality factors than the original Biot's mediums. The generation of the viscoelastic moduli associated with the patchy saturated regions Ω_3 and Ω_4 was achieved using stochastic fractal fields based on the so-called von Karman self-similar correlation functions. Following [26] and more recently [65], we consider a particular case for

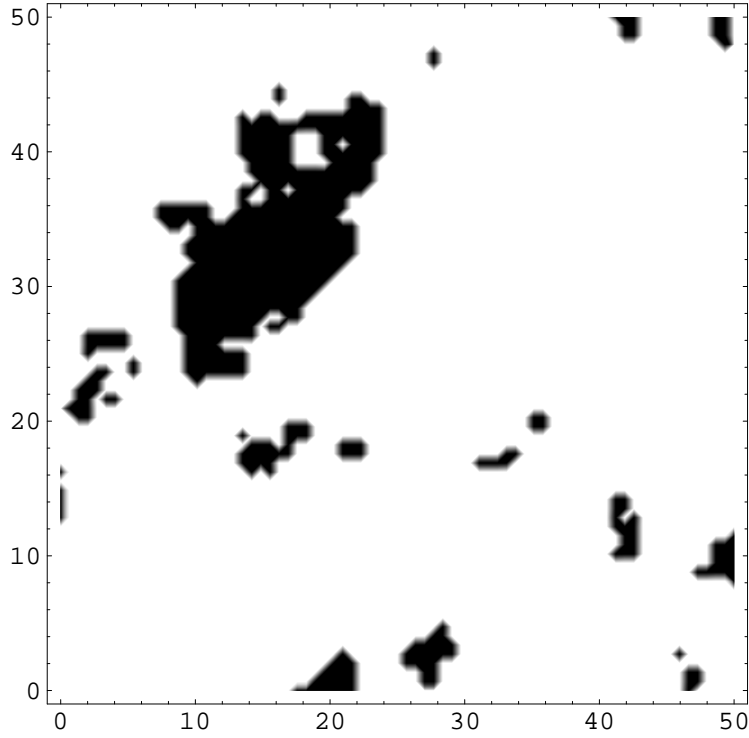


Figure 20: The reference sample Ω_R associated with the patchy CO_2 saturated region Ω_4 .

which the spectral density of the stochastic field is given by:

$$S_d(k_x, k_y) = S_0(1 + k^2 a^2)^{-(H+E/2)} \quad (42)$$

where $k = \sqrt{k_x^2 + k_y^2}$ is the radial wavenumber, a the correlation length, H is a self-similarity coefficient ($0 < H < 1$) and S_0 is a normalization constant. Equation (42) corresponds to a fractal process of fractal dimension $D = E + 1 - H$ at scales smaller than a .

Figure 3 displays the representative sample Ω_R of the region Ω_4 , taken to be a square of side length 50 cm with 10% CO_2 saturation. The parameters associated with Ω_R in Figure 3 are $D = 2.2$, $a = 5$ cm, $E = 2$.

Region	$\rho_s(\text{gr}/\text{cm}^3)$	$K_s(\text{GPa})$	ϕ	$K_m(\text{GPa})$	$\mu(\text{GPa})$	S	$\kappa(\text{cm}^2)$
Ω_1	2.6	40	0.35	1.33	0.85	2.8	$1.6 \cdot 10^{-8}$
Ω_2	2.6	20	0.25	4.7	0.99	5	$0.001 \cdot 10^{-8}$
Ω_3	2.6	40	0.36	1.4	0.87	2.8	$1.6 \cdot 10^{-8}$
Ω_4	2.6	40	0.36	1.4	0.87	2.8	$1.6 \cdot 10^{-8}$

Table 4. Material properties of the Utsira formation

The brine properties are $\rho_w = 1.03 \text{ gr/cm}^3$, $K_w = 2.61 \text{ GPa}$ and $\eta_w = 1.2^{-2} \text{ Poise}$, while the gas properties are $\rho_g = 0.485 \text{ gr/cm}^3$, $K_g = 0.012 \text{ GPa}$ and $\eta_g = 0.0015 \text{ Poise}$. For regions Ω_3 and Ω_4 we performed the described compressibility test in order to determine the complex equivalent modulus $M_c(\omega)$ for each region.

Also, for each reference sample Ω_R associated with either Ω_3 or Ω_4 we computed the average bulk density ρ_b needed in (39). The shear modulus in Ω_3 and Ω_4 were taken to be real as in Table 4. As result of the compressibility tests in Ω_4 we obtained a decreasing set of values of the P-quality factor Q_p in the range $(0, 100\text{Hz})$, with values of $Q_p=10$ at 15 Hz and $Q_p=5$ at 100 Hz. The P-phase velocities vary between 1.22 km/s at 1 Hz and 1.4 km/s at 100 Hz. Thus, we expect that P-waves will suffer strong attenuation when travelling across Ω_4 . On the other hand, in Ω_3 the compressibility tests yield values of the phase velocity almost independent of frequency and equal to 1.17 km/s in the range $(0, 100)$ Hz, and the values of the P-quality factor Q_p are $Q_p = 100$ at 50 Hz and $Q_p = 50$ at 100 Hz, so that waves would suffer very little attenuation when travelling across this region. To excite the medium Ω in our numerical simulations of seismic monitoring of CO_2 injection we used a horizontal line source of dominant frequency 25 Hz located at depth $y = 100 \text{ m}$ to obtain a plane wave travelling downwards across the formation.

Figure 4 displays a snapshot of the vertical particle displacement at time $t=225 \text{ ms}$. It can be seen a very clear reflection which, due to fact that the wavelengths of the direct wave are much greater than the thickness of the upper CO_2 -bearing layer, it is associated with the interference of the reflections at the top and the bottom of such layer. Also, we can observe a significant delay and amplitude decay of the direct wave while travelling across the chimney (zone Ω_4).

The next snapshot (Figure 5) corresponds to a time $t=350 \text{ ms}$. It shows the very strong attenuation and velocity dispersion produced by the chimney on the direct wave. Also, it can be seen the generation of a reflection produced by the the lower CO_2 -bearing layer at both sides of the chimney.

Figure 6 shows a plot of the recorded traces near the surface. The first reflection at about 250 ms is generated by the presence of the upper CO_2 -bearing layer, while the second reflection, at approximately 600 ms, is produced at the second CO_2 accumulation. A weak multiple reflection is also observed. The center of the second reflector is strongly attenuated due to the two-way travel across the chimney.

In our last numerical experiment we consider a smaller correlation length $a = 1 \text{ cm}$ in the definition (42) of the fractal spectral density distribution to generate the complex moduli associated with region Ω_4 , but keeping the overall CO_2 saturation to be 10%. This change in the correlation length causes changes in the size and shape of the patches, which in turn modifies

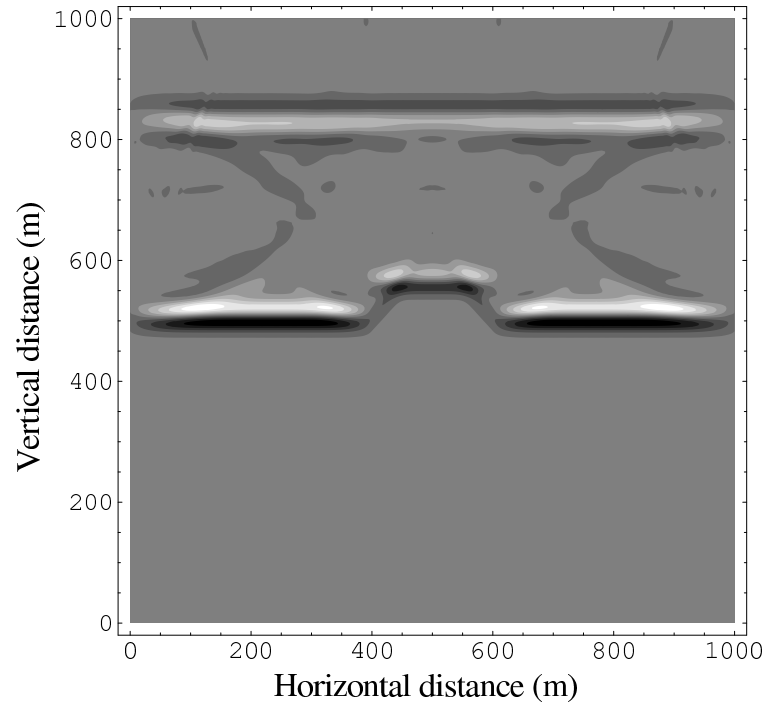


Figure 21: Snapshot at $t=225$ ms for the case of a plane wave source.

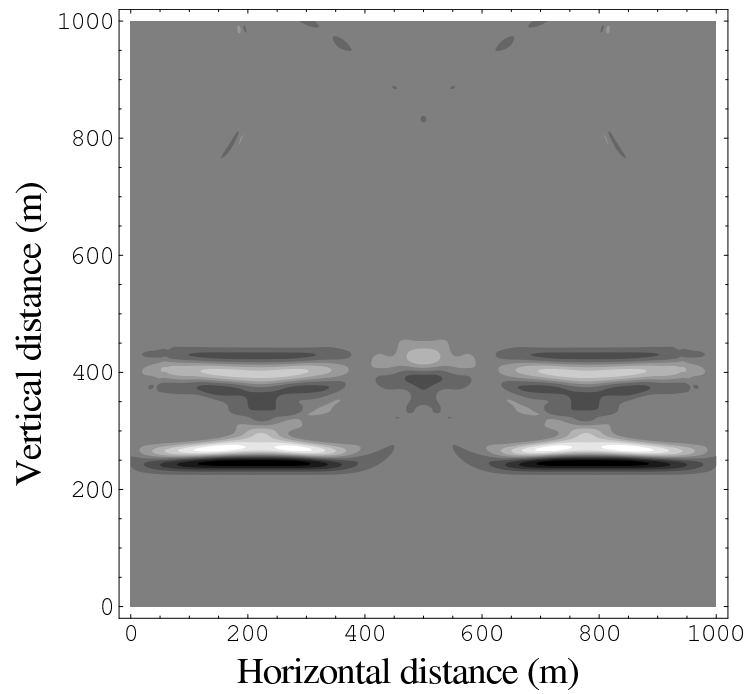


Figure 22: Snapshot at $t=350$ ms for the case of a plane wave source.

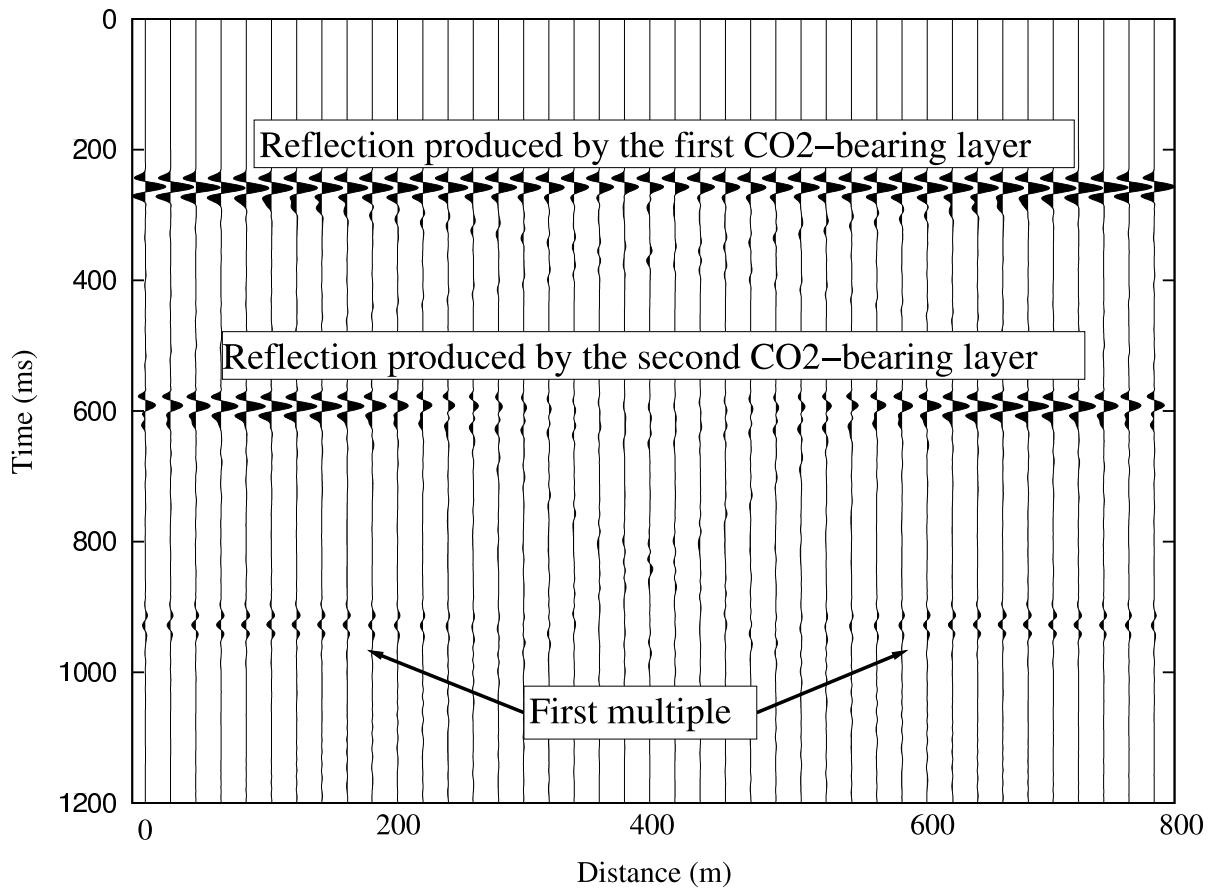


Figure 23: Time histories measured near the surface for the case of a plane wave source. Region Ω_4 has correlation length $a=5$ cm.

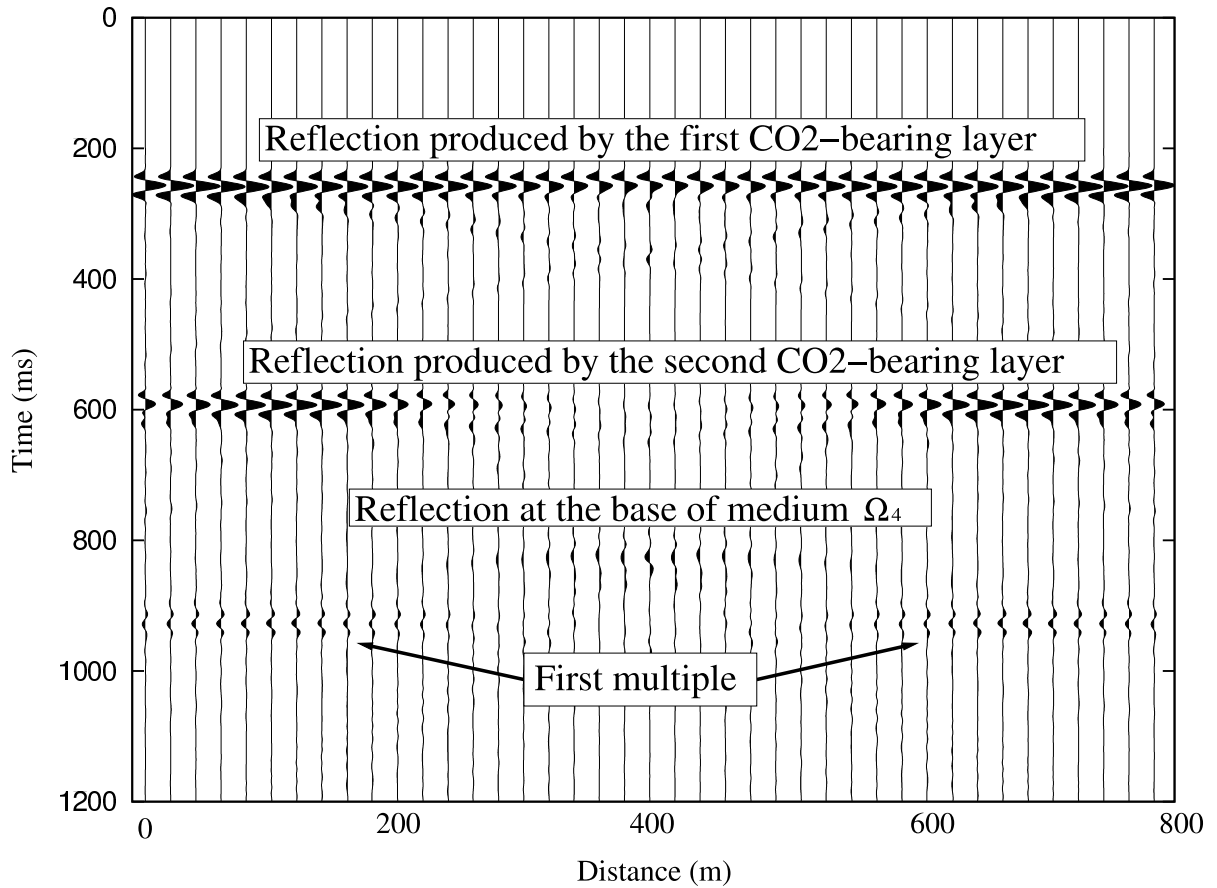


Figure 24: Time histories measured near the surface for the case of a plane wave source. Region Ω_4 has correlation length $a=1$ cm.

the attenuation properties of Ω_4 . This can be noticed in Figure 7, where the weak delayed reflection at approximately 850 ms corresponds to waves reflected at the second CO_2 -bearing layer. This reflection can not be observed in Figure 6 due to the stronger attenuation effects suffered by the waves. This difference in the seismic response is only due to the change of the sizes and shapes of the patches of CO_2 , demonstrating that the mesoscopic-scale heterogeneities can affect the seismic response at the macroscale.

4.4 Conclusions

We have presented a novel finite element procedure to model wave propagation and mesoscopic attenuation effects in highly heterogeneous fluid-saturated poroelastic media. The method uses a numerical upscaling procedure to define a viscoelastic model stated in the space-frequency domain with complex coefficients bringing to the macroscale the attenuation effects due to the

mesoscopic-scale heterogeneities. The method was first validated by comparison with previous numerical experiments employing Biot's equations of motion at the macroscale, showing that the proposed methodology allows for a reduction in several orders of magnitude of the degrees of freedom needed to represent the response of a given highly heterogeneous fluid-saturated poroelastic medium. The algorithm was then applied to simulate the seismic response of a CO₂ injection site in the Utsira formation. The numerical results obtained using fractal patchy saturation, give a possible explanation for the high levels of attenuation observed. The experiments also demonstrated that the size and shape of the CO₂ patches in a brine-filled formation can change the seismic response of the formation being monitored. The presented modelling procedure can be a useful tool in seismic monitoring, for the interpretation of time lapse seismic, for the delineation of CO₂ plumes and the characterization of its saturation type.

These results were presented in the following work:

J. E. Santos, J. G. Rubino and C. L. Ravazzoli Modelling mesoscopic attenuation in a highly heterogeneous Biot's medium employing an effective viscoelastic model. Expanded Abstracts, Society of Exploration Geophysicists, International Exposition and 78th. Annual Meeting, Las Vegas, 2008. ISSN 1052-3812.

5 A finite element method to model attenuation and dispersion effects in highly heterogeneous fluid-saturated porous media

A major cause of P-wave attenuation at seismic frequencies is known as mesoscopic loss and it is caused by heterogeneities greater than the pore size but much smaller than the predominant wavelengths. A fast P-wave travelling in an heterogeneous fluid-saturated porous material induces fluid-pressure gradients in the different regions of the medium. This in turn generates slow P-waves that diffuse away from the interfaces separating the heterogeneities, causing energy loss and velocity dispersion. White and coauthors [74, 75] were the first to model wave-induced fluid flow produced by mesoscopic-scale heterogeneities in partially saturated rocks, showing that this mechanism can produce important attenuation and velocity dispersion effects at seismic frequencies. They obtained approximated solutions of the response of plane porous layers alternately saturated with gas and water [74] and of spherical gas pockets in a water-saturated porous rock [75]. In this fashion, the equivalence between the approximate behavior of low-frequency fast compressional P-waves in the presence of mesoscale heterogeneities and that of a viscoelastic solid at the macroscale was established. Since those leading work, the study of this attenuation mechanism has motivated the interest and research of many authors in this field, such as [23, 56, 30, 13, 42, 61], among others. These mesoscopic scale heterogeneities in the solid frame and fluid properties, typically on the order of centimeters, are much smaller than the wavelengths of the fast P and S waves travelling in Biot's media. Consequently, the huge number of degrees of freedom (DOF) needed to represent these heterogeneities and their attenuation effects at the macroscale in any finite element or finite difference based numerical procedure employing Biot's equations renders such approach not feasible. In this paper we present an alternative approach to overcome this difficulty. First we employ the numerical upscaling procedure presented in [67] as follows. We define local boundary value problems representing time-harmonic compressibility and shear tests applied to a representative sample Ω_R of bulk material containing stochastic heterogeneities described by their statistical properties. The computed volume and shape changes of Ω_R allowed us to calculate complex P-wave and shear moduli. Averaging over realizations of the stochastic parameters, we obtain average P-wave and shear modul, denoted $\overline{M}_c(\omega)$ and $\overline{\mu}(\omega)$, respectively, defining locally an *average equivalent* viscoelastic solid having approximately the same attenuation and velocity dispersion than the original fluid-saturated porous rock. Biot's theory [9] is used to model the response of the heterogeneous material to the applied stresses. For each realization of the stochastic parameters, the *equivalent* complex P-wave moduli and shear moduli are obtained solving numerically

Biot's equations of motion in the space-frequency domain with appropriate boundary conditions employing a finite element procedure and for a finite number of frequencies in the range where the material is going to be tested by acoustic methods. Second, the computed *average equivalent* complex P-wave and shear moduli $\overline{M}_c(\omega)$ and $\overline{\mu}(\omega)$ are employed at the macroscale to define a viscoelastic medium that will represent our heterogeneous Biot's medium. This viscoelastic medium is determined using a causal model that fit the computed frequency dependent average moduli. Numerical simulations of wave propagation at the macroscale are performed in the time-domain. The algorithm, based on the velocity-stress elastodynamic equations, uses a spectral method with a Chebychev expansion in the vertical direction, and absorbing boundary conditions at the artificial boundaries. This approach allows the calculation of the spatial derivatives with high accuracy [12]. The anelasticity is described by the standard linear solid, also called the Zener model. The proposed methodology is applied to the CO₂ geological storage monitoring. There is evidence that, during the last 150 years, the increased concentration of greenhouse gases has increased the atmospheric temperature by 0.3 - 0.6 C. Geological sequestration of CO₂ is an immediate option to reduce the emission of this gas into the atmosphere. The main possibilities are injection into hydrocarbon reservoirs, saline aquifers and unmineable coal mines. Wherever we put the CO₂, however, it is necessary to do before, during and after the injection integrated studies to model the long term behaviour of CO₂. In particular, in this study we are interested in the identification of potentially hazardous leakages using the seismic method. In this work we consider one of the site of the CASTOR project, the almost depleted Atzbach-Schwanenstadt gas-field in central northern Austria, where the CO₂ comes from a papermill and a fertilizer plant. This site is considered a potential site for a future CO₂ injection. It is important to monitor the time evolution of the injected CO₂ within the reservoir and in the sealing layers above, so to evidence changes and possible breakthrough before it reaches the surface. The seismic survey method is very useful to this aim, because of the mesoscopic loss effect, which occurs when the pore space is occupied either by liquids and gases. In this application we evaluate whether in this particular case the seismic method is efficient.

5.1 Proposed methodology

We consider a 2D isotropic fluid-saturated porous material Ω with boundary $\partial\Omega$ composed of several subdomains, say $\Omega = \cup_{m=1}^{m=M} \Omega_m$. We assume also that some of the Ω_m 's contain multiscale mesoscopic heterogeneities in the solid and fluid properties, which are statistically homogeneous and can be described by its statistical properties. Thus, for each subdomain Ω_m let us take a part of bulk fluid-saturated material containing a representative number of such heterogeneities. This will be our representative element, denoted $\Omega_{R,m}$, and for simplicity let

us assume that $\Omega_{R,m}$ is a square of side length $L_{R,m}$, *i.e.* $\Omega_{R,m} = (0, L_{R,m})^2$. In the absence of external body sources, the oscillatory motion of $\Omega_{R,m}$ at the angular frequency ω will be assumed to obey Biot's equations of motion, stated in the form

$$-\omega^2 \rho^m u^{s,m}(\tilde{x}, \omega) - \omega^2 \rho_f^m u^{f,m}(\tilde{x}, \omega) - \nabla \cdot \tau(u^{s,m}, u^{f,m}) = 0, \quad \tilde{x} \in \Omega_{R,m}, \quad (43)$$

$$\begin{aligned} -\omega^2 \rho_f^m u^{s,m}(\tilde{x}, \omega) - \omega^2 \frac{S^m \rho_f^m}{\phi^m} u^{f,m}(\tilde{x}, \omega) + i\omega \frac{\eta^m}{\kappa^m} u^{f,m}(\tilde{x}, \omega) \\ + \nabla p_f(u^{s,m}, u^{f,m}) = 0, \quad \tilde{x} \in \Omega_{R,m}. \end{aligned} \quad (44)$$

Here we denote by \tilde{x} the local coordinate system at the mesoscale in $\Omega_{R,m}$. Also, $u^{s,m}$ and $u^{f,m}$ are the Fourier transforms of the solid and fluid relative to the solid displacement vectors, respectively. In (43)-(44) ρ_s and ρ_f are the mass densities of the solid grains and the saturating fluid and $\rho^m = (1 - \phi^m)\rho_s^m + \phi^m\rho_f^m$ is the bulk density of the material, with ϕ^m being the effective porosity. Also, η^m is the fluid viscosity, κ^m the absolute permeability and S^m the structure or tortuosity factor. Also, $\tau(u^{s,m}, u^{f,m})$ is the total stress tensor and $p_f(u^{s,m}, u^{f,m})$ is the fluid pressure, given by stress-strain relations

$$\tau_{jk}(u^s, u^f) = 2\mu^m \varepsilon_{jk}(u^{s,m}) + \delta_{jk}(\lambda_c^m \nabla \cdot u^{s,m} + \alpha K_{av}^m \nabla \cdot u^{f,m}), \quad (45)$$

$$p_f(u^{s,m}, u^{f,m}) = -\alpha^m K_{av}^m \nabla \cdot u^s - K_{av}^m \nabla \cdot u^{f,m}, \quad (46)$$

where $\varepsilon_{jk}(u^{s,m})$ denotes the strain tensor and δ_{jk} is the Kronecker delta. Also, the coefficient μ^m is equal to the shear modulus of the bulk material, considered to be equal to the shear modulus of the dry matrix and

$$\lambda_c^m = K_c^m - \mu^m,$$

with K_c^m being the bulk modulus of the saturated material. The coefficients in (45)-(46) can be obtained from the relations

$$\alpha^m = 1 - \frac{K_d^m}{K_s^m}, \quad K_{av}^m = \left(\frac{\alpha^m - \phi^m}{K_s^m} + \frac{\phi}{K_f^m} \right)^{-1}, \quad K_c^m = K_d^m + (\alpha^m)^2 K_{av}^m, \quad (47)$$

where K_s^m , K_d^m and K_f^m denote the bulk modulus of the solid grains composing the solid matrix, the dry matrix and the saturant fluid, respectively. The viscoelastic model to be used at the macroscale to perform our numerical simulations will be defined in terms of the macroscopic bulk density $\bar{\rho}_b^m(x)$ and the (undrained) macroscopic frequency dependent shear and P-wave modulus $\bar{\mu}_c^m(x, \omega)$ and $\bar{M}_c^m(x, \omega)$, with x denoting the coordinate system at the macroscale. The coefficient $\bar{\rho}_b^m(x)$ is determined by averaging the local bulk density $\rho^m(\tilde{x})$ over $\Omega_{R,m}$. The *average equivalent* complex frequency dependent plane wave modulus $\bar{M}_c^m(x, \omega) = \bar{\lambda}_c^m(x, \omega) + 2\bar{\mu}_c^m(x, \omega)$ and the *average equivalent* complex shear modulus $\bar{\mu}^m(x, \omega)$ are determined in a Montecarlo

fashion as in [67]. Here we briefly summarize the procedure. Biot's equations (43)-(44) were solved over a set of realizations of representative samples $\Omega_{R,m}$ containing stochastic heterogeneities characterized by their statistical properties, with boundary conditions representing compressibility and shear oscillatory tests at a finite number of angular frequencies ω . The size of the rock sample $\Omega_{R,m}$ is not arbitrary: it has to be big enough to constitute a representative volume of the medium but, at the same time, it has to be much smaller than the wavelengths associated with each excitation frequency. To find an upper bound for the side length $L_{R,m}$, we check that the compressibility and shear tests applied to homogeneous samples of side length $L_{R,m}$, composed of any of the different solid and fluid parts forming the heterogeneous medium, give negligible attenuation and velocity dispersion at the highest frequency under consideration. To obtain the *equivalent* complex plane wave modulus $M_c^m(x, \omega)$ associated with each realization of the reference sample $\Omega_{R,m}$, $\Omega_{R,m}$ is subjected to a time-harmonic compression of the form $\Delta P e^{i\omega t}$ on its top boundary, and no tangential forces are applied on the boundaries of the sample. Also, the solid is neither allowed to move on the bottom boundary nor have horizontal displacements on the lateral boundaries, and the fluid is not allowed to flow into or out of the sample. Thus we solved equation (43)-(44) with the following boundary conditions:

$$\begin{aligned}
\tau(u^{s,m}, u^{f,m})\nu &= (0, -\Delta P), \quad \text{on } \Gamma^T, \\
\tau(u^{s,m}, u^{f,m})\nu \cdot \chi &= 0, \quad \text{on } \Gamma^L \cup \Gamma^R, \\
u^{s,m} \cdot \nu &= 0, \quad \text{on } \Gamma^L \cup \Gamma^R, \\
u^{s,m} &= 0, \quad \text{on } \Gamma^B, \\
u^{f,m} \cdot \nu &= 0, \quad \text{on } \Gamma^L \cup \Gamma^R \cup \Gamma^B \cup \Gamma^T,
\end{aligned} \tag{48}$$

where Γ^L , Γ^R , Γ^B and Γ^T are the left, right, bottom and top boundaries of $\Omega_{R,m}$, respectively. In the expressions 48 ν is the unit outer normal and χ is a unit tangent oriented counterclockwise on the boundaries of $\Omega_{R,m}$ such that $\{\nu, \chi\}$ is an orthonormal system on Γ . The computed displacements allow to measure the volume change of the sample, from where $M_c(x, \omega)$ is determined [67]. Similarly, to obtain the *equivalent* complex shear modulus $\mu^m(x, \omega)$ associated with each realization of the reference sample $\Omega_{R,m}$, the solid is not allowed to move on the bottom boundary of the sample, the fluid is not allowed to flow into or out of the rock and shear stresses are applied on the left, right and top boundaries. Then in this case we solve (43)-(44) with boundary conditions

$$\begin{aligned}
\tau(u^{s,m}, u^{f,m})\nu &= g, \quad \text{on } \Gamma^T \cup \Gamma^L \cup \Gamma^R, \\
u^{s,m} &= 0, \quad \text{on } \Gamma^B, \\
u^{f,m} \cdot \nu &= 0, \quad \text{on } \Gamma,
\end{aligned} \tag{49}$$

where

$$g = \begin{cases} (0, -\Delta T), & \text{on } \Gamma^L, \\ (0, \Delta T), & \text{on } \Gamma^R, \\ (\Delta T, 0), & \text{on } \Gamma^T, \end{cases} \quad (50)$$

and ΔT denotes the constant amplitude of the external oscillatory stress. The computed change in shape of the rock sample permits to determine the *equivalent* complex shear modulus $\bar{\mu}_c^m(x, \omega)$.

To solve (43)-(44) with either (48) or (49) as boundary conditions we used a finite element procedure employing bilinear functions to approximate the solid displacement vector, while for the fluid displacement a closed subspace of the vector part of the Raviart-Thomas-Nedelec space of zero order was employed ([60, 48]). Concerning the mesh size used in this local problems, it has to be small enough so that the diffusion process associated with the fluid pressure equilibration is accurately resolved. For practical purposes, in this work we take the mesh size so that the minimum diffusion length is discretized with at least 3 mesh points at the highest frequency, which is sufficient to represent a (smooth) diffusion-type process. See [67] for details on the finite element spaces and mesh sizes employed to solve each oscillatory local problem.

The average and variance of the phase velocities and quality factors associated with these moduli were obtained by averaging over realizations of the stochastic parameters, and the Monte Carlo realizations were stopped when the variance of the computed quantities stabilized at an almost constant value. The mean phase velocities and mean inverse quality factors obtained in this fashion at a finite number of frequencies are the desired *average equivalent* plane wave and shear modulus. As a final step, the computed complex frequency dependent moduli were fitted with a suitable viscoelastic model to be employed at the macroscale in the numerical simulations.

5.2 Memory variables and equation of motion

After computing the *average equivalent* complex plane wave and shear moduli, we perform numerical simulations of wave propagation at the macroscale solving the single-phase viscoelastic differential equations. The memory-variable approach introduced in [12] is essential to avoid numerical calculations of time convolutions when modeling wave propagation in the time domain. With this approach, we obtain a complete differential formulation. The dilatational and

shear relaxation functions in the stress-strain relation for isotropic media have the form:

$$\psi_{\mathcal{K}}(t) = \mathcal{K}_{\infty} \left[1 - \frac{1}{L_1} \sum_{l=1}^{L_1} \left(1 - \frac{\tau_{el}^{(1)}}{\tau_{\sigma l}^{(1)}} \right) \exp(-t/\tau_{\sigma l}^{(1)}) \right] H(t), \quad (51)$$

$$\psi_{\mu}(t) = \mu_{\infty} \left[1 - \frac{1}{L_2} \sum_{l=1}^{L_2} \left(1 - \frac{\tau_{el}^{(2)}}{\tau_{\sigma l}^{(2)}} \right) \exp(-t/\tau_{\sigma l}^{(2)}) \right] H(t), \quad (52)$$

where H is the Heaviside function and $\tau_{el}^{(\nu)}$, $\tau_{\sigma l}^{(\nu)}$ are relaxation times corresponding to dilatational ($\nu = 1$) and shear ($\nu = 2$) attenuation mechanisms. They satisfy $\tau_{el}^{(\nu)} \geq \tau_{\sigma l}^{(\nu)}$, with the equal sign corresponding to the elastic case.

The stress-strain relations read

$$\sigma_{ij} = \psi_{\mathcal{K}} * \epsilon_{kk} \delta_{ij} + 2\psi_{\mu} * d_{ij}, \quad (53)$$

where $*$ denotes the time convolution. After introduction of the memory variables, we have

$$\sigma_{ij} = \mathcal{K}_U \left(\epsilon_{kk} + \sum_{l=1}^{L_1} e_l^{(1)} \right) \delta_{ij} + 2\mu_U \left(d_{ij} + \sum_{l=1}^{L_2} e_{ijl}^{(2)} \right), \quad (54)$$

where

$$\mathcal{K}_U = \frac{\mathcal{K}_{\infty}}{L_1} \sum_{l=1}^{L_1} \frac{\tau_{el}^{(1)}}{\tau_{\sigma l}^{(1)}}, \quad \mu_U = \frac{\mu_{\infty}}{L_2} \sum_{l=1}^{L_2} \frac{\tau_{el}^{(2)}}{\tau_{\sigma l}^{(2)}}, \quad (55)$$

and

$$e_l^{(1)} = \varphi_{1l} * \epsilon_{kk}, \quad l = 1, \dots, L_1 \quad (56)$$

and

$$e_{ijl}^{(2)} = \varphi_{2l} * d_{ij}, \quad l = 1, \dots, L_2 \quad (57)$$

are sets of memory variables for dilatation and shear mechanisms, with

$$\varphi_{\nu l} = \frac{1}{\tau_{\sigma l}^{(\nu)}} \left(\sum_{l=1}^{L_{\nu}} \frac{\tau_{el}^{(\nu)}}{\tau_{\sigma l}^{(\nu)}} \right)^{-1} \left(1 - \frac{\tau_{el}^{(\nu)}}{\tau_{\sigma l}^{(\nu)}} \right) \exp(-t/\tau_{\sigma l}^{(\nu)}) H(t). \quad (58)$$

The memory variables satisfy

$$e_l^{(1)} = \varphi_{1l}(0) \epsilon_{kk} - \frac{e_l^{(1)}}{\tau_{\sigma l}^{(1)}}, \quad e_{ijl}^{(2)} = \varphi_{2l}(0) d_{ij} - \frac{e_{ijl}^{(2)}}{\tau_{\sigma l}^{(2)}}. \quad (59)$$

For $n = 2$ and say, the (x, z) -plane, we have three independent sets of memory variables. In fact, since $d_{11} = -d_{33} = (\epsilon_{11} - \epsilon_{33})/2$, then $e_{11l}^{(2)} = \varphi_{2l} * d_{11} = -\varphi_{2l} * d_{33}$. The other two sets are $e_l^{(1)} = \varphi_{1l} * \epsilon_{kk}$ and $e_{13l}^{(2)} = \varphi_{2l} * \epsilon_{13}$.

The equation of motion is obtained by substituting the stress-strain relation (54) into Euler’s differential equations

$$\begin{aligned}\partial_{tt}^2 u_1 &= \rho^{-1} (\partial_1 \sigma_{11} + \partial_3 \sigma_{13} + f_1) \\ \partial_{tt}^2 u_3 &= \rho^{-1} (\partial_1 \sigma_{13} + \partial_3 \sigma_{33} + f_3),\end{aligned}\tag{60}$$

and making use of the strain-displacement relations

$$\epsilon_{ij} = \frac{1}{2} (\partial_i u_j + \partial_j u_i),\tag{61}$$

where f denotes the body force.

5.3 Application to seismic modelling in the Atzbach-Schwanenstadt injection site

The Atzbach-Schwanenstadt gas field is situated in the Molasse Basin (Alps foreland), outside the area affected by compressional deformation. Molasse basin filling started from the latest Eocene to the early Oligocene. The Atzbach gas-field is being considered as a potential site for CO₂ injection.

5.4 Atzbach-Schwanenstadt geological model

The geological model has been built on the basis of seismic interpretation, geological knowledge, and well log data [57], including the topographic surface and one low velocity layer to simulate the overburden (Figure 25a).

The model was then populated with the physical properties provided in part by the partners and in part from the existing literature. The sedimentary sequence evidences the presence of shaly sandstones with variable clay content from 30% and 50%. The reservoir is located in the A4 formation. The presence of clay, calcite and quartz modifies the effective bulk modulus of the grains. That is, the grains are formed by a mixture of 3 solids. We assume that the grain bulk modulus K_s and shear modulus μ_s are equal to the arithmetic average of the upper and lower Hashin-Shtrikman bounds [33], as described in detail in [14]. The density is simply the arithmetic average of the densities of the single constituents weighted by the corresponding volume fractions. It is assumed that CO₂ is injected in the A4 formation (Figure 2), and the presence of 3 leakages, caused by degradation of the casing of an old well. In the reservoir, the fluid (CO₂, CH₄ or fluid mix) saturation is 56%. Numerical simulations [50] show that the mixed zone (where CO₂ and CH₄ are mixed together in equal proportions) after eight years is

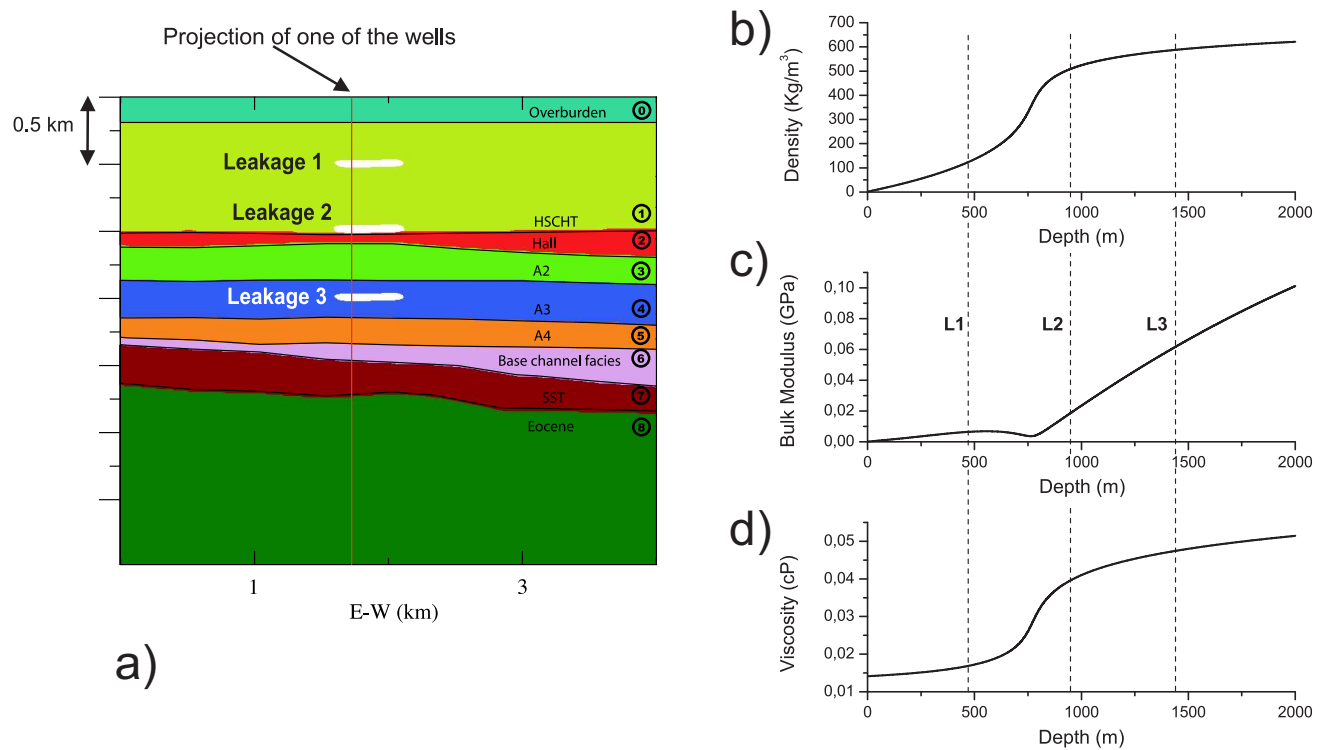


Figure 25: Atzbach-Schwanenstadt geological model (a). Density (b), bulk modulus (c) and viscosity (d) of a fluid mixture composed by CO₂ (90%) and CH₄ (10%) versus depth. L1, L2 and L3 indicate the three leakages.

approximately 15 m thick, where mixing is due to molecular diffusion. Therefore, because of the density difference between the two fluids, we assume the presence of almost pure CO₂ (90% CO₂ + 10% CH₄) at the bottom of the reservoir, almost pure CH₄ (10% CO₂ + 90% CH₄) at the top, and a 15 m thick fluid mixture zone of CO₂ (50%) and CH₄ (50%) in the middle. We also assume that the leakages are composed by almost pure CO₂ (90% CO₂ + 10% CH₄), with a fluid mixture saturation of 10%. Leakage 1 (L1) is located at 480m depth, with the CO₂ in the gaseous state. Leakage 2 (L2) is located at 950m depth, with the CO₂ in the liquid state. Leakage 3 (L3) is located at 1440m depth, with the CO₂ in the supercritical state. The reservoir (R) is located at 1788m depth, with the CO₂ in the supercritical state.

5.5 Seismic properties of pore fluids and rocks

To correctly model the seismic response, it is necessary to calculate the physical properties of the different fluids that may be present (brine and a mixture of methane and carbon dioxide). The properties of the fluids depend on temperature T and pressure p , which in turn depend

on depth z [14]. The most common method used to compute the density ρ_g of gases is the use of equations of state (EoS). We consider the Peng-Robinson EoS [52], a cubic equation derived from the van der Waals equation. The bulk modulus of the gas K_g is given by [45]

$$K_g = \gamma \rho_g \frac{\partial p}{\partial \rho_g}. \quad (62)$$

where γ the specific heat ratio. [6] provide an empirical equation of γ for methane. From a regression of the experimental data of [73], we obtain a similar empirical equation for the specific heat ratio γ of CO₂

$$\gamma = 1.03 + \frac{8.47}{p_r + 6} + \frac{11.7}{(p_r + 1.3)^2} - 29.17 \exp[-1.25(p_r + 1)], \quad (63)$$

where $p_r = p/p_c$ and $T_r = T_a/T_c$ are, respectively, the reduced pressure and temperature. $T_a = T(^{\circ}\text{C})+273.15$ is the absolute temperature, and p_c and T_c are, respectively, the critical pressure and temperature. For CO₂, $p_c = 7.38$ MPa and $T_c = 304.3$ K. The gas density at the critical conditions, or critical density, is $\rho_c = 468.2$ kg/m³. We assume for the specific heat ratio of the mixture the same mixing rule used for the parameters of the Peng-Robinson equation [19]

$$\gamma = \gamma_1 x_1^2 + \gamma_2 x_2^2 + 2x_1 x_2 (\gamma_1 + \gamma_2), \quad (64)$$

where x_1 and x_2 are the molar fraction of the two pure gases. The viscosity of the gas mix, as a function of pressure and temperature, is determined using the Lohrenz-Bray-Clark (LBC) theory [38]. Figure 3 shows density (a), bulk modulus (b) and viscosity (c) versus depth of a fluid mixture composed by CO₂ (90%) and CH₄ (10%). The brine acoustic properties depend on temperature, pressure and salinity. [6] provide a series of useful empirical relations for density, velocity and viscosity. Using these relationships, we get the brine bulk modulus. Part of the gas can dissolve in brine, generating live brine, and the rest remain as free gas. The mixture of free gas with live brine behaves as a composite fluid with properties depending on the stiffness moduli of the constituents and their respective saturations[14].

The low-frequency bulk modulus of the wet rock is given by the Gassmann modulus. [15] obtained the generalized Gassmann modulus K_G and the dry-rock bulk modulus K_m for a multi-phase system consisting of n solids and a saturating fluid. The shear modulus of the wet rock is simply the modulus of the dry rock, $\mu = \mu_m$. The P-wave and S-wave velocities (at low frequencies) are then

$$V_P = \sqrt{\frac{K_G + 4\mu/3}{\rho}} \quad \text{and} \quad V_S = \sqrt{\frac{\mu}{\rho}}, \quad (65)$$

where ρ is the bulk density.

5.6 P-wave velocity and quality factor

As described in detail in the Section 2, we determine equivalent complex P-wave and shear moduli solving at the mesoscale (and for a finite number of frequencies) boundary value problems representing oscillatory compressibility and shear tests on a representative volume of bulk material containing multiscale stochastic heterogeneities. However, the exact spatial distribution of these heterogeneities is in general unknown. Instead, they can be assumed to be stochastic functions characterized by their statistical properties. To generate the quasi-fractal patchy saturated regions for the leakages and the reservoir, we use a stochastic fractal field based on the so-called von Karman self-similar correlation functions. Following [65], we consider a particular case for which the spectral density of the stochastic field is given by

$$S_d(k_x, k_y) = S_0(1 + k^2 a^2)^{(H+E/2)}, \quad (66)$$

where $k = \sqrt{k_x^2 + k_y^2}$ is the radial wavenumber, a the correlation length, H is a self-similarity coefficient ($0 < H < 1$), E is the Euclidean dimension and S_0 is a normalization constant. Equation (66) corresponds to a fractal process of dimension $D = E + H - 1$ at scales smaller than a . For a given realization of the stochastic parameters, the computed displacements allow to determine equivalent complex P-wave and shear moduli as functions of frequency, representing the behavior of the heterogeneous material at the macroscale. Figure 25 shows two different fluid patch realizations, corresponding to the leakages (a), where the fluid saturation is 10%, and the reservoir (b), where the fluid saturation is 56%. In this case we used a side length of 50 cm, $D=2.5$ and $a = 5$ cm. Once determined the equivalent complex P-wave and shear moduli $\overline{M}_c(\omega)$ and $\overline{\mu}(\omega)$, the complex P- and S-wave velocities are given by

$$v_p(\omega) = \sqrt{\frac{\overline{M}_c(\omega)}{\rho}} \quad \text{and} \quad v_s(\omega) = \sqrt{\frac{\overline{\mu}(\omega)}{\rho}}. \quad (67)$$

In order to obtain the average equivalent complex moduli for such media, we calculated the means and variance of phase velocity and quality factor by applying the compressibility tests in a Monte Carlo fashion. In other words, we averaged phase velocities and quality factors over many patchy realizations of statistical parameters. [67] show that the variance of the equivalent compressional phase velocity averaged over the whole range of frequencies stabilizes at a very low constant value after about 30 realizations. We also computed the complex P-wave velocity using the White's theory for layered porous media [74, 13]. White's theory considers a simplified model consisting in plane layers alternatively saturated by brine and fluid mix. Our

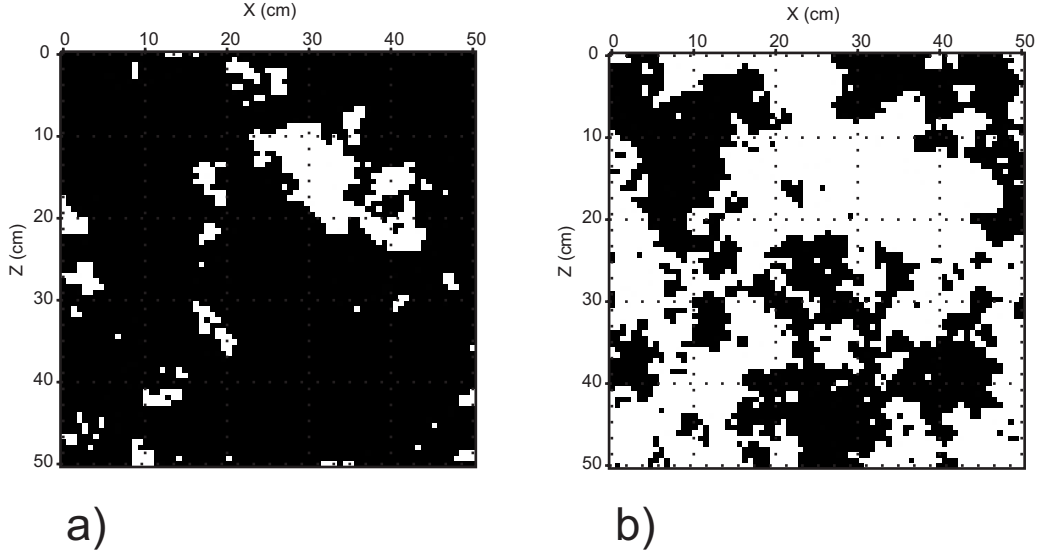


Figure 26: Two different fluid patch realizations, corresponding to the leakages (a), where the fluid saturation is 10%, and the reservoir (b), here the fluid saturation is 56%.

methodology considers a more realistic medium consisting in fractal patches. For the case of plane layers, both procedures yield the same results. Figure 26a,b show the results obtained using the two methodologies for the three leakages. The layer width used for the periodic White model is 17 cm. The strong differences in the attenuation curves of the two methods justifies the use of the oscillatory tests, because White's model overestimates attenuation and shifts attenuation peaks. The results obtained for the reservoir show that the attenuation and velocity dispersion is very small.

Because shear tests applied to these rock samples gave negligible attenuation and velocity dispersion, their corresponding curves are not presented for brevity's sake. The S-wave velocities are computed using the Gassmann relation (65). To obtain the P-wave velocity and quality factor in the other formations we use White's model of patchy saturation [74, 14], using a residual CH_4 saturation of 0.3% and a patch size of 3 cm. In the overburden the saturating gas is air, with a saturation of 50%. It is assumed that the medium has spherical patches of CH_4 or air in a brine saturated background. The S-wave quality factors have been calculated using the following approximated relation:

$$Q_S = Q_P \frac{4}{3} \left(\frac{v_S}{v_P} \right)^2, \quad (68)$$

where Q_P is the P-wave quality factor, v_P is the P-wave velocity and v_S is the S-wave velocity. This relation is based on the assumption that there is no dissipation during a purely compressional cycle ($Q_P \gg 1$).

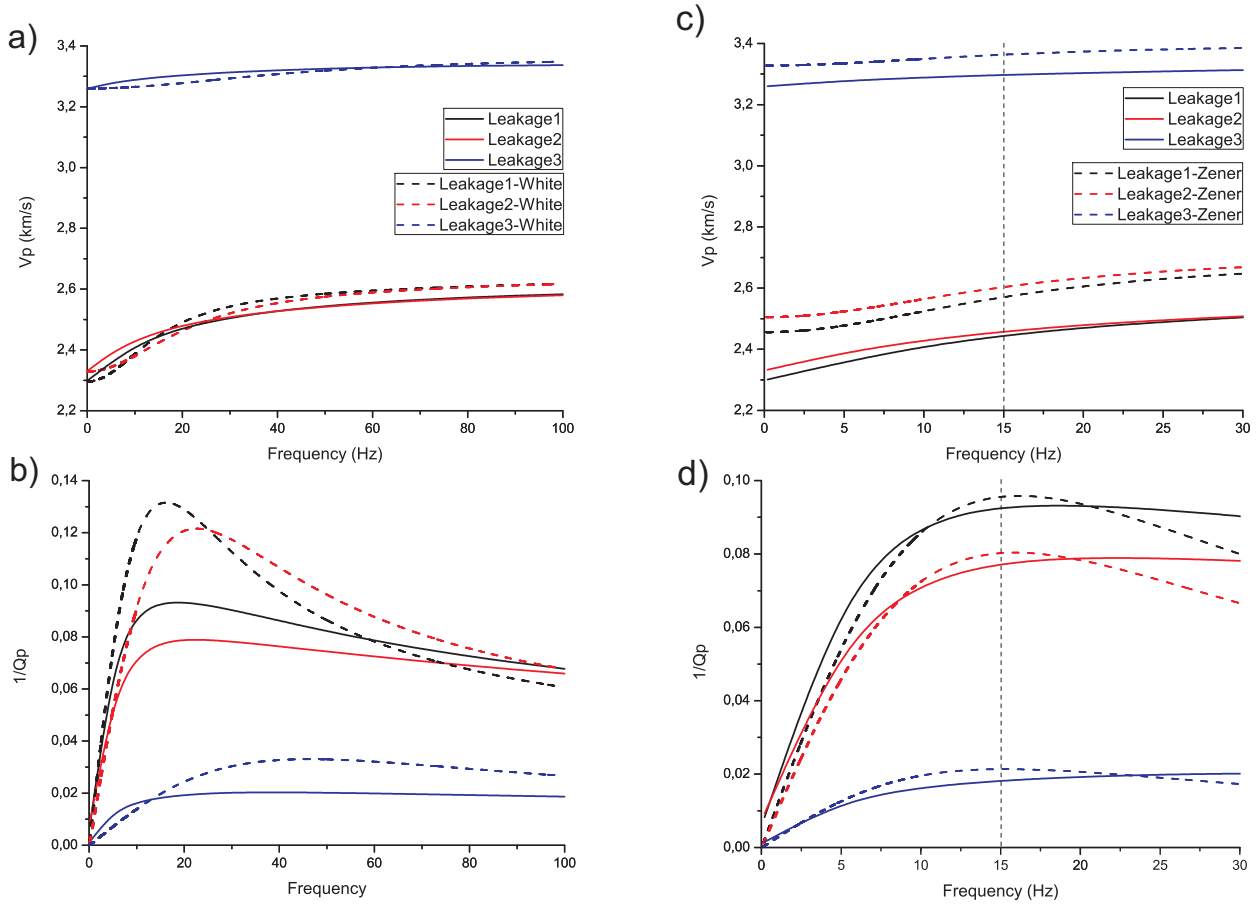


Figure 27: P-wave velocity (a) and quality factor (b) obtained using oscillatory compressibility tests and the White’s layered model for the three leakages. Best fit of the P-wave velocity (a) and quality factor (b) obtained using the Zener model.

Finally, we define an equivalent viscoelastic model fitting the behaviour of the computed complex moduli in the desired range of frequencies using a Zener model [53]. Figure 26c,d shows the fit of the P-wave velocities and quality factors obtained for the three leakages. This model is used at the macroscale to perform numerical simulations of wave propagation phenomena in the time domain.

5.7 Simulations

We simulated a seismic line shot along a 2D section coinciding with one of the migrated seismic sections available. The staggered grid, corresponding to the geological model, has 800 x 720 points. The mesh is structured, with rectangular cells. with a grid spacings $dx = 5$ m and $dy = 5$ m This grid size is sufficient to sample the shortest wavelengths, according to the Nyquist

theorem. The time-domain equations for wave propagation in a heterogeneous, viscoelastic and isotropic medium are described in detail in subsection 5.3. The anelasticity is described by the standard linear solid, also called the Zener model. We locate a source and a receiver at every grid point at the surface to simulate a plane wave. The plane wave is absorbed at the top, it goes down and it impinges on the interfaces and is reflected back to the surface where it is recorded by the receivers. As the reflectors are sub-horizontal, the result can be considered equivalent to a zero-offset section. The source is a dilatation stress whose time-history is a Ricker wavelet with a dominant frequency of 15 Hz. The wavefield is computed by using a time step of 0.5 ms with a maximum time of 2.2 s. The modeling algorithm is based on a 4th-order Runge-Kutta time-integration scheme and the staggered Fourier method to compute the spatial derivatives [12]. The viscoelastic seismograms before and after CO₂ injection show the expected differences. Figure 27a show that the leakages that we hypothesized are easily identifiable. Discrimination between methane and carbon dioxide in the reservoir is possible on synthetic data. Nevertheless, the differences are subtle, and they may be masked in presence of noise, or non-repeatable acquisition patterns.

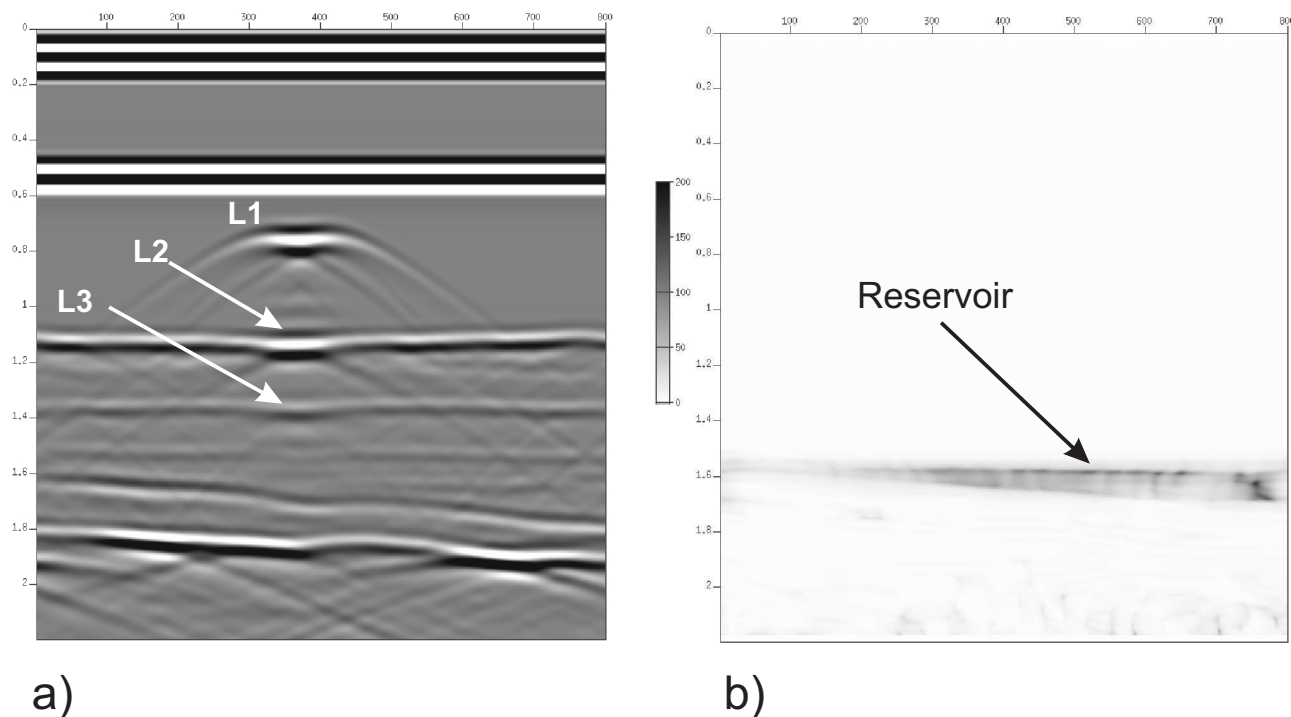


Figure 28: Viscoelastic synthetic seismogram after the CO₂ injection, in presence of the leakages (a). NRMS section obtained using the simulations before and after the CO₂ injection, without leakages (b).

A common procedure, when assessing the similarity of two time-lapse data sets, is to use repeatability metrics, such as the normalized rms (NRMS)[35], where

$$NRMS = 100 \frac{RMS(repeat - base)}{0.5(RMS(repeat) - RMS(base))}. \quad (69)$$

Figure 27b shows the NRMS section obtained using the simulations before and after the CO₂ injection, without leakages. Now we can clearly see that there is a difference between the pre-injection and post-injection. The difference is above the value of 15% that has been measured in real seismic data [35]. The leakage has a NRMS much higher than the noise, because of the strong impedance contrast and the frequency change, so that it is well visible. Therefore, notwithstanding the difficulties of the repeatability of a seismic survey onshore, possible CO₂ migration should be detectable.

5.8 Conclusions

In this work, we present a numerical methodology to obtain synthetic seismograms in heterogeneous media, considering a particular case of a depleted gas field in which CO₂ is supposed to be stored. This methodology consists in rock-physics theories to calculate the properties of rocks and pore fluids, and in an upscaling procedure to obtain equivalent viscoelastic solids for heterogeneous fluid-saturated porous media. Oscillatory compressibility and shear tests, based on a finite-element solution of the classical Biot's equations in the space-frequency domain enable us to obtain the equivalent complex undrained plane-wave and shear moduli of rock samples. Because at mesoscopic scales rock parameter distributions are generally uncertain and of stochastic nature, we apply the oscillatory tests in a Monte Carlo fashion. Then, fitting the P-wave and shear moduli using a Zener model we replace the Biot medium containing mesoscopic-scale heterogeneities by an average equivalent viscoelastic solid, where the mesoscopic effects are included by solving a set of local boundary value problems. To illustrate this procedure, we performed numerical experiments to obtain the average equivalent complex moduli of patchy-saturated sandstones. We built a petro-physical model of the Atzbach-Schwanestadt depleted gas field and made seismic numerical simulations. Different 2D rock models were considered, in order to analyze the sensitivity of the mesoscopic effect at seismic frequencies in the three different states of CO₂: gas, supercritical and liquid. The simulations evidenced that leakages are more evident when the CO₂ is in the gaseous state, until about 600m depth. However, they are also visible at early stages, where the CO₂ is in the liquid or supercritical states (just over the reservoir). If in the reservoir there is another gas (methane) and the saturation is high, the seismic response is small and it may be masked by the noise. In this case a cross-well seismic survey may help to evaluate also the changes within the reservoir, related to varied CO₂

saturations. These simulations confirm that this methodology is particularly important for modelling CO₂ geological storage and, more generally, in the context of exploration geophysics. This because performing numerical simulation of wave propagation employing the viscoelastic equation is computationally much less expensive than any numerical procedure based on the discretization of the full Biot's equations for the same order of accuracy.

These results are contained in the work

A finite element method to model attenuation and dispersion effects in highly heterogeneous fluid-saturated porous media presented in the International Conference on Theoretical and Computational Acoustics (ICTA2009), held in Dresden, Germany, in September 9th, 2009, to appear in the Proceedings of the Conference.

6 Seismic characterization of thin beds containing patchy carbon dioxide-brine distributions

In this work we first study seismic attenuation and velocity dispersion effects due to wave-induced fluid flow in weakly-consolidated sandstones containing highly-heterogeneous distributions of carbon dioxide (CO_2) and brine. Since in certain CO_2 injection sites, such as the Sleipner Field, this fluid accumulates forming thin layers, we also analyze the role of this loss mechanism in the AVA seismic response of this kind of structures. Numerical experiments let us observe that although wave-induced fluid flow effects are very significant, the seismic responses obtained considering the viscoelastic nature of the layers are very similar to those obtained replacing the thin bed by an elastic layer with the same bulk density and shear velocity but with a compressional velocity equal to that of the heterogeneous medium averaged in the effective data bandwidth. This fact suggests that the prestack spectral inversion method recently published by the authors could be used to estimate representative compressional velocities and layer thicknesses in these environments. Results using realistic synthetic prestack seismic data show that CO_2 -bearing thin beds similar to those found at the Sleipner Field can be characterized in terms of its thickness and representative compressional velocity. This information, in turn, can be qualitatively related to CO_2 saturations and volumes, and thus, the prestack spectral inversion methodology could find application in the monitoring of the evolution of CO_2 plumes at injection sites similar to that at the Sleipner Field.

6.1 Introduction

Underground storage of carbon dioxide (CO_2) is an immediate option to reduce the amount of this greenhouse gas in the atmosphere, and thus to mitigate the climate change. Seismic methods constitute a very useful tool to monitor the injection of this gas due to the marked contrast between its acoustic properties and those of brine.

Since October 1996, CO_2 has been injected into the Utsira Sand at the Sleipner Field, offshore Norway, with more than 8.4 million tonnes currently in the reservoir [3]. This reservoir is a weakly consolidated sandstone lying at depths between 800 m and 1100 m. Internally it contains thin intra-reservoir shale layers, having typical thicknesses of 1–2 m. The CO_2 is injected at a supercritical state near the bottom of the Utsira Sand, and it rises due to buoyancy effects until it reaches flow barriers such as the thin shale layers and the top seal shale. Beneath each intra-reservoir shale, CO_2 accumulates following the structural relief and forms layers of up to a few meters thick [3]. These thin layers can be identified in the seismic data as bright sub-horizontal reflections, which are mainly caused by the high compressibility

of the CO_2 as compared to that of the brine, and by constructive tuning effects of the top and bottom reflections at the CO_2 accumulations [1]. The correct interpretation of the seismic responses of these structures is crucial to perform a proper monitoring of the injection process at the Sleipner Field.

The major cause of seismic attenuation in reservoir rocks at seismic frequencies is presumably wave-induced fluid flow due to mesoscopic-scale heterogeneities, i.e., heterogeneities larger than the pore size but smaller than the predominant wavelengths [75, 74, 55, 13]. It has long been recognized that this loss mechanism is particularly important in the presence of rocks partially saturated with hydrocarbon gas and water, due to the strong contrast between the physical properties of the pore fluids.

[75] and [74] were the first to model this phenomenon, showing that this mechanism produces significant attenuation and velocity dispersion effects at seismic frequencies in partially saturated rocks. Since then, many authors have made important contributions to a better understanding of this subject, including a great variety of analytical solutions to model the seismic response of rock samples containing heterogeneities of ideal geometries (see, for instance, [49, 34, 54]). Other studies are based on numerical simulations of wave propagation, such as in [30] and [61], among others. However, in the low frequency range, these methodologies are computationally expensive or even not feasible because the diffusion length associated with the fluid pressure equilibration is very small as compared with the seismic wavelengths.

Alternatively, [62] recently presented an approach where numerical oscillatory compressibility and shear tests are applied to representative rock samples in order to obtain their equivalent complex undrained plane-wave and shear moduli. This upscaling procedure permits to handle complex geometries and is also computationally convenient, since the rock sample has to be much smaller than the wavelengths associated with the excitation frequencies.

As mentioned by [1], the distribution of CO_2 and brine in the porous volume of the rocks at the Sleipner Field is not expected to constitute a homogeneous mixture with respect to the seismic wavelengths. In such case, considering that the reservoir contains patches of CO_2 in a brine-saturated background, and taking into account the high porosity, high permeability and low frame moduli of the Utsira Sand, together with the high compressibility of the CO_2 , significant attenuation and velocity dispersion effects due to wave-induced fluid flow are expected to arise. These effects, in turn, may play a key role in the observed seismic responses of these environments, and thus, a better understanding of this subject is needed. Certainly, this knowledge would help to extract, from seismic data, useful information about the mesoscopic-scale characteristics of the CO_2 -bearing layers, such as overall CO_2 saturation, nature of fluid distribution and mean size of CO_2 patches, among others.

With these motivations, in this work we first study the seismic attenuation and velocity

dispersion effects that take place at a weakly-consolidated sandstone, similar to the Utsira Sand, that contains patchy CO₂-brine distributions. Next, we analyze the seismic response of CO₂-bearing thin beds as those found at the Sleipner Field, taking into account these effects. With this aim, we follow [63] to obtain the AVA response of patchy CO₂-brine thin beds embedded between two brine-saturated sandstones, taking into account the viscoelastic behavior of the CO₂ accumulations. To model the viscoelastic nature of the thin beds we employ the numerical methodology recently published by [62] which allows to replace a highly-heterogeneous fluid-saturated porous rock by a viscoelastic solid with the same attenuation and velocity dispersion. Finally, we use the prestack spectral inversion technique proposed by [63] to evaluate the possibility of characterizing this type of thin beds, with the ultimate goal of estimating their thicknesses and CO₂ saturations from seismic data.

6.2 Viscoelastic behavior of rocks containing heterogeneous CO₂-brine distributions

As mentioned in the Introduction, the propagation of seismic waves in rocks containing mesoscopic-scale heterogeneities in the fluid or frame properties may induce fluid flow. This physical process constitutes the dominant P-wave attenuation mechanism in reservoir rocks at seismic frequencies and can be understood as follows: when a compressional wave squeezes a heterogeneous fluid-saturated porous material, the different regions of the medium, due to their distinct elastic properties, may undergo different pore-fluid pressures. This, in turn, produces fluid flow and thus generates energy loss and velocity dispersion.

[14] quantified mesoscopic attenuation and velocity dispersion effects at the Utsira Sand, assuming patchy brine-CO₂ saturation. These authors were able to observe that mesoscopic loss may be very significant at this geological formation because of its physical properties. However, to obtain this information they employed the analytical White's model [75], which is strictly valid for spherical gas patches.

In this Section we use the methodology presented in previous sections to extract the viscoelastic behavior of rock samples containing highly-heterogeneous distributions of CO₂ and brine. Since we consider rock samples containing heterogeneities associated with pore-fluid distributions, shear tests produce unimportant mesoscopic effects. Thus, in the numerical examples shown in this work, we assume that the shear moduli of the rock samples are frequency independent, real and equal to the shear moduli of their dry matrices.

6.3 Equivalent viscoelastic solids for the Utsira Sand containing patchy CO₂-brine distributions

In order to analyze the amount of attenuation and velocity dispersion caused by heterogeneous fluid distributions, let us consider the Utsira Sand with a spatially variable CO₂-brine distribution in the form of irregular patches fully-saturated with CO₂ and zones fully saturated with brine. We take into account neither mixing nor capillary forces, and we assume that the two fluids occupy different mesoscopic regions of the model. Also, we neither consider chemical interaction between pore fluids and rock frame nor solubility effects.

We generate these (binary) heterogeneous distributions using stochastic fractal fields based on the so-called von Karman self-similar correlation functions, which are widely used in the statistical characterization of heterogeneities for different applications. Following [26], we consider a that the spectral density is given by 42, corresponding to a fractal process of dimension $D = E + 1 - H$ at scales smaller than a . In the experiments shown later, we take $E=2$, $D=2.5$ and different correlation lengths.

We first partition the computational domain (rock sample) into a finite number of square subdomains Ω_j , where j denotes cell number (we select 100×100 square cells in all cases) and assign to each Ω_j a pseudo-random number drawn from a uniform distribution. We then Fourier transform this field to the spatial wavenumber domain and filter its amplitude spectrum using Equation 42. Then, we transform back the result to the spatial domain and obtain a *micro-heterogeneous* water saturation field $S_w^{(j)}$.

We obtain the final (binary) patchy field (i.e. the *mesoscopic* heterogeneities) by selecting a threshold S^* and setting each cell to zero-water saturation (i.e. 100% CO₂ saturation) or 100%-water saturation according to whether $S_w^{(j)}$ is smaller or larger than S^* . In practice, we select S^* in such a way that an overall CO₂ saturation S_{CO_2} is obtained for each fractal field realization. Figure 29 shows some examples of the quasi-fractal fluid distributions considered in this work.

The next step is to compute the mesoscopic loss. For this purpose we require the rock frame and pore fluids physical parameters. In this sense, we assume that the solid matrix of the rock sample is homogeneous and corresponds to the Utsira Sand, with properties given by [1]. Following this work, we take a rock porosity $\phi = 0.37$, mineral bulk modulus $K_s = 36.9$ GPa and solid grains density $\rho_s = 2.65$ gr/cm³. Also, we consider a brine density $\rho_w = 1.09$ gr/cm³ and bulk modulus $K_w = 2.3$ GPa. In addition we set, for full water saturation, $V_P = 2.05$ km/s and $V_S = 0.643$ km/s [1]. Thus, using the inverse Gassmann's equation and the relation between shear velocity, bulk density and shear modulus, we obtain the rock frame bulk modulus $K_m = 2.68$ GPa, and the shear modulus $\mu_m = 0.857$ GPa. Also, water viscosity is taken to be

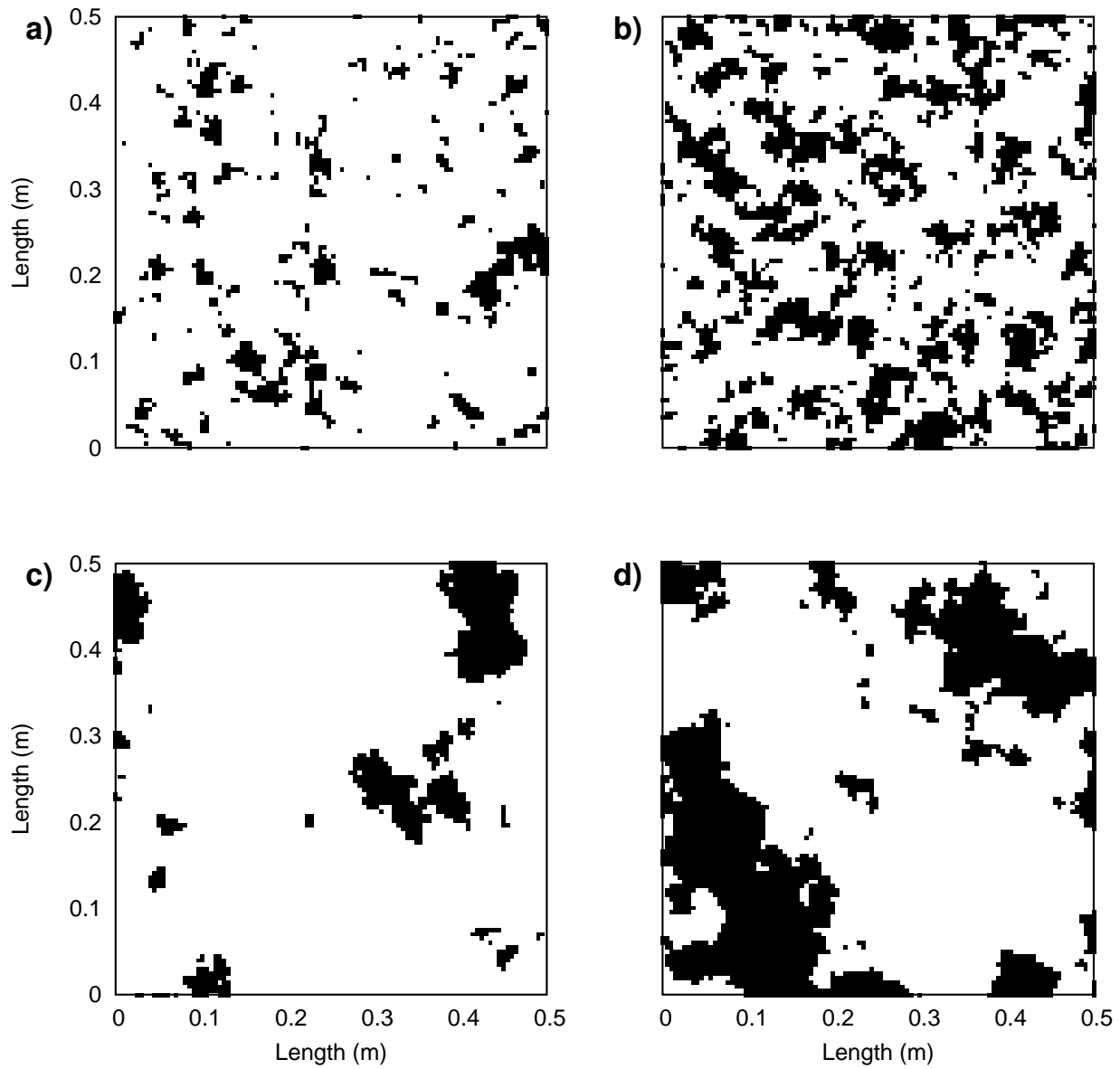


Figure 29: Examples of quasi-fractal distributions of CO_2 and brine in the Utsira Sand. (a) $a = 0.01$ m, $S_{\text{CO}_2} = 0.1$; (b) $a = 0.01$ m, $S_{\text{CO}_2} = 0.3$; (c) $a = 0.1$ m, $S_{\text{CO}_2} = 0.1$; (d) $a = 0.1$ m, $S_{\text{CO}_2} = 0.3$.

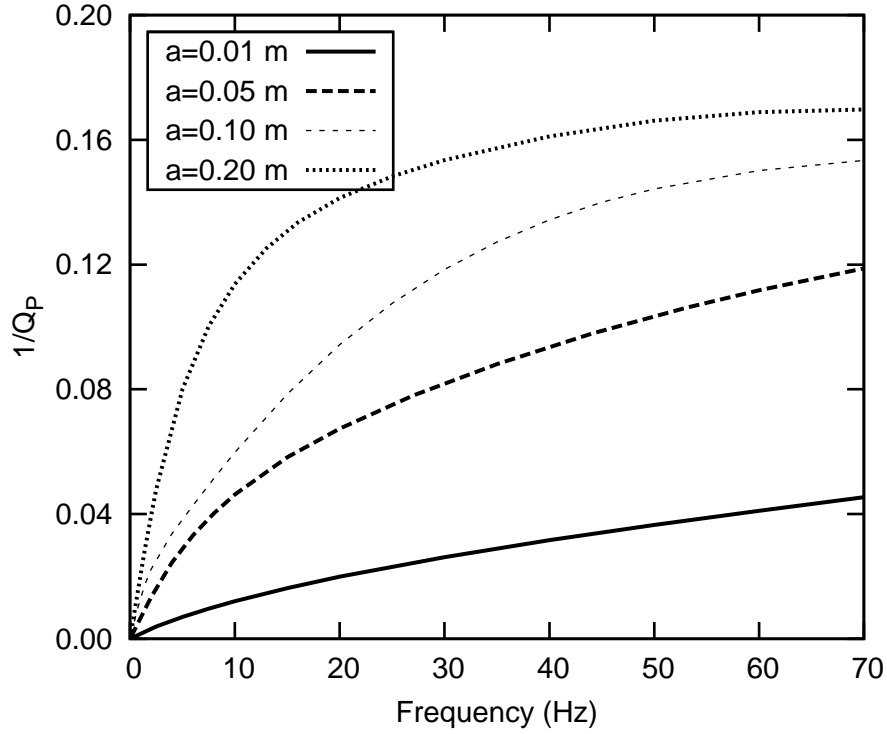


Figure 30: Equivalent inverse quality factor as a function of frequency, for rock samples containing an overall CO_2 saturation $S_{\text{CO}_2} = 0.1$ and different correlation lengths.

$\eta_w = 1$ cP and rock permeability $\kappa = 1$ D.

We calculate the CO_2 density and bulk modulus employing the equation of state proposed by [22], considering a temperature $T = 37^\circ\text{C}$ and pressure $P = 10$ MPa, which are representative values for the reservoir under consideration. Thus, in the numerical experiments we set $\rho_{\text{CO}_2} = 0.693$ gr/cm³ and $K_{\text{CO}_2} = 0.0229$ GPa. In addition, we use the Sutherland's formulae to compute CO_2 viscosity as a function of temperature, obtaining $\eta_{\text{CO}_2} = 1.56 \times 10^{-4}$ P.

Figures 30 and 31 show, respectively, the equivalent compressional inverse quality factor and phase velocity as functions of frequency, for particular samples containing an overall CO_2 saturation $S_{\text{CO}_2} = 0.1$ and different correlation lengths. In all cases the samples are squares of side length $L = 0.5$ m, and we employ computational meshes of 100×100 equal square elements. It can be seen that the energy losses are very significant in the seismic frequency band, with quality factors below 10 in some cases, showing the importance of this loss mechanism in the behavior of the rock samples under consideration. Also, we can observe significant velocity dispersion effects, mainly for correlation lengths above 0.1 m. On the other hand, the mesoscopic effects become less significant as patch size decreases.

These effects become also less significant for CO_2 saturations higher or lower than about 0.1

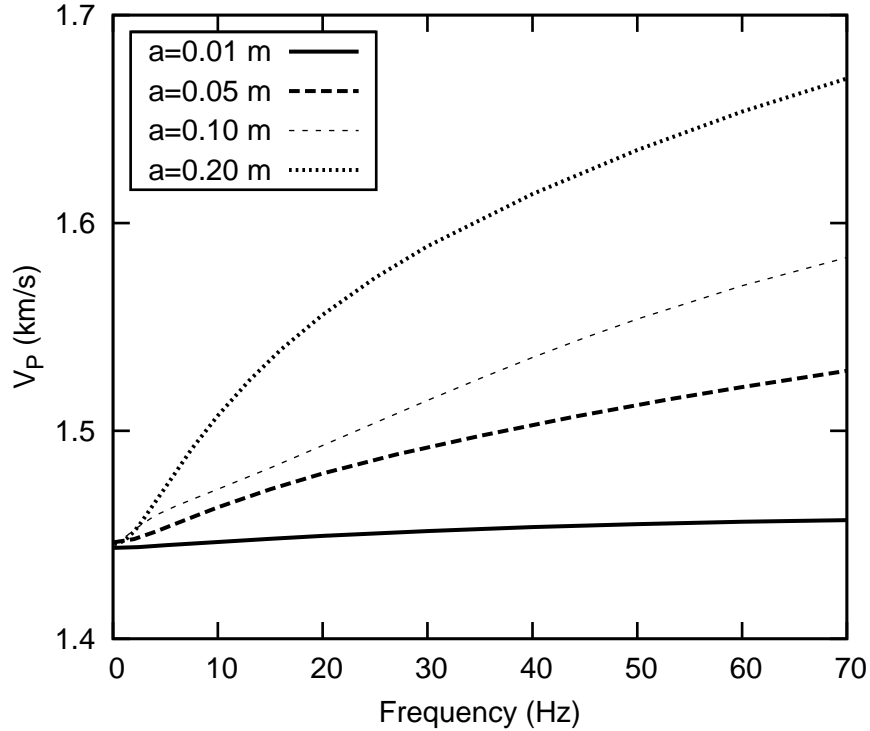


Figure 31: Equivalent compressional phase velocity as a function of frequency, for rock samples containing an overall $S_{\text{CO}_2} = 0.1$ and different correlation lengths.

(plot not shown for brevity). In the case of samples with $S_{\text{CO}_2} = 0.3$ and correlation lengths between 0.01 and 0.2 m, for instance, although velocity dispersion increases with patch size, this increment does not exceed 5% in the frequency range considered. In addition, equivalent quality factor is below 10 only for the largest correlation lengths and for frequencies above 45 Hz.

Since we are dealing with rocks having local properties drawn from certain probability distribution function, it seems appropriate to perform a Monte Carlo analysis as that suggested by [62] to extract the statistical characteristics of phase velocity and quality factor as functions of overall CO_2 saturation, correlation length and frequency. However, the fact that seismic data contain errors of different nature and magnitude, and that their energy is concentrated within a relatively narrow frequency range, suggests that seismic data will at most provide information about a single phase velocity and a single quality factor that are representative of that narrow bandwidth. For this reason, and from a practical point of view, in our analysis we proceed to average the compressional phase velocities and quality factors in a given effective data bandwidth, and plot them as functions of overall saturation and correlation length.

Accordingly, Figure 32 shows the equivalent compressional phase velocity, as a function of

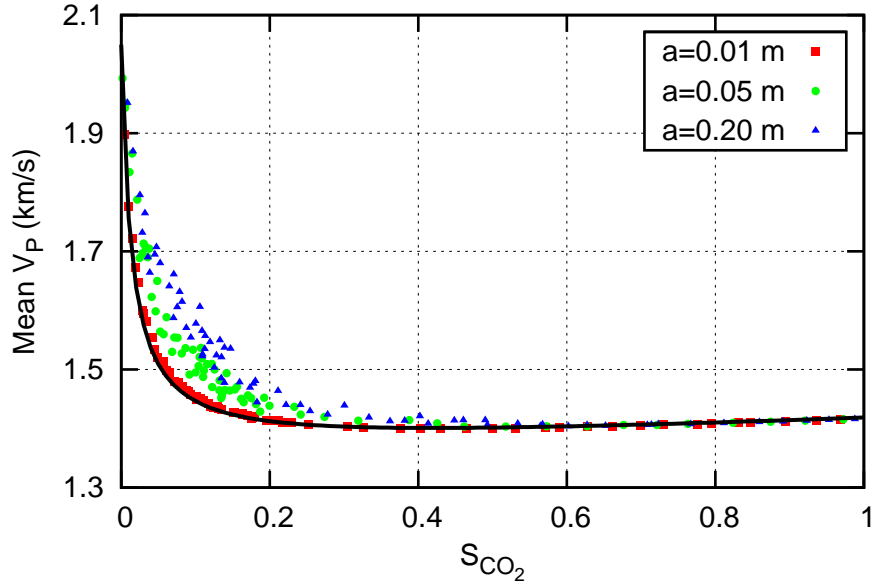


Figure 32: Mean equivalent compressional phase velocity as a function of CO_2 saturation, for different realizations and correlation lengths in Utsira sandstone.

CO_2 saturation and for various correlation lengths, averaged in the frequency range 10–60 Hz for a large number of realizations. This plot also includes the low-frequency limit velocity (solid line), which we compute taking into account that at sufficiently low frequencies the fluid pressure is uniform (isostress state), and thus an effective fluid with bulk modulus given by Wood’s law [13] can be used. Figure 32 shows that mean compressional phase velocities are higher than the low-frequency limit values. These departures are due to velocity dispersion effects and are more significant for large correlation lengths and S_{CO_2} near 0.1. On the contrary, for the correlation lengths considered in this work, we can observe that for CO_2 saturations above 0.3–0.4 or near zero, or for very small patch sizes, average velocities are very close to the low-frequency limit.

Equivalent compressional quality factors were also averaged within the same bandwidth and for the same set of realizations (for the sake of brevity, the corresponding figure is not shown). These data show that very important attenuation levels take place in these experiments, and they become more significant as the characteristic size of the patches increases. The average quality factors take values below 10 for S_{CO_2} near 0.08 and correlation lengths above 0.05 m. This behavior corresponds to that observed in Figure 32, since higher attenuation levels are usually associated with higher levels of velocity dispersion. For CO_2 saturations near zero or above 0.6, approximately, average quality factors take values above 100. In the particular case of very small CO_2 patches, this parameter is above 100 for saturations above 0.2, approximately.

This analysis allows us to observe that seismic data associated with rocks with patchy distributions as those considered in this work are expected to carry useful information that may help to provide some insight about CO₂ saturation values. In addition, these results show that for the patch sizes considered in this work, mesoscopic effects are more significant for CO₂ saturations near 0.1 and large correlation lengths. Also, if CO₂ saturation is higher than 0.6 or close to zero, attenuation and velocity dispersion effects can be disregarded irrespective of the patch size. Therefore, in these cases, CO₂-bearing rocks behave like an elastic solid with a compressional velocity given by that of the low-frequency limit. For very small patch sizes, this approximation is valid for S_{CO_2} higher than about 0.2.

6.4 Seismic response of a CO₂-bearing thin bed

As mentioned in the Introduction, at the Utsira Sand CO₂ accumulates beneath thin intra-reservoir shales, forming thin CO₂-bearing layers that can be identified in the seismic data as bright sub-horizontal reflections. This fact, together with the results shown in previous section, show that seismic attenuation and velocity dispersion effects associated with wave-induced fluid flow may be very significant in these media, playing a key role in the observed seismic responses.

In this section we analyze the seismic responses of thin layers containing heterogeneous distributions of CO₂ and brine in the AVA domain. We use a methodology similar to that presented by [63] to obtain the AVA response of a thin bed embedded between two homogeneous half-spaces but, in this case, we include the viscoelastic behavior of the CO₂-bearing layer. We refer the reader to the work of [63] for the details of the calculations in the case of an elastic thin bed. It is important to remark that in the modeling we neglect the ultra-thin shale layers (1 to 2 m thick) typically found at the Utsira Sand because the contrast between the acoustic impedance of the water-saturated shale layers and that of the water-saturated sandstone is very low.

6.4.1 Methodology

Let us consider a viscoelastic horizontal layer embedded between two elastic homogeneous half-spaces, as shown in Figure 33. Let a plane harmonic compressional wave of frequency $\omega = 2\pi f$ and unit amplitude propagate in the (x, z) plane arriving at the thin bed with an incidence angle θ . The particle displacements in the top half-space are caused by the contributions of the incident wave and the reflected compressional and shear perturbations, while in the bottom half-space they are given by the contribution of the transmitted compressional and shear waves. On the other hand, the displacements within the (viscoelastic) thin bed are obtained by considering four partial wavefields associated with a compressional and a shear-wave traveling upwards, and

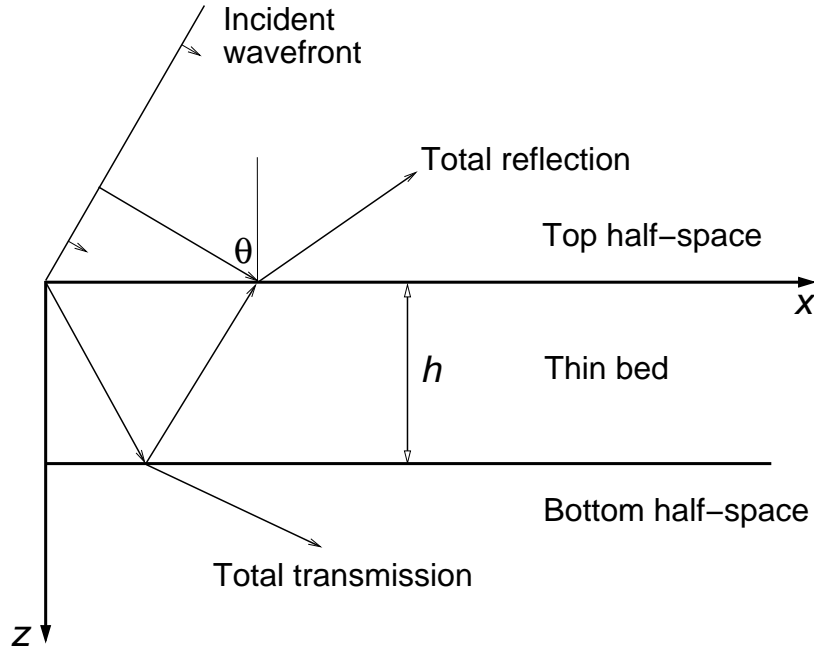


Figure 33: Diagram of the thin-bed model showing the reflection and transmission rays. For simplicity, shear waves generated at the interfaces are not shown.

a compressional and a shear-wave traveling downwards. To represent such contributions, we employ scalar and vector potentials for the compressional and shear waves, respectively.

Then, using the elastic properties of each medium we relate the displacement vectors with the stress tensors by means of the Hooke's law. As usual, we require the continuity of the displacements and normal and shear stresses through the top and bottom layer interfaces, which leads to an 8×8 linear system of equations where the unknowns are the eight potential amplitudes. The product of the source amplitude spectrum and the potential amplitude associated with the reflected compressional wave, for different incidence angles, constitute the spectra of the prestack data.

In order to take into account the viscoelastic nature of the thin layer, the wave number associated with the compressional wave and the Lamé constant λ_c should be taken complex and frequency dependent. To compute them, let us consider a compressional plane wave propagating through such viscoelastic medium. Thus, by definition, it produces a material response of the form $\mathbf{u} = Ae^{i(\omega t - \mathbf{k}^P \cdot \mathbf{r})} \check{\mathbf{k}}^P$ where \mathbf{k}^P is the wave vector, \mathbf{r} is the position vector, $\check{\mathbf{k}}^P$ is the unit vector in the direction of propagation, and A is a constant. The inverse quality factor and phase velocity are related with the modulus of the wave vector, k^P , in the form

$$V_P(\omega) = \frac{\omega}{\text{Re}(k^P)}, \quad (70)$$

$$\frac{1}{Q_P(\omega)} = -2 \frac{\text{Im}(k^P)}{\text{Re}(k^P)}. \quad (71)$$

Then, we can express the modulus of the wave vector as

$$k^P = \frac{\omega}{V_P(\omega)} \left[1 - \frac{i}{2Q_P(\omega)} \right]. \quad (72)$$

In addition, the equivalent complex undrained plane-wave modulus can be written as $\overline{M}_c(\omega) = \lambda_c + 2\mu_m$, where μ_m is the shear modulus of the saturated rock. Thus, λ_c is complex and frequency dependent, and can be expressed as

$$\lambda_c = \overline{M}_c(\omega) - 2\mu_m. \quad (73)$$

In summary, for each frequency we apply the oscillatory compressibility test to obtain the equivalent phase velocity, quality factor and complex plane-wave modulus. Next, using equations 72 and 73 we compute k^P and λ_c .

6.4.2 Numerical experiments: Elastic versus viscoelastic models

With the aim of analyzing the effects of the mesoscopic loss on the seismic behavior of CO₂-bearing thin beds as those found at the Utsira Sand, we apply the recently presented methodology to obtain the seismic responses of these structures considering different thicknesses, incidence angles and CO₂ saturations. In all the examples we use a 30 Hz-Ricker wavelet and a correlation length $a = 0.10$ m.

Figure 34 shows some particular realizations of the seismic responses of layers with thicknesses $h = 5$ and $h = 10$ m, containing two different CO₂ saturations, for two incidence angles (solid lines). In all cases there is an increase in the reflectivity with the angle of incidence and with CO₂ saturation. The last point is explained by the fact that the bed mean phase velocity is lower for $S_{\text{CO}_2} = 0.3$ than for $S_{\text{CO}_2} = 0.1$, and thus the contrast between the acoustic impedance of the thin bed and that of the water-saturated sandstone is more significant. In addition, the reflectivity is stronger in the case $h = 10$ m as compared with $h = 5$ m, as a consequence of the tuning effects for the considered wavelet.

Figure 34 also shows the seismic responses obtained after replacing the (viscoelastic) thin layer by an elastic bed with the same shear velocity and bulk density, but with a compressional velocity similar to that of the heterogeneous CO₂-bearing bed averaged in the effective data

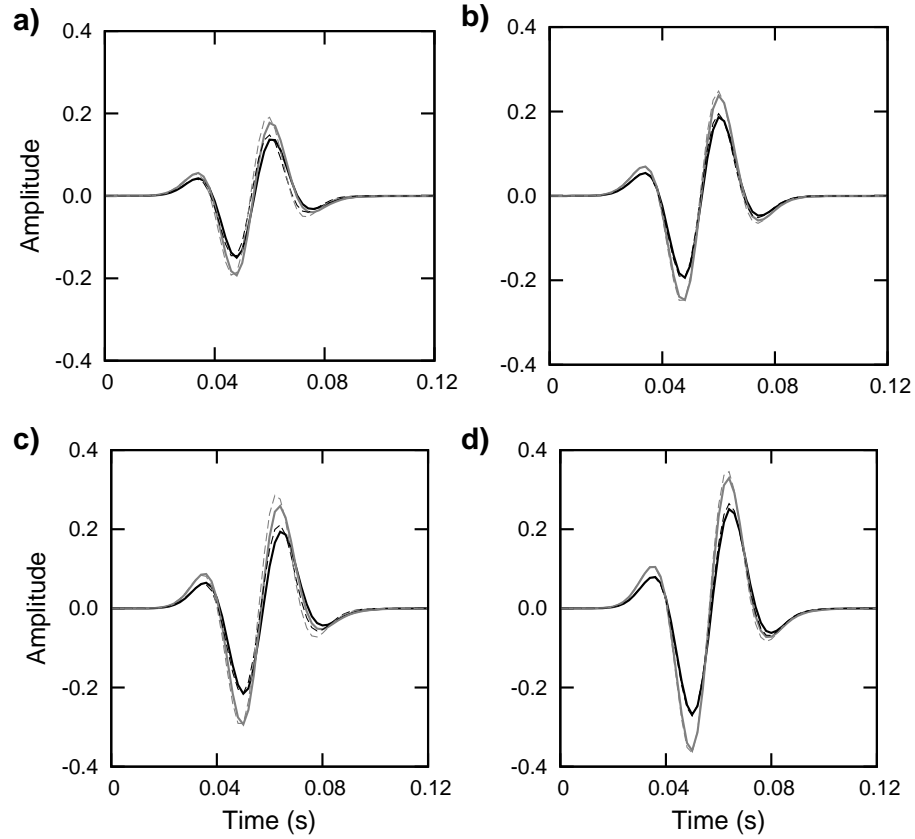


Figure 34: Seismic responses for a 5 m (top panels) and 10 m (bottom panels) thick bed, for $S_{CO_2} = 0.1$ (left panels) and $S_{CO_2} = 0.3$ (right panels). Black lines correspond to an incidence angle $\theta = 0^\circ$, while grey lines correspond to $\theta = 40^\circ$. Solid lines represent the responses obtained taking into account the viscoelastic nature of the thin bed, while dashed lines are those obtained by replacing the thin layer by an elastic bed with a mean compressional velocity.

bandwidth (dashed lines). As expected, the discrepancies between the elastic and viscoelastic models are more significant for $S_{\text{CO}_2} = 0.1$, since mesoscopic effects are particularly important for this saturation value. However, it is interesting to notice that although wave-induced fluid flow effects are very significant in these media, the discrepancies are negligible. To understand this fact we have to take into account that the differences between the seismic responses are associated with energy losses within the bed and with velocity dispersion effects on the acoustic impedance contrasts between the layer and the upper and lower half-spaces. Energy losses effects are not significant because the layer is very thin as compared with the predominant wavelengths of the seismic waves. In addition, since the elastic model considers the mean phase velocity computed within the frequency range in which the data contains most of the energy, the differences due to velocity dispersion effects are minimized.

We observed similar behaviors to those shown in Figure 34 for other CO_2 saturations, correlation lengths and bed thicknesses (not show for brevity).

6.5 Prestack spectral inversion of seismic data for the characterization of CO_2 -bearing thin beds

As we observed in previous sections, the patchy nature of the CO_2 accumulations at the Sleipner Field adds complexity to the modeling of the seismic response of this kind of structures. If we wish to extract useful information from the seismic data to characterize these environments, we must assume a simplified model. In this sense, the similarities between the elastic and viscoelastic seismic responses shown in Figure 34 and analyzed in the previous section suggest that the prestack spectral inversion method presented by [63] to study thin elastic beds, could be used to estimate representative compressional velocities and thicknesses of CO_2 -bearing layers, which in turn could allow us to provide insight into CO_2 saturations and volumes.

With this purpose, in this section we invert the seismic response of thin beds in the prestack spectral (amplitude) domain, assuming an elastic layer embedded between two homogeneous half-spaces. We generate realistic data for thin beds similar to those found at the Utsira Sand, taking into account their viscoelastic natures due to mesoscopic effects. We consider several CO_2 saturations, correlation lengths and bed thicknesses. Also, since the rock properties are randomly sampled from certain probability distribution function, we generate a large number of realizations and invert the resulting data in each case.

Following the procedure proposed by [63], let $A(f, \theta)$ and $\hat{A}(f, \theta)$ be the amplitude spectra of the observed and calculated prestack data, respectively. Then, let J be a function that measures the discrepancies between $A(f, \theta)$ and $\hat{A}(f, \theta)$. Here, J is a 10-dimensional cost function that depends on the elastic properties and densities of the top and bottom half-spaces, and on the

thickness, density and elastic properties of the thin bed. It is given by

$$J = \frac{1}{NM} \sum_{i=1}^N \sum_{j=1}^M w_i \left[A(f_j, \theta_i) - \hat{A}(f_j, \theta_i) \right]^2, \quad (74)$$

where N is the number of incidence angles, M is the number of frequencies, and w_i are weights. The minimization of J with respect to the model parameters represents a highly non-linear inverse problem that can be conveniently solved using a hybrid optimization scheme that involves both simulated annealing (SA) and a linearizing approach ([63]). Note that in the actual computations, $A(f, \theta)$ represents the seismic response of the CO₂-bearing thin bed taking into account its viscoelastic properties, as discussed in previous sections. Contrarily, $\hat{A}(f, \theta)$ is calculated by assuming an elastic bed.

6.6 Results and discussion

In practice, we obtain $A(f, \theta)$ from the observed data after isolating the seismic response of the CO₂-bearing thin bed in the time-angle domain using an angle-dependent time window. This process is illustrated in Figure 35, where we show a typical angle-gather used in the inversion together with the angle-dependent time window (we use a Hamming window to avoid truncation effects). Then, we obtain $A(f, \theta)$ by applying the Fourier transform to the windowed data and taking the modulus.

The data used in the following numerical tests were obtained as follows. First, we calculated the AVA response of the viscoelastic thin-bed model in the frequency domain for incidence angles in the range 0–40° and considering a 30 Hz-Ricker wavelet. Then, after applying the inverse Fourier transform, and in order to simulate realistic data, we added two types of noise: additive and convolutional. The additive noise consisted in the summation of pseudo-random numbers drawn from a Gaussian distribution. For convenience, random noise was previously filtered with a 5-100 Hz passband filter. The convolutional noise was added, on the other hand, with the aim of simulating the effects of small reflectors that may be present in the data. These reflectors can be associated with the presence of the under- and overburdens. In this sense, we chose an arbitrary set of well-log data to construct an angle-dependent reflectivity using approximate Zoeppritz formula. Subsequently, we convolved this reflectivity with the source wavelet and added the result to the data. Finally, we applied a constant hyperbolic move-out to each trace. Figure 35 shows a typical gather constructed this way and used in the tests that follow.

During the inversion process, we consider bounding constraints in all the model parameters to guarantee physically reasonable models and to allow for the incorporation of a priori infor-

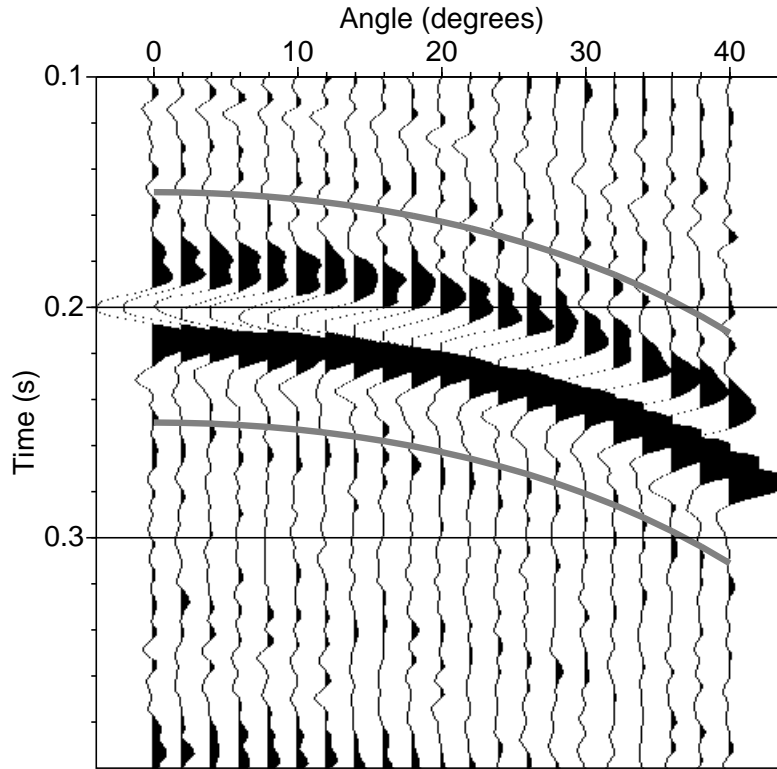


Figure 35: Typical prestack data used in the inversion. The hyperbolic gray lines show the angle-dependent window used to isolate the assumed CO₂-bearing thin bed seismic response. In this particular case, $h = 10$ m, $S_{\text{CO}_2} = 0.1$ and $a = 0.1$ m.

mation. This is accomplished by selecting narrow search ranges for those parameters whose values are known approximately from other means (e.g., well-log data). On the other hand, we set wide search ranges for those parameters where this extra information is not available. In a practical context, for the inversion of the seismic responses of the CO₂-bearing thin beds we assume that densities and velocities of the two half-spaces are known within a tolerance error of about $\pm 5\%$, but density, thickness and velocities of the thin bed are allowed to attain any value within much wider search ranges (see Table 5). As noticed, the search ranges for the S-wave velocity and the density of the CO₂-bearing layer are in fact relatively narrow, since these quantities do not vary significantly for different CO₂ saturations and reasonable estimates are available based on previous works (e.g. [1]).

Layer	V_P (km/s)	V_S (km/s)	ρ (gr/cm ³)
Top half-space	2.0–2.2	0.6–0.7	2.0–2.2
CO ₂ -bearing thin bed	1.3–2.2	0.5–0.7	1.9–2.1
Bottom half-space	2.0–2.2	0.6–0.7	2.0–2.2

Table 5. Search ranges used in the inversion. The thickness of the CO₂-bearing thin bed is allowed to vary in the range 2–25 m. For the two half spaces, we assume that their true properties are $V_P = 2.05$ km/s, $V_S = 0.643$ km/s and $\rho = 2.073$ gr/cc.

In order to analyze the performance of the inversion procedure in different scenarios we carried out a large number of inversions for different CO₂ saturations, correlation lengths and thicknesses. For simulating the seismic response of the thin layers we selected a Ricker wavelet, whose tuning thickness can be estimated using the expression $\sqrt{6}/(2\pi f_0)$, where f_0 is the dominant frequency [18]. In the case of a 30 Hz-Ricker wavelet, the tuning thickness is about 13 ms, which turns out to be about 10 m for CO₂-bearing beds as those found at the Utsira Sand. In the numerical examples that follow we used thicknesses of 4, 7 and 10 m. Also, in all cases we added noise to the data with a signal-to-noise ratio of about 10 (by amplitude) and chose the 10–60 Hz band for the computation of the cost function J (we set all weights equal to 1). In addition, for each realization we averaged the results of 100 inversions, where each inversion involved the same data but different SA seeds. We used this strategy because of the difficulties associated with the minimization of the cost function J , which often does not show a very clear global minimum. Consequently, slightly different sets of model parameters led to excellent data fits. Nevertheless, since the variability of the compressional velocity and thickness estimates was small, we assumed that these averaged values correspond to the optimum solution within the global minimum region of the 10-dimensional model space.

Figure36a shows, as a function of CO₂ saturation, the estimated compressional velocity for a 10 m-thick CO₂-bearing layer considering three different correlation lengths ($a = 0.01, 0.05$ and 0.2 m). In particular, for each one of the correlation lengths, we took into account seventy realizations associated with different CO₂ saturations randomly distributed in the range 0–1. We can observe that for very low CO₂ saturations, there is a rapid increase in the compressional velocity for decreasing saturations. On the other hand, for saturations above 0.2, no significant velocity changes are appreciated.

Because mesoscopic effects are much more significant for CO₂ saturations around 0.1, the elastic model used to fit the actual viscoelastic response becomes less appropriate in these cases. In addition, at these saturation values the compressional velocity is very sensitive to the

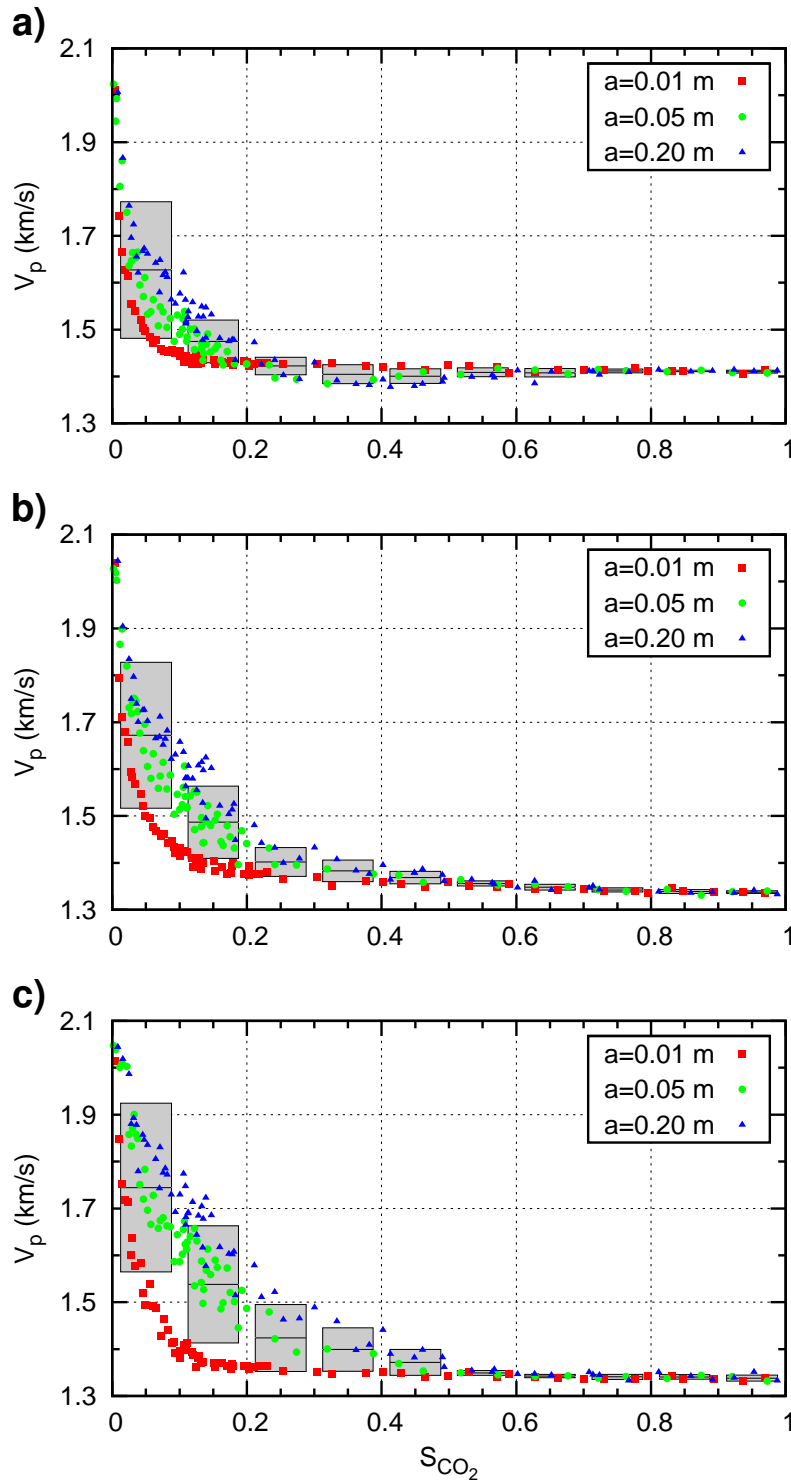


Figure 36: Estimated compressional velocity as a function of CO₂ saturation for different realizations and correlation lengths: (a) $h = 10$ m; (b) $h = 7$ m; $h = 4$ m. Each dot represents the average of 100 different inversions. Gray bars show the mean (binned) velocity plus-minus one standard deviation (bin size 0.1).

geometry of the CO₂ patches. As a consequence of these facts, it turns out that the dispersion of the inverted velocity is larger at these saturation levels, as can be observed in Figure 36a. Contrarily, when CO₂ saturations are relatively high (say above 0.2), the fit is much more accurate and the compressional velocity is less sensitive to the pore fluids distribution; thus, the variability of the inverted velocity is smaller.

Also, it is interesting to see that the uncertainty of the inverted velocity is significantly lower for very small correlation lengths (e.g., red dots). This result can be explained by noting that for the frequencies considered in this work, the patches are very small and the wavelengths do not *see* differences among realizations.

Figures 36b and 36c show the results obtained for CO₂-bearing layers of thicknesses 7 m and 4 m, respectively. We can observe that the results obtained in these cases show similar behaviors to those found for a 10 m thick bed.

Figure 36 can be compared with Figure 32, where we plotted, for several CO₂ saturations and correlation lengths, the compressional velocity associated with the Utsira Sand containing patchy CO₂-brine distributions, averaged in the bandwidth 10–60 Hz. The similarities between the plots suggest that, although the inverted velocities shown in Figure 36 are not expected to attain the same numerical values than those in Figure 32, their behaviors with respect to S_{CO_2} are comparable. The inverted velocities are, in fact, model parameters associated with a (simple) elastic thin-bed model that produces a seismic response similar to that of the viscoelastic model at different saturation levels. This fit is valid, at least, within the frequency range where the observed seismic energy is concentrated, which coincides with the bandwidth selected for the inversion. Thus, considering that the mean velocities shown in Figure 32 exhibit a clear relationship with CO₂ saturations, we believe that the inverted velocities shown in Figure 36 can be used as a petrophysical attribute to characterize CO₂-bearing thin beds in terms of saturations.

In effect, take Figure 36a as a reference. The gray bars show the mean (binned) inverted compressional velocity plus-minus one standard deviation, as a function of CO₂ saturation (bin size 0.1). These bars can be used as a guide to associate inverted velocities with S_{CO_2} . It is clear from the graph that in general high compressional velocities are associated with low (below 0.2) CO₂ saturations. On the other hand, velocities lower than about 1.45 km/s are indicative of S_{CO_2} higher than about 0.2. It is not possible to make any distinction between saturations above 0.2, because the inverted velocities do not show any significant change for these saturation values. On the contrary, the analysis shows that the inverted velocities may help to discriminate among saturations below 0.2.

On the other hand the uncertainty of the inverted velocities increases, as expected, for thicknesses below tuning (see Figures 36b and 36c), specially for large correlation lengths. As

in the previous case, for these layer thicknesses high inverted velocities are indicative of low saturation values, while low velocities are associated with saturations above 0.2.

In addition, it is important to remark that should the patchy distribution be of known correlation length, the dispersion of the inverted velocity represented by the gray bars in Figure 36 would be much smaller, and thus it would be possible to draw more certain conclusions about CO₂ saturations.

It is worth taking into account that the quantities and ranges mentioned in this analysis are not meant to be rigorous. In any case, the inverted velocity is viewed as a CO₂ indicator, specially for discriminating between low and high CO₂ concentrations, and hence, it can be used for the characterization of CO₂-bearing thin beds. We believe that this methodology may be a valuable tool to provide some broad but useful information about CO₂ saturation from prestack seismic data.

In addition to the thin-bed compressional velocity, the other parameter of interest is layer thickness. Table 6 shows the mean and standard deviation of the inverted thickness for three different CO₂ saturation ranges, taking into account the values obtained for the three correlation lengths. As expected, the larger the thickness and CO₂ saturation, the smaller the uncertainty. For $h = 10$ m, the accuracy of the inversion is very high, even for low saturation values. As layer thickness is smaller, the accuracy is lower; however, even in the case of a 4 m thick bed the estimates are reasonable and may be very useful to improve the knowledge of the distribution of the injected CO₂ in the reservoir.

Actual thickness	$S_{\text{CO}_2} < 0.1$	$0.1 \leq S_{\text{CO}_2} < 0.2$	$S_{\text{CO}_2} \geq 0.2$
4 m	6.1 ± 1.8	4.9 ± 1.5	3.3 ± 0.5
7 m	8.0 ± 1.1	7.2 ± 0.9	6.0 ± 0.4
10 m	10.3 ± 0.7	9.9 ± 0.4	9.4 ± 0.1

Table 6. Mean and standard deviation of the inverted thickness for different CO₂ saturation ranges. Values are given in meters.

6.7 Conclusions

The application of the oscillatory test permits us to study seismic attenuation and velocity dispersion effects due to wave-induced fluid flow in media similar to the Utsira Sand, containing highly-heterogeneous distributions of CO₂ and brine. We can observe that these effects may be very significant, with quality factors below 10 in some cases, mainly for CO₂ saturations near

0.1 and correlation lengths above 0.1 m. Hence, seismic data is expected to carry information about this loss mechanism, information that can be used to derive useful characteristics about the mesoscopic-scale properties of these environments.

The AVA seismic response of a thin bed containing patchy brine-CO₂ distributions as those found at the Utsira Sand is very similar to that of an elastic thin bed with the same shear velocity and bulk density, but with a compressional velocity equal to that of the patchy-saturated Utsira Sand averaged in the effective data bandwidth. This is explained by the fact that although the mesoscopic loss is very important in these media, energy losses within the thin bed are not very significant because the layer is very thin as compared to the predominant seismic wavelengths. In addition, the differences due to velocity dispersion effects are minimized when using a mean compressional velocity.

This evidence permits us to make use of a prestack spectral inversion algorithm to estimate representative compressional velocities and thicknesses of CO₂-bearing thin beds, information which in turn could be used to provide insight into CO₂ saturations and volumes. In this sense, results using realistic simulated prestack seismic data show that a CO₂-bearing thin bed with properties similar to that of the Utsira Sand could be characterized in terms of its thickness and compressional velocity, which allows us to derive some broad but useful information about CO₂ saturations. In this context we show that low velocities are indicative of relatively high CO₂ saturations (above 0.2), while high velocities are indicative of low saturations.

It is important to remark that this analysis is valid for patchy models with correlation lengths in the range 0.01 to 0.2 m. As expected, the smaller the correlation length the smaller the uncertainty of the estimates, both for inverted velocity and thickness. If the correlation length (or mean size of the CO₂ patches) were known, the information contained in the inverted velocity would allow us to derive more accurate CO₂ saturation estimates from seismic data. Unfortunately this information is not available, and only rough but very useful CO₂ saturation estimates can be obtained using the proposed methodology. Another limitation is that it is not possible to discriminate among saturations above 0.2, an issue that is naturally expected because the compressional velocity at the Utsira Sand does not show any significant change for these saturation levels. In spite of this, we believe that the inverted velocity represents, from a practical point of view, an important petrophysical attribute that can be used as an indicator to characterize CO₂-bearing thin beds. Furthermore, the proposed procedure allows us to obtain reasonable thickness estimates for sub-tuning CO₂-bearing layers of a few meters. This kind of information is crucial to perform a proper monitoring of the injection process at sites such as the Sleipner Field.

Finally, it is worth mentioning that the results suggest that the proposed spectral inversion methodology may be used to characterize CO₂-bearing thin beds in a two or three-dimensional

framework. In this sense, it would be possible to estimate thicknesses and CO₂ saturations at various locations and hence to obtain useful information about how the layer develops areally and what the CO₂ plume extension is within that unit. Presumably, at points far away from the injection point the CO₂ saturations will be low, and thus the extension of CO₂ plume could be delimited by detecting those regions where the inverted compressional velocity is very high. On the other hand, since zones with low velocities are indicative of high CO₂ saturations, the procedure could be used to monitor in time and in space the extent of the CO₂ distribution as well as how it migrates to the nearby zones around the injection point. These studies are currently under investigation.

The results presented in this Section were included in the following paper:

Seismic characterization of thin beds containing patchy carbon dioxide-brine distributions, by J. Germán Rubino & Danilo R. Velis, submitted to Geophysics in September 2009. Presently under review.

References

- [1] Arts R.J., Eiken O., Chadwick R.A., Zweigel P., van der Meer L. and Zinszner B., 2004. Monitoring of CO₂ injected at Sleipner using time-lapse seismic data. *Energy*, 29, 1383-1392.
- [2] Arts R.J., Chadwick R.A., Eiken O., Trani M. and Dortland S., 2007. Synthetic versus real time-lapse data at the Sleipner CO₂ injection site. Society of Exploration Geophysicists San Antonio Meeting, Expanded Abstracts, 26, 2974-2978.
- [3] Arts, R., A. Chadwick, O. Eiken, S. Thibeau, and S. Nooner, 2008, Ten years' experience of monitoring CO₂ injection in the Utsira Sand at Sleipner, offshore Norway: First Break, 26, 65-72.
- [4] Avseth P., Mukerji T. and Mavko G., 2005. Quantitative seismic interpretation: applying rock physics tools to reduce interpretation risk. Cambridge University Press.
- [5] Bachu S., 2003. Screening and ranking of sedimentary basins for sequestration of CO₂ in geological media in response to climate changes, *Environmental Geology*, 44, 277-289.
- [6] Batzle M. and Wang Z. , 1992. Seismic properties of pore fluids. *Geophysics*, 57, 1396-1408.
- [7] J.G. Berryman, 1982, Elastic waves in fluid-saturated porous media, in *Lecture Notes in Physics*, J. Ehlers and K. Hepp and R. Kippenhahn and H.A. Weidenmüller and J. Zittart, Springer Verlag 154, 38-50.
- [8] Biot M.A., 1956. Theory of propagation of elastic waves in a fluid-saturated porous solid. I. Low frequency range, *J. Acoust. Soc. Am.*, 28,168-171.
- [9] Biot M.A., 1962. Mechanics of deformation and acoustic propagation in porous media, *Journal of Applied Physics*, 33, 1482-1498.
- [10] Brown S., Hagin P. and Bussod G., 2007. AVO Monitoring of sequestration, Society of Exploration Geophysicists San Antonio Meeting, Expanded Abstracts, 26, 2974-2978.
- [11] J.M. Carcione, 2001, *Wave fields in real media: wave propagation in anisotropic, anelastic and porous media*, Pergamon.
- [12] Carcione, J. M., 2007. *Wave Fields in Real Media: Wave Propagation in Anisotropic, Anelastic, Porous and Electromagnetic Media*, 2nd edn revised and extended, *Handbook of Geophysical Exploration*, vol. 38, Elsevier, Amsterdam, 514 pp.

- [13] J.M. Carcione and S. Picotti, 2006, P-wave seismic attenuation by slow-wave diffusion: Effects of inhomogeneous rock properties, *Geophysics*, 71, O1–O8.
- [14] Carcione J.M., Picotti S., Gei D. and Rossi G., 2006, Physics and seismic modeling for monitoring CO₂ storage, *Pure Appl. Geophys.*, 163, 175-207.
- [15] Carcione, J. M., Helle, H. B., Santos, J. E., and Ravazzoli, C. L., 2005, A generalized Gassmann modulus for multi-mineral porous media, *Geophysics*, **70**, N17-N26.
- [16] Castagna J.P., Swanz H.W. and Foster D.J., 1998. Framework for AVO gradient and intercept interpretation, *Geophysics*, 63, 948-956.
- [17] Chadwick R.A., Arts R. and Eiken O., 2005. 4D seismic quantification of a growing CO₂ plume at Sleipner, North Sea. In Doré A. and Vinning, B. (eds.) *Petroleum Geology: NW Europe and Global Perspectives*, Proceedings of the 6th Petroleum Geology Conference, 1385-1399.
- [18] Chung, H. and D. Lawton, 1995, Frequency characteristics of seismic reflections from thin beds: *Canadian Journal of Exploration Geophysicists*, 31, 32–37.
- [19] Danesh, A., 2001, *PVT and phase behaviour of petroleum reservoir fluids*, Elsevier.
- [20] Deresiewicz H. and Rice J.T., 1960. The effect of boundaries on wave propagation in liquid-filled porous solid: I. Reflection of plane waves at a true plane boundary, *SSA Bull.*, 50, 599-607.
- [21] Douglas Jr. J., Santos J.E., Sheen D. and Ye, X., 1999, Nonconforming Galerkin methods based on quadrilateral elements for second order elliptic problems, *Math. Modelling and Numer. Anal.*, 33, 747-770.
- [22] Duan Z., Moller N., Weare J., 1992. An equation for the CH₄-CO₂-H₂O system: I. Pure systems from 0 to 1000C and 0 to 8000 bar, *Geochimica et Cosmochimica Acta* ,56: 2605-2617.
- [23] N.C. Dutta and H. Odé, 1979, Attenuation and dispersion of compressional waves in fluid-filled porous rocks with partial gas saturation (White model). Part I: Biot theory, *Geophysics*, 44, 1777-1788.
- [24] Dutta N. and Odé H., 1983. Seismic reflections from a gas-water contact. *Geophysics*, 48, 148-162.

- [25] Fenghour A., Wakeman W.A. and Vesovic V., 1998, The viscosity of Carbon Dioxide. *J. Phys. Chem. Ref. Data*, 27(1), 31-44.
- [26] Frankel A. and Clayton R. W., 1986, Finite difference simulation of seismic wave scattering: implications for the propagation of short period seismic waves in the crust and models of crustal heterogeneity, *J. Geophys. Res.*, 91, 6465-6489.
- [27] Gassmann F., 1951. Über die elastizität poroser medien. *Vierteljahrschrift der Naturforschenden Gessellshaft in Zurich*, 96, 1-23.
- [28] Ghaderi, A. and Landro, M., 2009. Estimation of thickness and velocity changes of injected carbon dioxide layers from prestack time-lapse seismic data. *Geophysics*, 74, O17-O28.
- [29] B. Gurevich and S.L. Lopatnikov, 1995, Velocity and attenuation of elastic waves in finely layered porous rocks, *Geophysical Journal International*, 121, 933-947.
- [30] H.B. Helle and N.M. Pham and J.M. Carcione, 2003, Velocity and attenuation in partially saturated rocks: poroelastic numerical experiments, *Geophysical Prospecting*, 51, 551-566.
- [31] Ha T., Santos J.E. and Sheen D., 2002, Nonconforming finite element methods for the simulation of waves in viscoelastic solids, *Comput. Methods Appl. Mech. Engrg.*, 191, 5647-5670.
- [32] Hardage B. and Silva D., 2009. Seismic steps aids sequestration, *AAPG Explorer*, May 2009. <http://www.aapg.org/explorer/2009/05may>.
- [33] Hashin, Z., and Shtrikman, S., 1963, A variational approach to the theory of the elastic behaviour of multiphase materials, *J. Mech. Phys. Solids*, **11**, 127-140.
- [34] D.L. Johnson, 2001, Theory of frequency dependent acoustics in patchy-saturated porous media, *Journal of the Acoustical Society of America*, 110, 682-694.
- [35] Kragh, E. and Christie, P., 2002, Seismic repeatability, normalized rms and predictability, *The Leading Edge*, **21**, 642-647.
- [36] H. Kolsky, 1963, *Stress waves in solids*, Dover Publications,
- [37] M. Krief and J. Garat and J. Stellingwerff and J. Ventre, 1990, A petrophysical interpretation using the velocities of P and S waves (full waveform sonic), *The Log Analyst*, 31, 355-369.

- [38] Lohrenz, J., Bray, B.G., and Clark, C.R., 1964, Calculating viscosities of reservoir fluids from their compositions, *J. Pet. Technol.*, Oct, 1171-1176.
- [39] J.L. Lumley and H.A. Panofsky, 1964, The structure of atmospheric turbulence, Wiley-Interscience.
- [40] McCain Jr., W., 1990, The properties of petroleum fluids, Penn Well Books, Tulsa, Oklahoma.
- [41] Mason Y. and Pride S., 2006, Numerical modelling of the seismic attenuation due to wave induced flow in heterogeneous materials, Society of Exploration Geophysicists New Orleans Meeting, Expanded Abstracts, 1998-2002.
- [42] Y.J. Masson and S.R. Pride, 2007, Poroelastic finite difference modelling of seismic attenuation and dispersion due to mesoscopic-scale heterogeneity, *Journal of Geophysical Research*, 112, B03204.
- [43] Mavko G., Mukerji T. and Dvorkin J., 1998, The rock physics handbook: Tools for seismic analysis of porous media, Cambridge University Press.
- [44] Meadows M., 2008, Time-lapse seismic modeling and inversion of CO₂ saturation for storage and enhanced oil recovery, *The Leading Edge*, 27(4), 506-516.
- [45] Morse, P. M., and Ingard, K. U., 1986. Theoretical acoustics, Princeton University Press, Princeton, New Jersey.
- [46] T. M. Müller and B. Gurevich, 2005, Wave-induced fluid flow in random porous media: attenuation and dispersion of elastic waves, *Journal of the Acoustical Society of America*, 117, 2732–2741.
- [47] T.M. Müller and J. Toms, 2007, Velocity-saturation relation for rocks with fractal distribution of the pore fluids, 77th Annual International Meeting, SEG, Expanded Abstracts, 1624–1628.
- [48] J.C. Nedelec, 1980, Mixed finite elements in R^3 , *Numerische Mathematik*, 35, 315-341.
- [49] , A.N. Norris, 1993, Low-frequency dispersion and attenuation in partially saturated rocks, *Journal of the Acoustical Society of America*, 94, 359-370.
- [50] Oldenburg, C. M., Benson, S. M., 2001, CO₂ Injection for Enhanced Gas Production and Carbon Sequestration, SPE International Petroleum Conference and Exhibition, Mexico, SPE 74367.

- [51] Osborne M.J. and Swarbrick R.E., 1997, Mechanisms for generating overpressure in sedimentary basins: a reevaluation. *Am. Assoc. Petrol. Geol. Bull.*, 81, 1023-1041.
- [52] Peng D.Y. and Robinson D.B., 1976. A new two-constant equation of state. *Ind. Eng. Chem. Fundam.*, 15(1), 59-64.
- [53] Picotti, S., Carcione, J. M., Rubino, J. G., Santos, J. E., and Cavallini, F., 2010, A viscoelastic representation of wave attenuation in porous media, *Computer & Geosciences*, **36**, 44-53.
- [54] S.R. Pride and J.G. Berryman, 2003, Linear dynamics of double-porosity and dual-permeability materials. I. Governing equations and acoustic attenuation, *Physical Review E*, 68, 036603.
- [55] S.R. Pride and J.G. Berryman and J.M. Harris, 2004, Seismic attenuation due to wave-induced flow, *Journal of Geophysical Research*, 109, B01201.
- [56] Pride S., Tromeur E. and Berryman J.G., 2002, Biot slow-wave effects in stratified rock, *Geophysics*, 67, 271-281.
- [57] Polak, S., Schultz, H. M., Kroos, B., Zweigel, J., Kunaver, D., Zweigel, P., May, F., Lindeberg, E., Pannetier-Lescoffit, S., Alles, S., Faber, E., Teschner, M., Poggenburg, J., 2006. The Atzbach-Schwanenstadt gas field - a potential site for onshore CO₂ storage and EGR *The Leading Edge*, **25**, 1270-1275.
- [58] Raistrick, M., 2008. Carbon capture and storage projects to challenge governments, scientists and engineers. *First Break*, 26, 35-36.
- [59] Ravazzoli, C., 2001. Analysis of reflection and transmission coefficients in three-phase sandstone reservoirs. *Journal of Computational Acoustics*, 9(4), 1437 -1454.
- [60] P.A. Raviart and J.M. Thomas, 1975, Mixed finite element method for 2nd order elliptic problems: *Mathematical Aspects of the Finite Element Methods*, Lecture Notes in Mathematics, 606, Springer.
- [61] J.G. Rubino and J.E. Santos and S. Picotti and J.M. Carcione, 2007, Simulation of upscaling effects due to wave-induced fluid flow in Biot media using the finite-element method, *Journal of Applied Geophysics*, 62, 193-203.
- [62] Rubino, J., C. Ravazzoli, and J. Santos, 2009, Equivalent viscoelastic solids for heterogeneous fluid-saturated porous rocks: *Geophysics*, 74, N1–N13.

- [63] Rubino, J. and D. Velis, 2009, Thin-bed prestack spectral inversion: *Geophysics*, 74, R49–R57.
- [64] Santos, J.E., Corberó, J., Ravazzoli, C.L. and J.Hensley, 1992. Reflection and transmission coefficients in fluid saturated porous media. *Journal of the Acoustical Society of America*, 91, 1911-1923.
- [65] Santos J.E., Ravazzoli C.L., Gauzellino P.M. and Carcione J.M., 2005, Numerical simulation of ultrasonic waves in reservoir rocks with patchy saturation and fractal petrophysical properties, *Computational Geosciences*, 9, 1-27.
- [66] Santos, J. E., Rubino, J. G. and Ravazzoli C.L. , 2007, Statistical analysis of the effective velocity and mesoscopic attenuation in patchy saturated porous media, 77th Annual International Meeting SEG Expanded Abstracts 26, 2708-2712.
- [67] Santos, J. E., Rubino, J. G. and Ravazzoli C.L. , 2009, A numerical upscaling procedure to estimate effective plane wave and shear moduli in heterogeneous fluid-saturated poroelastic media, *Comput. Methods Appl. Mech. Engrg.* 198, 2067-2077.
- [68] Span R. and Wagner W., 1996. A new equation of state for carbon dioxide covering the fluid region from the triple-point temperature to 100 K at pressures up to 800 MPa. *Phys. Chem. Ref. Data*, 25, 1509-1596.
- [69] Teja, A.S. and Rice P., 1981. Generalized corresponding states method for viscosities of liquid mixtures. In *Ind. Eng. Chem. Fundamentals*, 20, 77-81.
- [70] J. Toms and T.M. Müller and R. Ciz and B. Gurevich, 2006, Comparative review of theoretical models for elastic wave attenuation and dispersion in partially saturated rocks, *Soil Dynamics and Earthquake Engineering*, 26, 548–565,
- [71] J. Toms and T.M. Müller and B. Gurevich, 2007, Seismic attenuation in porous rocks with random patchy saturation, *Geophysical Prospecting*, 55, 671–678.
- [72] van der Waals, J. D., 1873. *Over de continuïteit van den gas en vloeïstoftoestand*, dissertation, Leiden.
- [73] Z. Wang and A. Nur, 1989, Effect of CO₂ flooding on the velocities in rocks with hydrocarbons: *SPE Reservoir Engineering*, 4, 429-436.
- [74] J.E. White and N.G. Mikhaylova and F.M. Lyakhovitskiy, 1975, Low-frequency seismic waves in fluid-saturated layered rocks, *Izvestija Academy of Science USSR, Physics of the Solid Earth*, 10, 654-659.

- [75] J.E. White, 1975, Computed seismic speeds and attenuation in rocks with partial gas saturation, *Geophysics*, 40, 224-232.
- [76] Zyserman F. I, Gauzellino P. M. and Santos J. E., 2003, Dispersion analysis of a non-conforming finite element method for the Helmholtz and elastodynamic equations, *Int. J. Numer. Meth. Engng.*, 58, 1381–1395